UNIVERSIDADE DE LISBOA
FACULDADE DE CIÊNCIAS
DEPARTAMENTO DE GEOLOGIA

Mineralogy and geochemistry of the hydrothermal alteration haloes related to the Mandoos Volcanic Massive Sulphide (VMS) deposit, Sumail Ophiolite, Oman

André Cravinho Santos

Mestrado em Geologia Económica
Especialização em Prospecção Mineral

Relatório de Estágio orientado por:
Jorge Manuel Verdilhão Figueiras e Ana Patrícia Marques de Jesus

2017

UNIVERSIDADE DE LISBOA
FACULDADE DE CIÊNCIAS
DEPARTAMENTO DE GEOLOGIA

Mineralogy and geochemistry of the hydrothermal alteration haloes related to the Mandoos Volcanic Massive Sulphide (VMS) deposit, Sumail Ophiolite, Oman

André Cravinho Santos

Mestrado em Geologia Económica
Especialização em Prospecção Mineral

Relatório de Estágio orientado por
Ana Patrícia Marques de Jesus e Jorge Manuel Verdilhão Figueiras

2017

Em memória de José António Várzea Cravinho

TABLE OF CONTENTS

AGRADECIMENTOS

Já que não há dissertação alguma sem esta parte (e, sejamos sinceros, quantas vezes ao folhear teses apenas lemos resumos e agradecimentos), aqui segue o elenco de quem foi contribuindo, de diferentes formas, para que se chegasse ao fim. Antes de mais, como a minha memória já não é o que era (por sua vez, graças, em parte, a este trabalho), faltarão pessoas. Se aqui não estão, não é por mal. Diria para me virem cravar um copo, que vontade não falta. Mas falta dinheiro, portanto fica para a próxima.

Um especial agradecimento ao coordenador deste mestrado, Professor António Mateus, por todo o apoio prestado e paciência consumida, mas também pela preocupação e a disponibilidade que demonstrou, recorrentemente, no esclarecimento de dúvidas. Ao orientador Jorge Figueiras, pela leitura atenta, pelas correcções e sugestões, que permitiram melhorar substancialmente o documento final. À coorientadora deste trabalho, Ana Jesus, por todas as reuniões por Skype, pelas discussões, sugestões e correcções que beneficiaram este trabalho. Devo-lhe ainda um agradecimento especial e pessoal, não só por toda a preocupação, incentivo e amizade, mas também por me ter recebido de braços abertos em sua casa, a 8500km da minha, como se fosse apenas um reencontro de velhos (não etariamente) amigos, apesar de nos termos acabado de conhecer. Obrigado por teres tornado a estadia no inferno (aquilo é quente!) muito mais agradável. Quero ainda agradecer à Professora Isabel Costa e ao ao Professor Pedro Madureira, pelas preciosas correcções, sugestões e reparos, muitíssimo úteis na redacção de um documento final substancialmente melhor que o provisório. Gostaria também de agradecer a todas as pessoas que tornaram os meus dias na GUTech/Omã mais fáceis; um especial agradecimento à Céline Ducassou, ao Wilfried Bauer, ao Bernhard Pracejus e à Amal. À Universidade de Aveiro, na pessoa do Professor Fernando Rocha e de Maria Cristina Sequeira, pelo fornecimento de parte dos dados de litogeoquímica. Ao Mathieu Bennoit, pela outra metade dos dados de geoquímica de rocha total, os elementos traço, e pelas discussões relativas ao contexto geológico/geodinâmico. Ao Dr. Pedro Rodrigues, pelos dados de microssonda e também por toda a simpatia e paciência a responder às minhas questões existenciais relativas à química mineral. E por me mostrar que sou um nabo a fazer contas.

Aos meus amigos, da universidade e não só, devo também umas palavrinhas:

À Sofia, pelo enorme apoio e amizade, por ter sido (quase) minha mãe (também quem cria dois, cria dois e meio), por todo o gasóleo gasto a fazer um desvio, à noite, quando podia estar a fazer o o-ó, do qual se auto-intitula profissional. Pela companhia a horas obscenas na faculdade, que tornou o trabalho pós-luz solar muito mais tolerável e também pelas incríveis pausas, a melhor parte das noitadas sem fim. Além disso, devo-lhe também um agradecimento especial por ter sido fundamental para manter, pelo menos, parte da minha sanidade mental; obrigado pelo enorme apoio e por me ter aturado tanto tempo. Vamos à pausa! À Cristiana, por me ter deixado ocupar o sofá da sua casa algumas vezes, pela amizade e apoio constantes, pela motivação, assim como pelos já, internacionalmente, conhecidos bolos e doces, que fazem as delicias da malta do 4º piso do C6. À Rita (Ferraz), pela contagiante boa disposição, pela simpatia e motivação, pela ajuda e por me ter deixado, tantas vezes, invadir a sua casa e ocupar o sofá. Ao Bruno, por me ter aturado três meses em Omã sem ter cometido homicídio…oportunidades não faltaram. À chefa Filipa, pela ajuda essencial no processamento laboratorial das amostras, pela motivação, incentivo e puxões de orelhas (às vezes tem de ser!). Ao Filipe, pela preocupação, incentivo e amizade (já lá vão 6 anos!), e por ser uma excelente pessoa e um exemplo, a nível pessoal e científico; ao Ivo, pela boa disposição, apoio, motivação e toda a amizade, também já longa; ao Zé, pelas pausas, "reuniões importantes" e pela companhia durante as noites intermináveis na faculdade. Ao Marcelo e aos restantes amigos deste mestrado com quem passei momentos inesquecíveis, Fred, Miguel, Velez e Hugo. Ao Soares, por todas as palavras de carinho e amizade e pela constante preocupação; à Joana Duarte, pelas palavras de apoio, motivação e por todos os chocolates deliciosos que trouxe da Suíça. Ao Pambu, pela preocupação e por, apesar de toda a distância e tempo, continuar a ser o mesmo palhaço que ia comigo buscar chocolate e pão ao LIDL (bons tempos). À Maja que, apesar de ter tido uma estadia curta em Portugal, se tornou uma ótima companheira de trabalho e dos momentos de pausa, para beber uma cerveja e falar das banalidades da vida (em inglês

claro); agradeço-lhe também a amizade e todas as palavras de apoio e motivação. Ao "camarada" Manuel Silva, por todas as discussões geológicas nas pausas para café. Um agradecimento especial também à Rita (Pereira), Marcelino, Miguel Teixeira, Ana Medeiros, Ana Jacinto, Vanessa Pais e Joana Ferreira, pela amizade e pela forma desinteressada com que me apoiaram ao longo deste(s) ano(s).

Depois de toda esta lamechice, vem outra, que deixo o melhor para o fim. Gostaria de agradecer de forma muito especial aos meus pais, ao João e às minhas avós, que sempre me possibilitaram e incentivaram, sem restrições, a seguir os estudos em algo que, pelo menos ao início, não faziam ideia do que era (caramba, são só pedras!) – nem eu, passados seis anos, faço! Devo-lhes também um pedido de desculpas, por todas as ausências. Obrigado pela enorme compreensão e pelo constante apoio.

Por fim, quero agradecer à pessoa a quem dedico este trabalho, que sempre me dirigiu palavras de motivação, carinho, apreço e apoio e, infelizmente, não o pôde ver terminado.

ACKNOWLEDGEMENTS

Since this part is almost mandatory (and let's be honest, no one reads any other chapters besides the abstracts and the acknowledgements), here is the list of people who contributed, in many ways, for this work to be completed. First of all, since my memory isn't what is used to be (partly due to this work), some people are probably missing. It's not in bad faith. I'd say to come and ask me for a drink, I've got the will. But not the money, so we'll schedule it for another day.

I am forever in debt to the MSc program coordinator, Professor António Mateus, for all the support and patience but also for all the concern and availability in answering questions he has shown. To this work supervisor, Jorge Figueiras, whose careful reading allowed to substantially improve the presented work. To the co-supervisor, Ana Jesus, for all the Skype meetings, discussions, suggestions and corrections, especially regarding my English skills, which were also important to this thesis. I owe her, also, many thanks, personally, not only for the concern, incentive and friendship, but also for welcoming me so warmly at her place, 8500km from mine, as if it was only an old friends reencounter, despite the fact we had just met each other. Thank you for making the stay in hell (that place is warm!) so much enjoyable. Also, many thanks to Professors Isabel Costa and Pedro Madureira, for the time and patience spent, reading this work, and for the precious and important corrections and suggestions, improving this final version I'd also like to thank to everyone that made my days in GUtech/Oman easier: special mentions to Céline Ducassou, to Wilfried Bauer, to Amal, to Bernhard Pracejus and to Michaela Bernecker. To the University of Aveiro, namely Professor Fernando Rocha and Maria Cristina Sequeira, for providing part of the lithogeochemical data. To Mathieu Bennoit, for the other part of the whole-rock trace element geochemical data as well as for the discussions related to the geodynamic and geological setting of the ophiolite. To Dr. Pedro Rodrigues, for the microprobe data, as well as for his kindness and patience in answering all my existential question regarding mineral chemistry. And also for showing me that I'm a complete zero at math.

I'd also want to mention some of my friends.

To Sofia, for the support and friendship. For being (almost) my mother (she raised two so, two and a half is not a problem), for all the gasoline spent in a small detour at night, when she could have been sleeping, which she brags about being a professional at it. For the company at obscene hours in the university, making the post-daylight work more bearable, as well as for the amazing breaks, the best time of those endless nights. Furthermore, I owe her also some special thanks for being fundamental for me to keep, at least part, of my mental health. Come, it's break time! To Cristiana, for sometimes letting me occupy her sofa, for the constant friendship and support, motivation and the, by now internationally known, cakes and sweets, that delights everyone on the 4th floor of C6. To Rita (Ferraz), with her constant and contagious good humour, for the kindness and motivational conversations, for the help she gave me and for often letting me invade her place and crash in. To Bruno, for putting up with me for three months without committing murder…There were a lot of opportunities. To the boss, Filipa, for the essential help in the laboratorial processing of the samples, for the motivational words and the occasional earful. To Filipe, for the constant concern, motivation and friendship (6 years already!). For being a terrific person and a great example, personally and scientifically; to Ivo, for the great and fun mood, support and motivation, as well as for the now long (and good) friendship; to Zé, for the breaks from work, "important meetings" and for the companionship throughout the nights in FCUL; to Marcelo and the rest of my friends from the MSc, with which I spent unforgettable moments, Fred, Miguel, Velez and Hugo. To Soares, for all the kind words and for being a great friend; to Joana Duarte, for all the inspiring words and for all the delicious chocolates brought from Switzerland. To Pambu, for the interest and, despite the distance, remaining the same asshole that kept me company at night in FCUL, after grabbing some bread and chocolate from LIDL (good old times). To Maja which, despite the short stay in Portugal, became a pleasant company, during work-time and afterwards: to grab a beer and talk about the trivialities of life; I also want to thank her for all the support and motivation, even when she left Lisbon. To my "comrade" Manuel Silva, for all the geological discussions and the coffee-break enjoyable times. I'd also like to give out special thanks to Rita (Pereira), Marcelino, Miguel Teixeira,

Ana Medeiros, Ana Jacinto, Vanessa Pais and Joana Ferreira, for the friendship and support during this/these year(s).

After all this lame conversation, here it comes: another one. I saved the best for last. I'd like to appreciate and acknowledge, in a very special way, both my parents, my brother João and my grandmothers, who've always supported and encouraged me, without restraints, to follow what I thought best, despite, at first, they didn't have any clue of what was it all about (damn, it's just rocks!)- neither do I, and six years have passed already! I owe them, also, a great deal of apologies, for all my absences. Thanks for the huge understanding and support.

Finally, I also want to thank in a very special way to the person I dedicate this work, which unconditionally supported me and showed a great deal of appreciation and care; which motivated me to keep studying and, sadly, couldn't see this "chapter" completed.

RESUMO

Durante o Cretácico, o complexo contexto geológico e geodinâmico do ofiolito de Sumail, situado no Omã, permitiu o desenvolvimento de sistemas hidrotermais e consequente formação de numerosas mineralizações de sulfuretos maciços, algumas com interesse económico, encontrando-se hospedadas na sequência vulcânica. Esta é dividida em quatro principais unidades vulcânicas (da mais antiga para a mais recente): *Geotimes, Lasail, Alley e Boninitic Alley*. Apesar da maior parte destes depósitos se encontrarem hospedados na transição entre *Geotimes* e *Alley*, qualquer período de quiescência vulcânica, muitas vezes marcados pela presença de sedimentos metalíferos e outros marcadores de actividade hidrotermal exalativa, traduz um horizonte temporal onde a precipitação e acumulação de sulfuretos maciços é possível. Esta província metalogénetica de VMS do tipo máfico/tipo Chipre, é, então, comparável, em dimensão e tonelagem, ao ofiolito de Troodos, Chipre, com 30 a 50Mt de tonelagem total de minérios.

O depósito de Mandoos, situado perto de Sohar, na parte Norte do ofiolito de Sumail, foi descoberto em 2009 através de técnicas geofísicas aeroportadas (VTEM), e as operações de extração tiveram início em 2011, em *open-pit*. Com recursos medidos que perfazem um total de 8 Mt, com 5 Mt de reservas (a 1.8% de Cu), este depósito representa um dos maiores depósitos descobertos neste ofiolito. Apesar disto, a inexistência de estudos detalhados desta mineralização, fazem dele um ótimo caso de estudo, permitindo o desenvolvimento de um estudo metalogenético aprofundado, (possivelmente) contribuindo para a definição de critérios de prospeção deste tipo de mineralizações. Assim, recorrendo a amostras recolhdas no *open-pit* e em sondagens cedidas pela Mawarid Mining, este trabalho teve como objectivo a caracterização da sequência vulcânica que hospeda esta mineralização, utilizando critérios mineralógicos e geoquímicos, com objectivo de I) atribuir uma posição volcano-estratigráfica ao depósito, e II) caracterizar os padrões de alteração observados, distinguindo entre halos de alteração imputáveis a episódios regionais, de baixa temperatura ("metassomatismo oceânico") e halos de alteração hidrotermal, associados à precipitação e acumulação de sulfuretos maciços.

As rochas vulcânicas que hospedam esta mineralização correspondem a rochas basálticas, de natureza toleiitica, caracterizadas por anomalias positivas, baixas, em Ti. Os teores baixos em ETRL (comparados com os dos ETRP), os padrões normalizados (condrito C1) de ETR e os seus teores em HSFE permitem atribuir estas rochas à unidade Lasail, colocando a possibilidade das rochas vulcânicas a muro da mineralização corresponderem a vulcanismo transicional entre esta unidade e a *Geotimes*. Considerando as características geoquímicas, particularmente de elementos traço e, também, os dados publicados (*e.g.* Godard *et al*., 2003; 2006; Kusano *et al.*, 2012) para esta unidade vulcânica, considera-se que estas derivam da fusão parcial de rochas mantélicas, sujeitas anteriormente a taxas de fusão parcial elevadas, aquando da formação de fundidos silicatados máficos, tipo MORB, cuja extrusão originou a unidade infrajacente, *Geotimes*, num contexto de *rift* e formação de crosta oceânica.

A sequência vulcânica é composta por basaltos microporfiríticos, sob a forma de escoadas maciças e/ou *pillow-lavas*, com quantidades e distribuição de vesículas variáveis, traduzindo os canais por onde os gases escaparam, durante a sua extrusão. Estas encontram-se também localmente fragmentadas, sendo esta fragmentação resultante de processos de arrefecimento brusco, relacionados com a interacção com água do mar. Estes processos estão associados a fracturação e fragmentação, criando descontínuidades físicas que permitem o escoamento de fluidos, gerando texturas similares a brechas. Os microfenocristais de clinopiroxena, de composição augítica, e de feldspatos do grupo das plagioclases, de composição bytownítica, encontram-se dispersos, por vezes em aglomerados, numa matriz composta por micrólitos de feldspatos do grupo das plagioclases, de composição semelhante à dos microfenocristais, e óxidos de Fe com quantidades consideráveis de Ti.

Um primeiro episódio de alteração, de natureza pervasiva e ubíquo, correspondente a alteração regional decorrente da circulação de água do mar, em condições oxidantes, emm razões água/rocha baixas (metassomatismo oceânico), processo comumente apelidado de espilitização. Este estádio de alteração é marcado pela alteração das fases vulcânicas primárias: no caso dos cristais de clinopiroxena, esta alteração dá-se preferencialmente nos bordos e em fracturas, e esta é materializada por anfíbola e, posteriormente, marcada por clorite+epídoto; por sua vez, os microfenocristais e micrólitos de plagioclase registam um incremento significativo da molécula albítica na sua composição, sendo apenas encontrados núcleos que preservam a composição primária; os óxidos de ferro disseminados na matriz apresentam, frequentemente, bordos corroídos, e, na proximidade destes, são encontrados cristais de titanite. A matriz destas rochas encontra-se substituída por filossilicatos, com características expansivas, possivelmente interestratificados clorite-esmectite. A presença destes interestratificados poderá resultar, assim, da alteração de vidro vulcânico. Este episódio é também caracterizado pelo preenchimento das vesículas por fases minerais neo-formadas, como é o caso dos interestratificados clorite-smectite, calcite e zeólitos cálcicos. Estas ocorrem frequentemente, também, sob a forma de precipitados que preenchem veios. Frequentemente, são também encontrados veios preenchidos por hematite+carbonatos+clorite, que marcam a transição para o segundo episódio de alteração identificado.

Na zona SE do depósito, assim como no *open pit*, são encontrados jaspes e *umbers* – rochas argilíticas ricas em (hidr)óxidos de Fe e Mn-, resultado de actividade exalativa hidrotermal de baixa tempertura. O desenvolvimento deste sistema hidrotermal está, possivelmente, controlado estruturalmente, e, perto do contacto com estas rochas exalativo-hidrotermais, observa-se, na matriz das rochas vulcânicas, uma forte impregnação de hematite, sendo apenas reconhecível alguns fenocristais de clinopiroxena. Na restante área, longe da influência directa das estruturas por onde os fluidos hidrotermais oxidantes, ricos em Fe e Mn, circulam, este episódio está marcado pela presença de veios de hematite+quartzo. São, também, frequentemente, observados veios de carbonatos calcíticos, que cortam estas rochas exalativas, localmente preenchendo fracturas *en echelon*, com brechificação sobreimposta.

A actividade hidrotermal relacionada com a mineralização de sulfuretos maciços (e a intensidade da alteração associada) é, também, controlada estruturalmente, mas também função da porosidade e permeabilidade das rochas vulcânicas, *i.e.* abundância e distribuição das vesículas. Com base em geotermómetros baseados na variabilidade composicional da clorite, é possível estimar temperaturas entre 250-400ºC, para o fluido hidrotermal relacionado com a mineralização.

De forma geral, distinguem-se diferentes fases de circulação de fluidos hidrotermais, dispostos numa rede de veios e filonetes, preenchidos por: I) *Qz+Py+Chl*; II) *Qz+Py+Ccp*; III) *Cb+Py/Qz+Zeol*; IV e V) *Qz* microcristalino. O controlo estrutural para a circulação destes fluidos hidrotermais é também reconhecível através das evidências de reabertura e sobreposição destas estádios de precipitados hidrotermais. A acompanhar a alteração hidrotermal associada à mineralização, ocorrem esporádicas disseminações de cristais euédricos, sub-microscópicos, de apatite, sugerindo uma contribuição de fluidos magmático-derivados, associados à cristalização das intrusões sub-vulcânicas doleríticas. Estas rochas apresentam também disseminações de apatite, assim como alguns sulfuretos (sub)microscópicos. Na área S/SE da mineralização, a alteração hidrotermal está marcada por uma silicificação fraca, disseminação de pirite e processos mais intensos de cloritização (comparando com as amostras recuperadas no *open pit*), com veios de quarto, clorite, pirite e, ocasionalmente, calcopirite. A partir dos dados de quimica mineral de grãos de chlorite, obtidos a partir destas amostras, é possível concluir que o fluido hidrotermal mineralizante, circulou a temperaturas entre os 200-400ºC, com valor mediano de ~270ºC. Por sua vez, nas amostras provenientes do *open-pit* são observáveis processos alteração hidrotermal marcados por silicificação mais intensos, acompanhados pela deposição de clorite, sob a

forma de agregados de granularidade reduzida, disseminação de pirite, e ocasionalmente de calcopirite e esfalerite. Em ambos os casos é possivel encontrar, por vezes, evidências mineralógicas atribuíveis ao primeiro estádio de alteração descrito (metassomatismo oceânico), nomeadamente micrólitos de plagioclase albitizados.

Durante a alteração hidrotermal, os balanços de massa que se estabelecem são, geralmente, negativos, com perdas de massa significativas, caracterizados por perda considerável em Si, Ca ou Mg, compatível com a decomposição das fases ferromagnesianas primárias e neo-formação de fases secundárias. Ganhos em Fe, acompanhados por Mg, indicam a presença de fluidos hidrotermais diluídos (misturados com água do mar), enquanto algumas zonas do *open-pit* são caracterizadas por ganhos em Fe, não acompanhados por ganhos em Mg, sugerindo a circulação de fluidos hidrotermais não diluídos. A estes domínios, registam também ganhos consideráveis em Cu, Zn, As, Ba e ainda em In, Sn, Tl e Cd, na ordem das dezenas de ppm, indicando ainda um *input* de fluidos tardios de oridem magmática, para o fluido hidrotermal, responsável pela mineralização.

É também possível observar veios de hematite, posteriores à alteração hidrotermal, revelando que, durante o colapso térmico do sistema hidrotermal, outro(s) episódio(s) exalativo-hidrotermal de baixa temperatura sejam responsáveis pela deposição de jaspes/*umbers*. Assim, a mesma fonte de calor que permite sustentar os sistemas produtivos hidrotermais representa também, a fonte de calor que alimenta outros sistemas, de mais baixa temperatura, favorecendo a recorrência de alguns estádios de evolução do sistema, em períodos temporais distintos.

Não obstante a amostragem abranger uma área significativa do depósito e permitir a caracterização da evolução do(s) sistema(s) hidrotermal/hidrotermais responsáveis pela formação deste depósito, uma amostragem mais completa, assim como a identificação e mapeamento das principais estruturas tectónicas presentes na área, permitiria a caracterização espacial do padrão de distribuição dos halos de alteração hidrotermal.

Por fim, a utilização dos índices CCPI, AI e dos $AI_{maiores}$ e $AI_{traço}$ corroboram os dados mineralógicos e texturais, traduzindo uma boa correlação entre os dados de geoquimica de rocha total com as modificações mineralógicas, texturais e composicionais descritas. Assim, a sua utilização afigura-se interessante na prospecção de mineralizações do tipo VMS para o ofiolito de Omã.

Palavras-chave: Ofiolito de Sumail, Omã, VMS, alteração hidrotermal, geotermometria, metalogenia

ABSTRACT

The Sumail ophiolite hosts numerous epi to syn-genetic massive sulphide mineralizations in its Cretaceous volcanic sequence. The Mandoos is one of the largest VMS deposits found in the ophiolite and the lack of detailed studies on its genesis makes it a prime case-study. Thus, this work aims to develop a mineralogical and geochemical characterization of the volcanic sequence that hosts the mineralization, in order to develop a metallogenetic model for the formation of the deposit, characterizing the hydrothermal alteration associated to the massive sulphide formation, the pinpoint of its volcanostratigraphic position and to develop geochemical criteria, helpful for mineral exploration purposes.

Considering the REE contents and patterns, and the HSFE contents, these volcanic rocks are considered part of the Lasail volcanic unit, which rocks derive from the partial melting of an already depleted DMM mantle source, which underwent a previous melt extraction, in a ridge setting. These are microporphyritic basaltic rocks, with tholeiitic affinities, with a primary mineralogy is characterized by augitic clinopyroxene and bytownitic to labradoritic feldspar microphenocrysts, set in a plagioclase microlite rich matrix, with disseminated Ti-rich magnetite crystals. Oceanic metasomatic alteration is pervasive and responsible for the alteration and replacement of the primary volcanic minerals by (Ca-)amphiboles+*Chl*+*Ep*, Ab and *Ttn* and by the alteration of volcanic glass to interlayered *Chl-Sme*, as well as other secondary mineral phases such as calcite and calcic-zeolites, as vesicles and fractures infills. Sub-volcanic intrusions (dolerites) act as heat sources that allow to sustain structurally controlled hydrothermal systems, in different periods of time. Low-temperature hydrothermal systems are responsible for late-developed *Hem*+Qz±Chl±*Cb* veins, throughout the sampled area, and, in the SE part of the deposit, for the deposition of jaspers and umbers. Overall, the hydrothermal alteration includes silicification, dissemination of pyrite and chloritization and, in most of the area it is associated to hydrothermal quartz veins, sometimes occurring with sulphides, distinguishing four different hydrothermal vein stages: i) *Qz*+*Py*, ii) *Qz*+*Py*+*Ccp*±*Sph* which are, sometimes, re-opened and *Cb*+*Py* or *Qz*+*Zeol* precipitate, denoting an evolution of the hydrothermal fluid; iii and iv) *Qz*. The hydrothermal system, responsible for the mineralization, is characterized by temperatures between 200-430 ºC; it's circulation is responsible for the development of different alteration facies, sometimes with preservation of oceanic metassomatic alteration effects, such as the albitized microlites. This is the result of the primary volcanic rocks permeability but, more importantly, the proximity to the structural features that act as fluid-flow channels. In extreme cases, the hydrothermal alteration is marked by intense brecciation, with hydrothermal quartz and sulphides-bearing veins, silicification and sulphides dissemination, revealing that the mineralization also took place as sub-seafloor replacement.

The lithogeochemical data is coherent with the mineralogical transformations, using the AI and CCPI indexes. Additionally, during the registered alteration stages, elements such as Ti, Zr, Ta, Yb, Y, Nb and Ta are considered to have an immobile behaviour, some of them showing a slight mobility, especially during hydrothermal alteration. Nevertheless, the established mass balances, during hydrothermal alteration, record negative balances. Nevertheless, Fe gains are usually accompanied by Mg additions, highlighting the presence of diluted fluids but, for the sampled area of the open pit, the presence of non-diluted hydrothermal fluids is inferred by gains in Fe (but not in Mg) and metals such as Cu and Zn. Also, gains in In, Cd, Sn and Tl, as well as *Ap* disseminations in hydrothermal altered samples, reveal an input of late-magmatic fluids into the hydrothermal system. Finally, the use of AI_{major} and AI_{trace} is found to be useful in distinguishing hydrothermal alteration, related to sulphide deposition, from regional metassomatic alteration, useful for exploration surveys.

Key-words: Sumail Ophiolite, Oman, VMS, hydrothermal alteration, geothermometry, metallogeny

ACRONYMS AND ABBREVIATIONS

Geochemical Features			
Rare Earth Elements	REE	Suprasubduction Zone	SSZ
Light Rare Earth Elements	LREE	Moho Transition Zone	MTZ
Heavy Rare Earth Elements	HREE	Depleted Mantle Source	DMM
High Field Strenght Elements	HSFE	C1 Chondrite	C1
Large Ion Litophile Elements	LILE	Primitive Mantle	PM
Mid-Ocean Ridge Basalts	MORB	Back-arc basins basalts	BABB
Normal Mid Ocean Ridge Basalts	N-MORB	Forearc Basin	FAB
Enriched Mid Ocean Ridge Basalts	E-MORB	Island Arc Tholeiites	IAT
Chlorite-Carbonate-Pyrite Index	CCPI	Ishikawa Alteration Index	AI

Minerals			
clinopyroxene	*Cpx*	actinolite	*Act*
clinoenstatite	*Cen*	albite	*Ab*
clinoferrosilite	*Cfs*	epidote	*Ep*
pigeonite	*Pgt*	chlorite	*Chl*
augite	*Aug*	titanite/sphene	*Ttn*
hedembergite	*Hd*	quartz	*Qz*
diposide	*Di*	hematite	*Hem*
enstatite	*En*	carbonates	*Cb*
ferrosilite	*Fe*	calcite	*Cal*
wollastonite	*Wo*	pyrite	*Py*
plagioclase (*s.l.*)	*Pl*	chalcopyrite	*Ccp*
magnetite	*Mgt*	sphalerite	*Sp*
titanium rich-Magnetite	*Ti-Mgt*	chlorite-smectite interstratificates	*Chl-Sme*
zeolite (group)	*Zeo*	apatite	*Ap*

Geology- various			
atoms per unit formula	apuf	North East	NE
parts per million	ppm	South West	SW
weight percent	*wt %*	Volcanic Associated Massive Sulfide	VAMS
Whole-rock	WR	Volcanic Hosted Massive Sulfide	VHMS
X-ray fluorescence	XRF	Vulcanogenic Massive Sulfide	VMS
Wave lenght X-ray fluorescence	WDXRF	Iberian Pyrite Belt	IPB
Inductively Coupled Plasma Mass Spectrometry	ICP-MS	Massive Sulfide	MS
Polarized light	PL	million years	M.y.
Reflected ligh	RL	Versatile Time-Domain Electromagnetic	VTEM
Parallel polars	PP	Mandoos	MD
Crossed polars	XP	Back Scatter Electrons	BSE
Million Tons	Mt	Bellow Detection Limit	BDL

Institutional			
Faculdade de Ciências da Universidade de Lisboa	FCUL	Sultan Qaboos University	SQU
Centre National de la Recherche Scientifique	CNRS	German University of Technology, Oman	GUTech
Comission on New Minerals and Mineral Names of the International Mineralogical Association			CNMMN-IMA

Others			
exempli graia /example	e.g.	*sensu strictu* /strict sense	*s.s.*
sensu lato /broad sense	*s.l.*	*Id est* /This is	*i.e.*

LIST OF FIGURES

LIST OF TABLES

CHAPTER I
INTRODUCTION

Volcanogenic massive sulphides (VMS) are epigenetic to syngenetic, stratabound/lenticular bodies of sulphide minerals, precipitated from hydrothermal fluids at or immediately below the sea-floor.

The term VMS implies a direct spatial, temporal or genetic relationship with volcanic activity and is distinguishable from other similar ore subtypes, like Volcanic Hosted Massive Sulphide (VHMS) or Volcanic Associated Massive Sulphides (VAMS), where that relationship is not straightforward (Hannington, 2014). These relationships include: I) controls on the occurrence of the orebodies within the volcanic structures and sequences; II) (sub)volcanic activity acting as a heat-source, producing high rates of heat advection, required to sustain (modified) sea-water circulation in the oceanic crust (convection being possible in presence of a quasi-isotropic permeability) and; III) source of metals, through interaction of the sea-water with the footwall volcanic rocks and, sometimes, with late-stage magmatic-derived fluids. Thus, the depth of the heat-source, the temporal and spatial distribution of permeability in the host-rocks as well as the tectonic activity represent the three major factors controlling the fluid-flow, discharge and the life span of a VMS-forming hydrothermal system (Hannington, 2014).

Lenticular-shaped massive sulphide bodies are mostly composed of pyrite, with subordinate amounts of chalcopyrite, sphalerite, bornite, tetrahedrite, among others. It usually lies above an inverted cone-shaped sulphide bearing anastomosed vein system, corresponding to the stringer or stockwork zone, which represent the fluid flow conducts that fed the hydrothermal ore system (Hannington, 2014). The interaction of these sea-water derived hydrothermal fluids with the footwall volcanic rocks results in a series of chemical reactions, that ultimately generate alteration haloes. These hydrothermal alteration haloes vary widely, even in the same ore district, depending on rock permeability, changes in fluid chemistry and, rock composition, as well as in other physical-chemical variables that control the rate and extension of mineral/textural transformations (Hannington, 2014). In general, hydrothermal alteration involves replacement of primary igneous minerals (*e.g.* pyroxenes, plagioclase, Fe(-Ti) oxides), and volcanic glass, by secondary mineral phases, stable at temperature and chemical environment, such as chlorite, epidote, carbonates, pyrite, albite, sericite, clay minerals and quartz or different forms of silica (chalcedony, opal). The degree of alteration is also very variable, ranging from weak, allowing the preservation of primary volcanic textures and rock-forming minerals, to pervasive and intense, with (almost complete) obliteration of primary textures and minerals.

Despite this wide range of variation, there are recognizable zonal arrangements related to the hydrothermal fluid circulation in the genesis of VMS deposits, characterized by particular types of mineral assemblages that allow the reconstitution of the main paths of fluid flow, sulphide deposition and water/rock reaction processes (Hannington, 2014). The recognition of hydrothermal alteration haloes is therefore critical to the development of exploration vectors, which allow the assessment of favourable exploration targets for VMS deposits.

The classification of VMS deposits can be made on different basis. Some classification schemes use their metal composition/contents as the main criteria (*e.g.* Franklin *et al*. 1981; Franklin *et al*., 2005; Barrie and Hannington, 1999), others consider their geological setting (Sawkins, 1976), or host-rock composition (*e.g.* Barrie and Hannington, 1999). An increasingly used classification is the one proposed by Barrie and Hannington (1999) and later modified by Franklin *et al* (2005). Therefore, in a first approach, five different type of VMS districts can be recognized: I) bimodal-mafic; II) mafic; III) pelitic-mafic; IV) bimodal-felsic; V) siliciclastic-felsic. These types are then sub-divided on the basis of their lithofacies association, providing a way of pinpointing the volcano-sedimentary environment of a specific deposit (Franklin *et al.*, 2005):

I). The bimodal-mafic VMS provinces (or districts) corresponds to incipient rift-related bimodal volcanic arcs, above intra-oceanic subduction (oceanic suprasubduction rifted arc), dominated by basalts but up to 25% of felsic rocks; pillowed and massive basaltic flows, felsic flows and domes with minor basaltic and felsic volcaniclastic rocks occur within sedimentary sequences dominated by graywackes, sandstones and shales, with local debris flows (e.g. Abitibi, Canada; Flin Flon, Canada).

II). The mafic type VMS provinces correlates with intra-oceanic back-arcs and mid-ocean ridges, ophiolite and ophiolite-like sequences, dominated by MORB-boninite and arc tholeiite sequences with prevailing pillowed and massive basaltic flows, minor felsic flows and/or domes, synvolcanic mafic dykes or sills. Minor sulphide-rich/reduced or hematite/oxidized argillite, chert or tuffs also occur (e.g. Konuto, Canada; Troodos, Cyprus; Sumail, Oman). At fast spreading ridges, high temperature fluids circulate at relatively shallow depths and the ore-forming systems tend to be small and/or short-lived or subjected to strong intermittency, due to the frequent volcanic eruptions that disrupt the hydrothermal paths and bury the sulphide accumulations; in such settings, hydrothermal fields and vents are rapidly displaced from their heat source. In slow-spreading ridges the magma supply rate is lower, hence, hydrothermal systems are supported by long-lived high heat flow will have the chance to produce larger sulphide accumulations.

III). The pelitic-mafic corresponds to mature, basalt-pelite dominated back-arc sequences, in juvenile accreted arc assemblages, typically devoid of felsic volcanic rocks. The sedimentary sequences are often of distal flysch type, but they can include carbonaceous shales, siltstones and minor sandstones, besides mafic sills (e.g. Outukumpo, Finland; Besshi district, Japan).

IV). The bimodal-felsic association is common in continental margin arcs and related back-arcs in which felsic volcaniclastic rocks dominate, along with minor basaltic/andesitic flows and clastic sedimentary rocks (e.g. Pilbara, Australia; Eskay Creek, Canada).

V). Siliciclastic-felsic type compares to mature epicontinental back-arcs where siliciclastic sequences prevail over felsic volcaniclastic and/or massive flows or domes with even minor mafic (tholeiitic to alkaline) flows or sills; often the sedimentary sequences contain Fe-, Mn- Ca- and Ba-rich chemiogenic sedimentary rocks/sediments (e.g. Iberian Pyrite Belt, Portugal and Spain; Lachlan Fold Belt, Mexico).

Another commonly used classification scheme distinguishes three types of VMS deposits: i) Besshi type VMS, broadly correlated to the pelitic-mafic type VMS; ii) Kuroko-type VMS deposits, corresponding to the bimodal mafic type; and iii) Cyprus-type, representing obducted VMS deposits, i.e. of the mafic type.

The Sumail ophiolite hosts of a series of VMS occurrences, classified as mafic-type VMS. These are mostly found in the northern part of Oman, along the Batinah Coast, in the Sohar region, some of them

irregularly mined since the Bronze Age (for Cu and, where gossanized sulphide mounds exist, for Au). The most important deposits are Aarja, Hatta, Lasail, Bayda, Shinas, Al Bishara, Rakha and Mandoos. These deposits are typical Cyprus-type ore systems and totalize 30 to 50Mt of ores (Galley *et al*., 2007; Franklin *et al*., 2005) with an average copper content of 2.3% (Gilgen *et al*., 2014), comparable to values for the Troodos Ophiolite in Cyprus. The known orebodies are, usually, massive pyritic masses with minor chalcopyrite and sphalerite, hosted in the extrusive Upper Cretaceous (Cenomanian to Turonian) sequence. These mineralizations are thought to have been formed in black smokers sulphide mounds and hydrothermal fields, analogous to those found in present-day oceanic settings (e.g. East Pacific Rise).

The Mandoos deposit was identified in 2009, when Mawarid Mining conducted the first exploration survey in the area, through an airborne VTEM (versatile time-domain electromagnetic) geophysical assessment, during which three other targets were defined. A later geological exploration survey, including an adequate drilling program, confirmed the existence of massive sulphides in three of the four previously delimited targets, Mandoos 1 being the bigger and copper richer target. The fourth target, Mandoos 4, did not result in the discovery of a VMS orebody (Mawarid Mining, 2014).

The mining operations at Mandoos 1 started in October 2011, in an open-pit, that reached the maximum exploitable extension in mid-February 2015, when the mine finally closed, due to financial/economic factors. Although the mining activities were abandoned there is still some potential to expand exploitation underground and mine about the remainder of the orebody, an option which is currently under consideration. According to Mawarid Mining, the deposit contains about 8 Mt of copper sulphide ore, with 5 Mt in reserves at 1.8% Cu (Rob Willis, *pers. comm.* to Ana Jesus, February, 2015).

The main objective of this project is to provide a study of the volcanic rocks forming the hanging and footwall sequence, hosting the Mandoos massive sulphide ores. The petrographic, mineralogical and geochemical characterization of a representative set of samples, collected at the open pit and 6 different drill cores, allowed: I) the discrimination of the petrological (igneous) processes responsible for the genesis of these rocks, especially regarding the tectonic setting in which the rocks erupted (MORB *s.l. vs* SSZ signatures); II) the correct assignment of a volcanic-stratigraphic position to the deposit, and III) the distinction between the inprints of the low-temperature oceanic metasomatic alteration from those due to hydrothermal processes, directly related to the massive sulphide deposition (*i.e.* hydrothermal alteration/mineralization haloes). The analysis of their extent and nature, as well as the crucial factors for their development, represent significant inputs to an intended metallogenic model of the deposit, providing also crucial information to further exploration surveys and economic feasibility studies.

CHAPTER II
GEOLOGICAL SETTING

II.1. REGIONAL SETTING– OPHIOLITE OBDUCTION AND GEODYNAMIC MODELS

The Sumail (also referred as Semail or Samail) ophiolite constitutes the best preserved and less deformed ophiolitic sequence in the world. It is found in the Oman mountains, in a ~600 km long, and up to 150-wide belt and includes a complete section of the oceanic crust and underlying mantle (10-15 km thick), one of the Neo-Tethyan Oceanic basins. This oceanic crust fragment is part of the Alpine-Himalayan fold-thrust collisional belt that extends from the Mediterranean to the Far East (Lippard *et al.*, 1986; Goodenough *et al*., 2014; Hou & Zhang, 2015) (Figure II. 1). It is one of the many Tethyan ophiolites, formed during the oceanic-continental collision related to the closing of the Neo-Tethys ocean, result of the Africa/Nubia and Eurasia tectonic plate collision, coeval of the opening of the South Atlantic Ocean (Lippard *et al*., 1986).

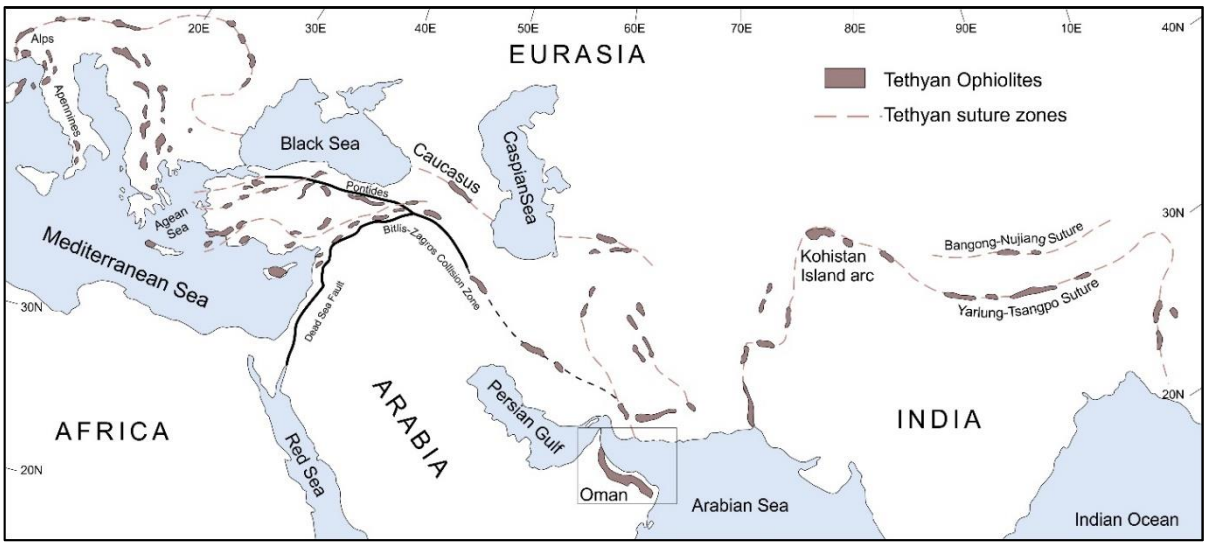

Figure II.1- Distribution of the major Tethyan suture zones and ophiolites, found in the Alpine-Himalayan collisional belt *Adapted from Dilek & Furnes (2009).*

II.1.1. MAIN UNITS OF THE SUMAIL OPHIOLITE

In the Sumail, a complete ophiolitic sequence (as defined in the Penrose Conference, 1972) is preserved (Figure 2 and 3). Deformation is not widespread and resulted in minor doming and thrusting during obduction (Gilgen *et al.*, 2014). Instead, the deformation was strongly partitioned into a basal thrust and regional shear-zones (Boudier *et al.*, 1988). Thus, this ophiolite preserves the main structure of the spreading centres, as well as the lithostratigraphic relationships, reason why it is widely used as an analogue for understanding present day oceanic crustal processes (Nicolas *et al.*, 2000; Godard *et al*., 2006; Gilgen *et al.*, 2014).

The mantle portion comprises mantle peridotites, mainly harzburgites, originated from partial melting of fertile spinel lherzolites; other peridotitic rocks include dunites and minor lherzolites, displaying various tectonic and plastic flow deformation (micro)structures, as well as evidence of various serpentinization episodes (Boudier, 1985). The Moho transition zone (MTZ) has a variable thickness, from ten to hundreds of meters. It represents a level of magmatic exchange between asthenospheric mantle and the oceanic crust, mainly composed of dunite with various types of segregations and intrusions (gabbroic, piroxenitic and chromitites) (Boudier, 1995).

Above the MTZ, the lowermost crustal section composed of a gabbroic suite, layered and foliated-olivine gabbros, troctolites, wehrlites (Boudier, 1996; Boudier, 2000). The layered gabbros are found in the lower part of the crustal section and includes alternating layers of gabbroic cummulates, anorthosite and (ultra-)mafic portions: foliation is commonly defined by plagioclase laths and elongated crystals, corresponding to magmatic flow and compaction structures (Boudier, 1996). The upper gabbroic section is composed of foliated gabbros, having a linear and planar fabric. The foliation changes gradually from flat lying- in the layered gabbros- to a steeper dip towards the foliated gabbros, where it is almost parallel to the sheeted dykes. In some areas, the foliation in the upper gabbros disappears, forming patches of amphibole-rich isotropic gabbros in the root zone of the sheeted dykes (Boudier, 2000).

The top of the gabbroic sequence, near (or at) the sheeted dyke transition, is intruded by trondhjemites, which genesis is still under debate. They are commonly interpreted as late-stage, extreme differentiates of basaltic melts (*e.g.* Lippard *et al*., 1986), thus providing a good estimate of the age of the ophiolite. Nevertheless, some authors distinguish three different type of trondhjemites (Rollinson, 2006): (1) the earlier ones, formed as a result of partial melting of MORB-like gabbros, previously hydrated by sea-water derived fluids (second stage melts); (2) later trondjhemites result of differentiation of a magma produced from re-melting of a depleted harzburgitic mantle source; and (3) mantle-hosted trondhjemites formed by mixing or contamination processes, during or immediately following the emplacement of ophiolites (*e.g.* Rollinson, 2006). This implies that the trondhjemites found throughout the ophiolite are not providing the same age, since they originate from diachronic geological processes, challenging the average age of ~95Ma, often considered (*e.g.* Tilton, 1981; Lippard *et al.*, 1986; Boudier *et al.*, 1998; Searle and Cox, 1999; Searle *et al.*, 2003; Warren *et al.*, 2005; Dilek & Furnes, 2009; Goodenough *et al*., 2010; Dilek & Furnes, 2011).

The uppermost part of the gabbroic section of the crust is crosscut by dolerite dykes, particularly at the transition zone to the sheeted dykes sequence. The dykes represent the feeder channels of the overlying extrusive magmatic sequence. The extrusive rocks comprise a suite of Cretaceous volcanic rocks, mostly pillow lavas and massive flows, that host numerous epigenetic volcanic massive sulphide orebodies (VMS). The volcanic rocks are affected by a set of normal faults, which are later intruded by un-deformed dykes, sometimes displaying evidence of hydrothermal alteration. This suggests that these faults were related to seafloor extension and contemporaneous volcanism, as well as hydrothermal

activity- with sulphide deposition (Gilgen *et al.*, 2014). The volcanic rocks are often overlain by pelagic sedimentary rocks, with Cenomanian to Turonian microfossils (Fleet & Robertson, 1980).

Considering the accepted U-Pb zircon ages for several intrusive bodies at different levels in the ophiolitic section, ophiolite (*e.g.*, Warren *et al.*, 2005), and the combination with the microfossils from pelagic sediments, it is possible to infer that sea-floor volcanism was active for 10 M.y., between 98.8 and ~89 M.y. (Gilgen *et al.*, 2014).

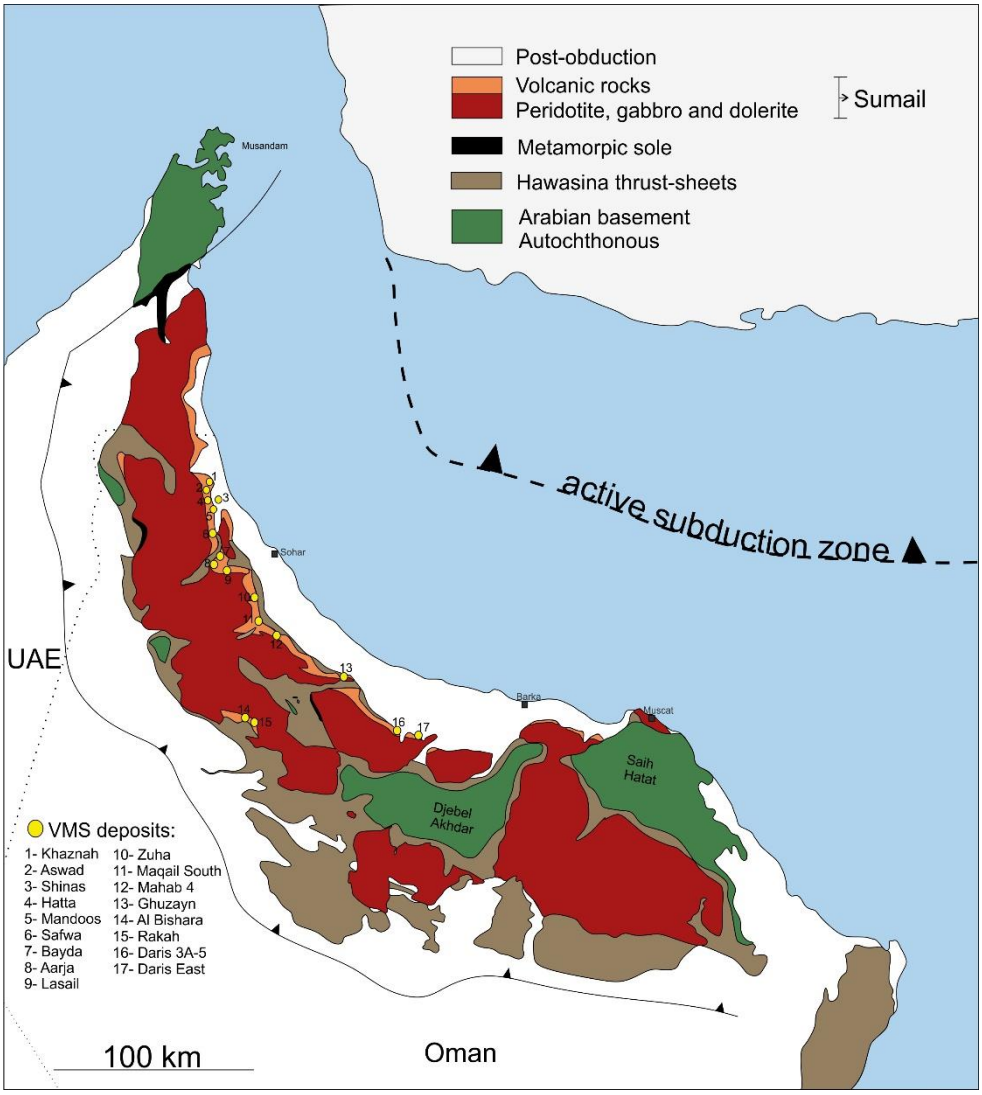

Figure II.2- Geological map of the Sumail ophiolite showing the main VMS deposits found in Oman, associated with the Cretaceous volcanism. Adapted from Boudier *et al.* (2000) and *Gilgen et al.* (2014).

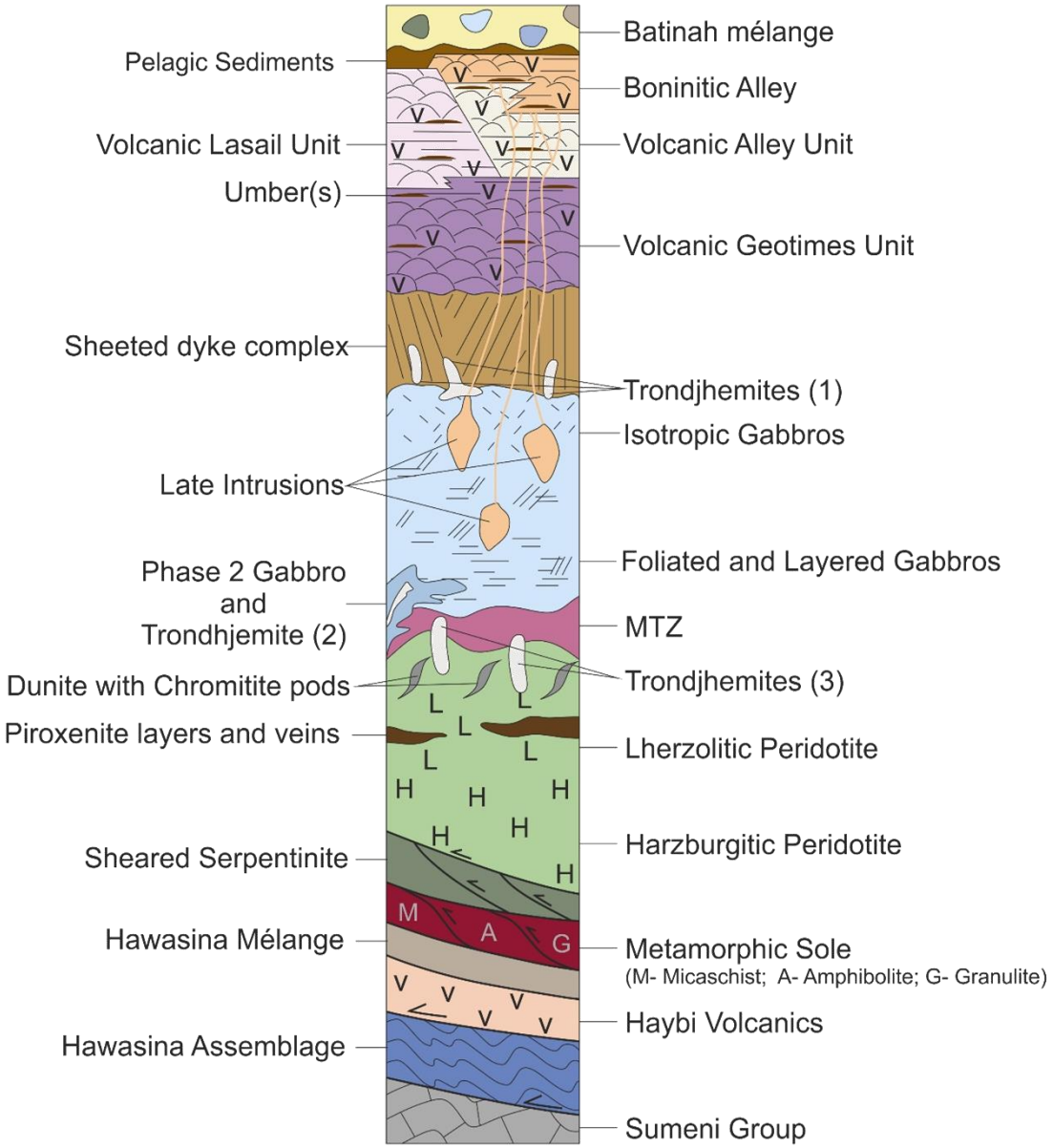

Figure II.3- Columnar section showing the complete ophiolitic sequence found in the Sumail ophiolite. *Adapted from Dilek & Furnes (2009), Goodenough et al. (2014) and Gilgen et al. (2014).*

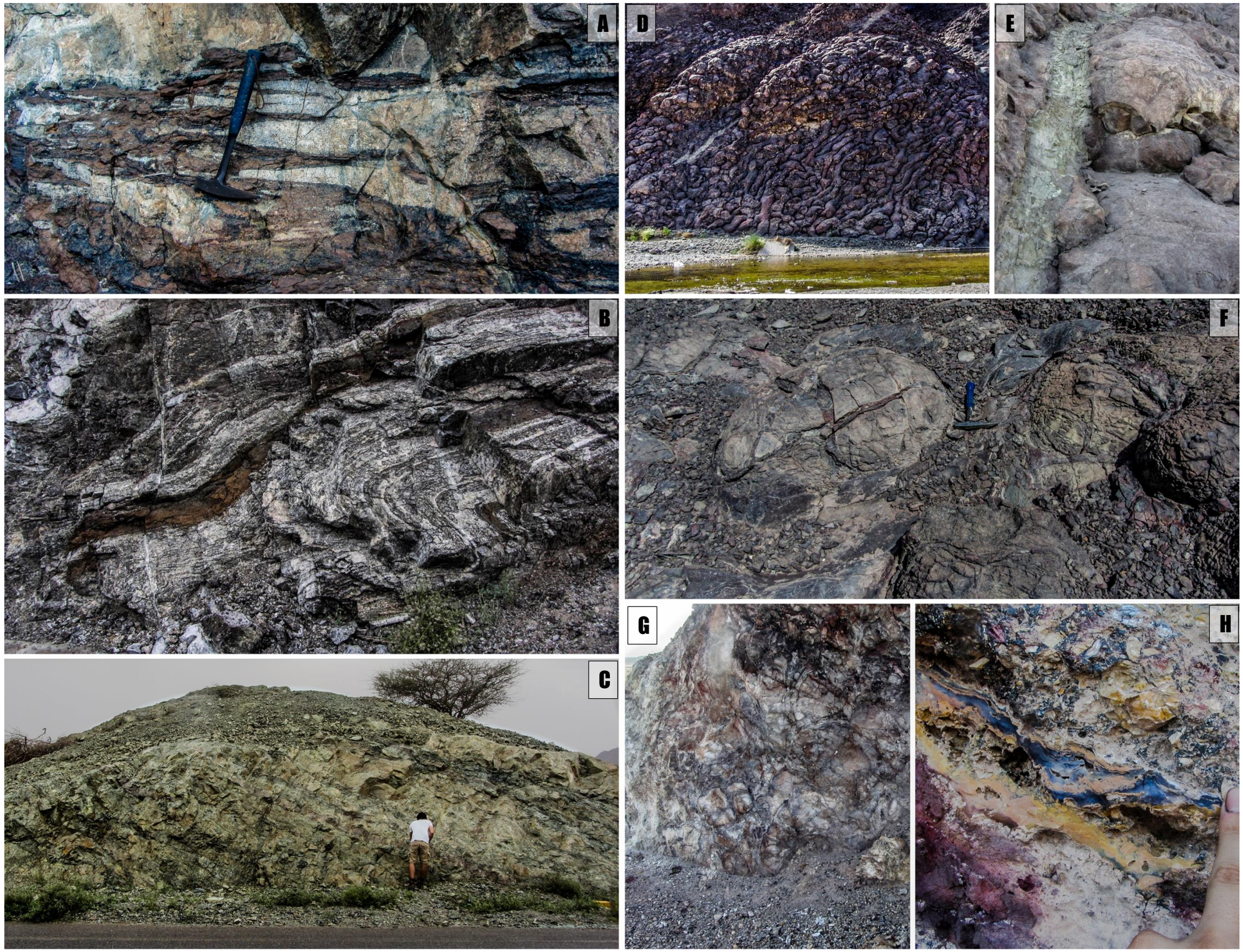

Figure II.4- Field photographies of key parts of the ophiolite (A) Wehrlite dykes and pods intruding the lower gabbroic sequence, near the MTZ (Wadi Al Abyad, Nakhl region); (B) Layered gabbro, showing syn-magmatic deformation (Wadi Al Abyad, Nakhl region); (C) Sheeted dyke outcrop (Wadi Al Jizzi, Sohar region); (D) Geotimes pillow-lavas outcrop (Wadi Al Jizzi, Sohar region); (E) Geotimes pillow-lavas crisscrossed by a fault zone with evidences of hydrothermal circulation – presence of epidote (Wadi Al Jizzi, Sohar region); (F) Pelagic Sediments overlying pillow-lavas (near Zuha,Sohar region); (G) Gossanized and silicified pillow-lavas outcrop (Al Ghuzayn, Al Batinah region); (H) Detail of gossan, with opal bearing veins (Al Ghuzayn, Al Batinah region)

II.1.2. GEODYNAMIC EVOLUTION

The opening of the Neo-Tethys and the Hawasina basin began in the mid-Permian, with the intracontinental rifting of the Gondwana, related to the closure of the Paleo-Tethys (Muttoni *et al.*, 2009; Berra *et al.*, 2016; Németh *et al*., 2016). The intracontinental rifting is marked by bimodal alkaline volcanism (Haiby volcanics), along with siliciclastic rocks and carbonates sedimentation, part of the Haybi Complex/Hamrat Duru group (Cox, 2000; Searl, 2007). Lateral facies variations account for the formation of shelf carbonates of the Sumeni Group and progressively distal siliciclastic slope and basin facies from the Hawasina Group (*e.g.* Searl, 2007 and references therein). The inexistence of calc-alkaline magmatism in the Arabian margin, as well as the evolution of the sedimentary record, supports it behaved as a passive margin, until mid-Cretaceous (Searl, 2007). This excludes the possibility of a SW-dipping subduction zone, where oceanic crust was consumed, as proposed by Gregory *et al*., (1998) and Gray *et al*., (2000) (Searl, 2007).

In the early-Jurassic, alkaline magmatism ceased, giving way to sea-floor spreading in the Late-Cretaceous. The evolution of the extrusive sequence (MORB-like to arc/boninitic signatures), together with the petrological and geochemical features of the mantellic and gabbroic sequence and the presence of the late intrusive bodies in the MTZ (*e.g.* Yamaski *et al.*, 2006; Goodenough *et al.*, 2010), sustain, until today, a long-lasting and vivid debate regarding the geodynamic setting of the Sumail – whether a mid-ocean ridge (*e.g.* Boudier *et al.*, 1985; Boudier and Nicolas, 1995) or a suprasubduction zone setting (SSZ) (*e.g.* Pearce *et al.*, 1981; Alabaster *et al*., 1982; Lippard *et al*., 1986). The first volcanic phase (V1), represented by the lowermost Geotimes unit, is attributed to a MORB-like setting or a back-arc basin, while the V2 volcanic phase, with arc-like geochemical signatures and the overlying Alley and boninitic volcanic rocks reveals an arc-like setting. These variations have been interpreted as a result of an intra-oceanic thrusting and subduction initiation, thus modifying the magma source zone.

The intra-oceanic thrusting has long been understood as the mechanism that enabled the formation of the metamorphic sole that underlies the ophiolite (Breton *et al*., 2004). The metamorphic sole is a discrete ~200-300m thick thrust sheet, characterized by an inverted metamorphic gradient, from granulites to amphibolite gneisses and green-schist facies metasedimentary rocks at the bottom (quartzites, volcaniclastic and carbonates) (Cox, 2000; Searl *et al*., 2003, Breton *et al.*, 2004; Searl, 2007). The sole is present at the base of the entire ophiolite and the deformation fabrics are parallel to the Sumail thrust (Searl, 1980; Cox, 2000). There is evidence for localized partial melting within the sole, with the presence of tonalitic intrusions in the granulitic rocks (Cox, 2000). The heat source for the formation of the metamorphic sole is considered to be the downward heat transfer from young and hot over-thrusted mantellic rocks (>600ºC) (Ishikawa *et al*., 2005). Geochemical data from the metabasaltic rocks that compose the sole indicates that these rocks are derived from Triasic to Jurassic tholeiitic rocks of the Haybi volcanics, as well as MORB-like oceanic crust, that formed the Neo-Tethyan oceanic crust (Cox, 2000, Searl, 2007). This intra oceanic thrusting explains the presence of granitic rocks, which intrude the mantle and gabbroic sequence of the ophiolite. These peraluminous granitic intrusions are derived from a mixed-source, which are the Haiby complex volcanic and sedimentary rocks, preserved as green-schists to granulite-facies rocks (Cox, 2000; Searl *et al*., 2003; Searl, 2007). The fluids released from the sole may also explain the geochemical variation of the ophiolite volcanic rocks, due to contamination and metassomatic fertilization of the mantle wedge, and thus accounting for the low-Ti andesitic volcanism (Alley) and of the boninites found in the volcanic sequence (Ishikawa *et al.*, 2002; 2005; Breton *et al*., 2004). Notwithstanding, other authors propose that this geochemical variation is not attributed to intra-oceanic thrusting, and consequent arc-formation, but to sea-water contamination into residual and shallow peridotitic rocks. The partial (re-)melting of these hydrothermally altered (by sea-water derived fluids) mantle rocks experience P-T-H_2O evolutionary trends that resemble the

petrogenetic conditions for andesitic-boninitic magma genesis, usually attributed to subduction zones (Benoit *et al.*, 1999; Nonnotte *et al*., 2005)

During obduction of the ophiolite, *c.a.* 95 M.y., the Arabian continental crust was subducted, up to depths of about 80km. These rocks were brought into eclogite facies conditions (omphacite+garnet+glaucophane+phengite) along with metapelitic rocks (garnet+chloritoid), defining a clockwise P-T path, with estimated peak metamorphic conditions of 20-23±2.5 kbar and 540±75ºC at 82-79 M.y. (Searl and Cox, 1999; Searl *et al.*, 2003, Warren *et al.*, 2005). These HP-LT (High Pressure-Low Temperautre) rocks, outcropping in the Saih Hatat window, are also associated to blue schists and carpatholite-kaolinite schists. In this area (Saih Hatat), the metamorphic grade increases towards NE, where the eclogites occur as mafic boudins in the As Sifah sub-window. This subduction was "chocked" and exhumation was triggered by the positive buoyancy of the Arabic continental crust, as well as the extension of the ophiolite nappe (Cox, 2000; Sear *et al*., 2003).

The ophiolite and its coupled metamorphic sole are underlain by sedimentary allochthonous, highly imbricate nappes- Hawasina nappes. These consist on Mesozoic hemi-pelagic and pelagic sediments that show complex geometries with several evidences of syn-emplacement folding phases, and low-grade metamorphism (greenschists facies). The Hawasina-nappes are formed by three lower thrust sheets of proximal facies turbiditic sediments with a variable, usually kilometric, thickness with minor limestone breccias, pelagic sediments, basaltic sills and volcanic layers (Lippard *et al*., 1986). It is divided into four different formations: the Halfa and Haliw formations, the lower and more deformed, consisting in highly deformed upper Triasic to lower-Cretaceous cherts and thin pelagic limestones; Permo-Triasic limestones, the Oman Exotics; redeposited upper Triasic limestone breccias and pelagic sediments from the Al Aridh formation (Lippard, *et al.*, 1986; Cox, 2000).

The Batinah nappe is structurally overlying the Sumail mantelic and crustal ophiolitic sections, although it is accepted that this group (Batinah group), divided in a lower, Triasic to Jurassic portion- Sakhin-, and upper, early/mid-Jurassic to Cretaceous- Salahi-, was part of the Hawasina allochthonous; initially overridden by the ophiolite, it was thrusted above the Sumail during the last stages of the emplacement (Cox, 2000).

The combination of the isostatic rebound and the emplacement of the nappes resulted in a marine regression, exposing the ophiolitic sequence. Hence, a late Maastrichtian unconformity is found, overlain by rudist-bearing beach deposits and later (Paleocene to mid/late Eocene) shallow marine fossiliferous carbonates. This carbonate sedimentation prevailed until the Oligocene, with marine carbonates (Lippard *et al.*, 1986).

In the Miocene, the uplift related deformation phase, warped the whole sequence into large scale open folds, caused by a biaxial compression. Following the deformation phase, an erosional event lasted until the Anthropocene, with the formation of thick piedmont deposits, alluvial, coastal, aeolian, Sabkah deposits (Bathinah coast deposits) and over 4km of cenozoic molasses representing ~100 000km^3 of sediments (Lippard *et al.*, 1986).

Nevertheless, some questions remain unsolved, especially regarding the driving mechanisms that explain the transition of the passive margin to an active margin, with the obduction/subduction of the Hawasina oceanic crust and the lead edge of the Arabian plate, respectively. Despite this, some authors related this transition of kinematic change in the plates movement with the anticlockwise rotation of the African plate, associated to the opening of the South Atlantic Ocean, during the Cretaceous (Coleman, 1981; Michard *et al.*, 1991; Breton *et* al., 2004; Burg, 2015). Other topics, such as the geochemical variation of the extrusive sequence and its geodynamic setting remain widely debated and unsolved.

II.2. VOLCANOSTRATIGRAPHY, TECTONIC SETTING AND MS ACCUMULATION

The volcanostratigraphy of the extrusive sequence of the Sumail ophiolite has long been studied and debated. The volcanic sequence is made up of different volcanostratigraphic units formed in overlapping volcanic centres, in a set of spreading axis, and later off-axis setting. The majority of the research was developed in the northern part of Oman, where the volcanic sequence is best exposed, aiming to define a group of mappable and distinct volcanic units, with distinctive features. Alabaster *et al.* (1982) defined five different volcanic units in the Bayda-Aarja-Lasail area and provided field, petrographic and geochemical criteria to distinguish them. Several authors have claimed that the field criteria is insufficient to distinguish them outside the same area, mapped by Alabaster *et al.* (1982). None of the later works on the volcanostratigraphy of the ophiolite defined more than five different units. In 2003, Godard *et al.* proposed a new classification, defining three different volcanic units based on geochemical data and paleomagnetic data, correlating its volcanic units with the ones defined by Alabaster *et al.* (1982). Nonetheless, the volcanostratigraphy proposed by Alabaster *et al.* (1982) remains as the most widely accepted and applied. This volcanic sequence is thus divided into five different units:

I) **Geotimes**, the lowermost unit, directly overlies the co-magmatic sheeted dyke complex. It is composed of 0.75-1km thick sequence of aphyric tubular basaltic to occasional andesitic large pillow lavas with subordinated aphyric massive flows, pillow breccias and hyaloclastites (Figure II.4 [D]). The red/brownish hematitic alteration is one of the diagnostic field criteria. Geochemically, these lavas are slightly depleted in incompatible elements compared to N-MORB, namely HFSE such as Nb and Ta. (Alabaster *et al.*, 1982; Lippard *et al.*, 1986; Godard *et al.*, 2003; Gilgen *et al.*, 2014).

II) The **Lasail unit** comprises grey to pale greenish, basaltic to andesitic smaller pillow lavas and frequent massive flows with porphyritic texture- olivine, clinopyroxene and plagioclase phenocrysts- with a thickness of ~0.75km. The lavas are depleted in LREEs and incompatible elements, compared to N-MORB and the concentrations in Zr and other refractory elements are lower than Geotimes' lavas. Alabaster *et al*. (1982) noted that the Lasail unit is only present in some areas of the ophiolite and interpreted them as seamounts, overlying the Geotimes unit, whereas Godard *et al*. (2003), considered the Lasail equivalent unit (V2-1) to be present throughout the entire ophiolite. Alabaster and Pearce (1985) defined the transition of Geotimes/Lasail as transitional and Kusano *et al*. (2012) described Geotimes and Lasail unit as being interdigitated, considering Lasail a sub-unit of Geotimes (Kusano *et al*., 2012; Gilgen *et al*., 2014).

III) The **Alley unit** includes a ~0.75km thick sequence of grey or brown-coloured, meter-sized amygdaloidal microporphyritic basaltic to rhyolitic pillow lavas that overlie the Lasail and, sometimes, the Geotimes unit. These amygdules and vesicles are commonly filled with zeolites and celadonite, the clinopyroxene and plagioclase microphenocrysts sometimes developing glomerophyric textures. Poly and monomict breccias are common. They are characterized by a REE pattern similar to Lasail's with slighter higher REE concentrations. Geochemically, the distinction between Lasail and Alley consists in the latter having lower Cr concentrations and higher Zr contents.

IV) The **clinopyroxene-phyric unit** occurs as small basaltic porphyritic flows with abundant clinopyroxene phenocrysts. They show low Zr and Ti concentrations and high Cr contents.

V) The **Salahi unit** comprises alkaline to transitional massive thick flows, that regularly form joint columns and occurs only at one location.

Ishikawa *et al.* (2002) reported boninitic lava outcrops, associated to Alley lavas, and recent volcanostratigraphic reviews (*e.g.* Gilgen *et al.*, 2014) found them to have a widespread and regional

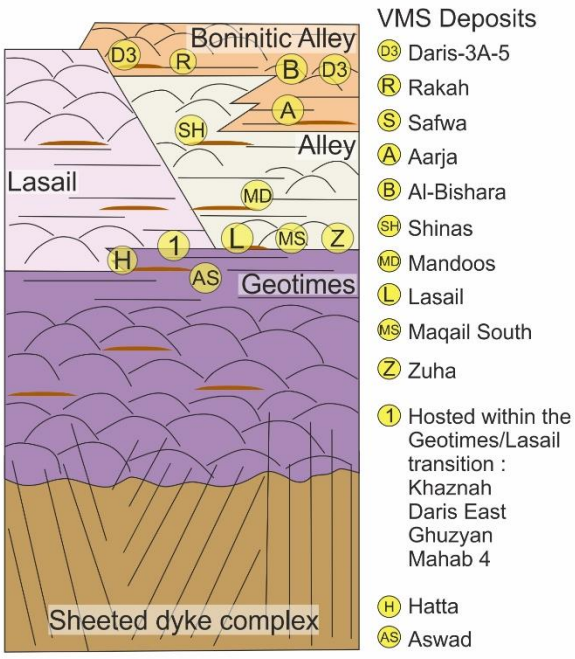

Figure II.5- Columnar section showing the different volcanic units found in the extrusive portion of the Sumail ophiolite and the VMS deposits found within that sequence, in their volcanostratigraphic positions. *Adapted from Gilgen et al. (2014).*

extent, defining the Boninitic Alley unit. The question remains, whether he boninite occurrences belong to the same unit or not. In general, they are vesicular pillow lavas and massive flows, several meters thick, with porphyritic texture. The phenocrysts and microphenocrysts are composed of orthopyroxene, clinopyroxene, olivine and chrome-spinel. This Boninitic Alley unit is macroscopically and mineralogically similar and equivalent to the clinopyroxene-phyric unit, defined by Alabaster *et al.* (1982).

These new volcanostratigraphic reviews (Gilgen *et al*., 2014) distinguish four main volcanic units, comprising, from bottom to top, the Geotimes, Lasail, Alley and Boninitic Alley units, which correspond to the division accepted and followed in this work (Figure II. 5).

The Geotimes unit erupted in a fast spreading ridge setting (Alabaster *et al.*, 1982; Lippard *et al.*, 1986; Kusano *et al.*, 2012; Gilgen *et al.*, 2014). The nature of this spreading ridge is under debated: a typical mid-ocean ridge (Boudier *et al.*, 1997; Godard *et al.*, 2006) or a suprasubduction marginal basin (Alabaster *et al.*, 1982; Lippard *et al.*, 1986). The Lasail unit shows a transitional geochemical nature, between ridge and arc-like geochemical affinity (Alabaster *e tal*, 1982; Searl, 2007). The more evolved compositions suggest an off-axis volcanism, occasionally influenced by on-axis volcanism, resulting into the interdigitated of both units (Gilgen *et al*., 2014), although some authors still debate if their geochemical signature marks a SSZ-signature. It is widely accepted that the Alley unit erupted in a suprasubduction setting, although the nature of the subduction is itself debated. The more consensual idea is that the subduction zone was already established when Geotimes erupted (Alabaster *et al.*, 1982; Lippard *et al.*, 1986; Godard *et al.*, 2003). The Boninitic Alley unit is altogether similar to other boninites in numerous modern-day tectonic settings related to spreading ridges, like the Neogene boninites in the northern termination of the Tonga Trench (Gilgen *et al.*, 2014 and citations therein), interpreted as the interference of the NW bifurcation of the Lau spreading ridge with the Tonga trench. Together, the Lasail and the Alley unit are considered to form a coherent sequence, as transitional lavas from a N-MORB-like geochemical signature (Geotimes) to boninitic (Boninitic Alley). Nevertheless, some authors propose that this geochemical variation (MORB-like to arc-like signatures) is assigned to a range

of variation of the peridotitic rocks alteration, induced by sea-water derived fluids, whose partial melting generates andesitic-boninitic-lile magmas, as previously mentioned.

The main horizon for VMS exploration was thought to be the Geotimes/Lasail contact and, to a minor extent, the Geotimes-Alley, defining the two major productive periods, in terms of VMS formation (Gilgen *et al.*, 2014). The first comprises the period after the Geotimes unit extrusion, in which the spreading center and off-axis (sub)volcanic activity acted as heat sources for the hydrothermal convection and sulphide precipitation, forming at least 7 MS deposits. The Geotimes eruption was intermittent, allowing the formation of, at least, one intra-Geotimes VMS deposit, in the volcanic quiescence periods. The Lasail off-axis volcanism later covered some of the deposits. The fact that Lasail lavas erupted in a possible off-axis setting, thus lacking a proper heat source, possibly explains the absence of intra-Lasail sulphide accumulations. The second major period for sulphide accumulations and productive hydrothermal systems to develop initiates with the Alley and Boninitic Alley extrusion. The Alley unit eruption covers longer-lived hydrothermal systems that originated deposits hosted in the Geotimes-Alley transition but the period between Alley volcanic activity generated at least one major sulphide accumulation system- Shinas. The existence of, at least, four major deposits hosted in the Boninitic Alley unit shows that the intermittence of this volcanism also allowed several important sulphide accumulations. The period between sulphide accumulation and its "sealing" is also accountable for oceanic-oxidation events, with the development of oceanic weathering profiles in the sulphide body.

New-found deposits and the re-examination of the volcanostratigraphic controls of massive sulphide occurrences, using clinopyroxene and whole-rock geochemistry, of the footwall and hanging wall of several VMS deposits, demonstrates that the idea that there were only two main periods of time for MS accumulation is not suitable (Gilgen *et al.*, 2014). Although most of the sulphide ores are, indeed, hosted in the Geotimes/Lasail and Geotimes/Alley transition, numerous deposits (including some of the most recent discoveries) are hosted within volcanic units, such as the Aswad deposit (Geotimes), Shinas (Alley) or the Daris-3A-5, Rakah and Safwa deposits (Boninitic Alley) (Figure II.5). This suggests that all hiatus in the volcanic activity (contacts between units, umbers or cherts) represent potential periods in which hydrothermal activity and sulphide accumulation was possible, and that horizon may, thus, host a MS deposit.

II.2.1. THE MANDOOS DEPOSIT

The Mandoos deposit, is found near the Sohar, beneath eight to thirty-four-meter-thick *wadi* fluvial gravels within a volcanic sequence which is not assigned to any volcanic unit, in the volcanostratigraphic sequence. The magnetic data recovered from the exploration surveys suggests that this deposit is likely to be intra-Alley or hosted within the Lasail volcanic unit, consisting in pillow lavas and massive flows (Mawarid Mining, 2014). The massive sulphide body consists of a pyritic mass, including minor chalcopyrite and sphalerite, presenting evidence for multiple brecciation events; with a variable thickness (up to 60 m thick in the northernmost area, decreasing towards south), extending 250m (in length) to the south area, this massive sulphide orebody was interpreted as being formed in a topographic depression or a *graben*, later affected by sea-water oxidation processes. The hydrothermal alteration is characterized by the presence of carbonates, albite, chlorite, quartz and smectite (Gilgen *et al*., 2014). Quartz and sulphide veins form a discreet stockwork, within silicified basalts. The hanging wall shows less alteration, possibly related to alteration processes distinct from those that acted upon the footwall rocks. Like for most of the recently discovered VMS deposits in Oman, there are no detailed studies for Mandoos and consistent published data is lacking. Therefore, its size and unknown volcanostratigraphic position make it an excelent case study within the Omani scenario, from where a relevant contribution to the understanding of mafic hosted-type deposits may be expected.

CHAPTER III
LABORATORIAL AND ANALYTICAL PROCEDURES

The laboratiorial and sample preparation work carried out during this study included several stages: (I) drill-core re-logging and sampling; (II) sample lab processing; (III) petrography; (IV) mineral chemistry; and (V) whole-rock geochemistry.

Drill c.ore re-logging and sampling

Six drill cores were sampled in the Mawarid drill core deposit, in March 2016, representing different sectors of the deposit: (I) MD 174 the "central" zone; (II) MD150 and MD178 from the lower/SW central zone; and (III) the MD 431, MD430 and MD429 set, located in the most southwestern part of the deposit (Appendix I). These were chosen considering drill core availability and good preservation. Indeed, drill core deterioration was a major conditioning factor to the sampling objectives.

Re-logging took place from end of March to mid-April in GUtech facilities. This work made it possible to recognize the overall volcanic sequence and to outline sampling targets.

Sampling aimed to obtain a representative set of samples of both the hanging and footwall volcanic rocks: different volcanic- primary and secondary- textures/facies, hydrothermally altered samples and (apparently) fresh rocks.

Some samples collected from the open pit mine by Ana Jesus in May 2015 were also used in this work; they represent the northern most portion of the deposit, where the massive sulphide body was thicker.

Sample preparation

After collecting the samples, they were processed for the preparation of polished thin sections and whole-rock geochemistry, using the SQU and FCUL facilities, from May to September 2016.

Petrography and mineral chemistry:

The preparation of thin sections consisted in the following procedure: (1) identification of textural and mineralogical features of interest; (2) manufacturing of rectangular slabs, using small diamond saws; (3) gluing the rock slabs into un-polished glasse slices, using a two-part resin epoxy resin with high refractive index and mechanic resistance; (4) cutting the obtained chips to 0.5 mm thickness, using a precision diamond saw; (5) grinding the glued chips, until they reach a 40-45 μm thickness, with an automatic lapping equipment; (6) polishing the rock surfaces with ever finer diamond-pastes, until a uniformly smooth plane is obtained and a thickness of 30 μm. For some samples, the presence of expansive clays/phyllosilicates created various technical problems during the thin section making process, posing additional difficulties during the polishing stage.

Whole-rock Geochemistry:

For the whole-rock geochemistry, a single procedure was used for all the selected samples: (1) cutting in thin slabs; (2) emery polishing, eliminating all possible contamination derived from the saw and weathering; (3) reduction of the slabs to chip size using a hammer, with the samples wrapped in white paper; (4) when necessary, another size reduction using a chromium hardened steel roll mill; (5) powdering, using an agate ring mill, when the samples weighted more than 100g or had enough volume to fill the space between the agate rings, or using two smaller agate ball mills, if the weight/volume of the sample was not enough to use the agate ring mill.

Petrography

The mineralogical and petrographic description of the thin sections was made from July until November 2016, in FCUL facilities.

This characterization was made using both reflected and transmitted light microscopy, identifying and characterizing the mineralogical and textural diversity of the volcanic sequence, with a special emphasis on the mineralogical transformations between primary and secondary phases related to oceanic metasomatism and hydrothermal activity, synchronous of sulphide deposition. This was documented by a set of microphotographs that illustrate the most important and representative mineralogical and textural features.

Based on this petrographic study, a set of representative samples were gathered, to be used for the subsequent mineral chemistry studies.

Analytical conditions

Electron Probe Micro-Analyser (EPMA)

The mineral chemistry data was obtained using a set of selected representative polished thin sections, which were covered by a 20nm thick carbon coating, in the Electronic Microprobe Lab at FCUL. The used equipment was a JEOL JXA 8200 Superprobe, equipped with four wavelength-dispersive spectrometers (WDS), six analysing crystals (LIF, LIFH, PET, PETH, TAP and LDED2) and secondary and back-scattered electron detectors as well as a coupled energy-dispersive spectrometer (EDS). This allowed the quantitative, semi-quantitative and qualitative chemical analyses of mineral phases. All the measurements were made with a 20 second acquisition time for the peaks, and 5 seconds for the background. The accelerating voltage was 15kV, with a current beam of 25nA and a beam spot diameter of 5μm. Natural mineral and metallic standards were used as standards. The detection limits for the different measured elements, as well as the used standards, can be found in Appendix II

The main objectives of data acquisition were i) resolution of pending questions about the petrographic study, more specifically the identification of mineral phases whose small size and/or occurrence mode prevented an unambiguous optical conclusion; (ii) identification of accessory mineral phases, impossible to determine properly, under the optical microscope; and (iii) characterization of variations in chemical composition exhibited by mineral phases, found in different textural arrangements and more importantly by various generations of the same phase, when polishing conditions were adequate.

Whole-rock geochemistry

Following sample preparation, major and trace were measured using two different methods: I) Wavelength dispersive X-ray fluorescence (WDXRF) for the major elements, at Aveiro University, and; 2) Inductively coupled plasma mass spectrometry (ICP-MS) for the measurement of trace elements, at CNRS, Tolouse.

WDXRF:

Whole-rock major elements were obtained by WDXRF, in Aveiro University facilities, on pressed-powder pellets, using an Axios Panalytical equipment.

ICP-MS:

Whole rock trace elements concentrations were acquired on a HR-ICP-MS ELEMENT XR at the Géosciences Environnement Toulouse laboratory (Observatoire Midi-Pyrénées), Université of Toulouse III, following the procedure described by Barrat *et al.* (2007). Sample preparation consisted of a HF-$HClO_4$ digestion procedure (Yokoyama *et al.,* 1999) combined with a Tm addition (Barrat *et al.,* 1996). The Tm addition allowed the calculation of the trace element compositions based on the Tm positive anomaly appearing in the samples REE pattern. Therefore, there is no correction for any elemental loss during the chemical procedure. Following digestion, samples were diluted and directly analysed to obtain concentrations all trace elements. BHVO-2 was used as external standard following the values proposed by Barrat *et al.* (2007). The yield was monitored and concentrations calculated using the Tm anomaly (Barrat *et al.,* 1996). MG-PMS and UBN geostandards were measured using the same procedure. Analytical blanks are systematically subtracted to BHVO2 and samples cps.

CHAPTER IV

CHARACTERIZATION OF THE VOLCANIC SEQUENCE: HYDROTHERMAL ALTERATION HALOES AND PETROGENETIC CONSIDERATIONS

IV.1. PETROGRAPHY: TEXTURAL AND MINERALOGICAL CHARACTERIZATION

In this section, the microscopic textural and mineralogical features are described, using the macroscopic and microscopic observations and a set of illustrative microphotographs, supplemented by EPMA data.

The volcanic rocks that host the Mandoos MS deposit comprise a set of basaltic rocks that display numerous evidence of regional metasomatic and ore-forming hydrothermal (*s.s.*) alteration. The textural arrangements of secondary mineral assemblages document the progression of fluid-rock interactions, at different evolving stages, causing heterogeneous alteration patterns.

Hanging Wall

The hanging wall rocks comprise a set of coherent facies: massive flows and/or massive flows, with minor apparent-volcaniclastic/autoclastic facies (see McPhie, 1993), along with basaltic rocks that display evidence of different stages of alteration.

Macroscopically, these rocks are classified as fine-grained vesicular microporphyritic basaltic rocks, distinguishable by their colours - resulting from differences in mineralogy, due to alteration (*s.l.*) phenomena - as well as by the presence of vesicle and their infillings and by the relative size and distribution of veinlets.

Overall, primary textures and, to some extent, primary mineralogy, are well preserved. Clinopyroxene, minor plagioclase microphenocrysts are set within a fine-grained, microcrystalline plagioclase microlitic-lath matrix, partly replaced by secondary mineral assemblages, with abundant primary iron-titanium oxides.

The microphenocrysts generally occur as clusters or single crystals of euhedral to sub-euhedral clinopyroxene and minor plagioclase. The clinopyroxene crystals, ~600 μm to ~1mm in size, do not show zoning and are partly to completely replaced by secondary mineral phases, showing evidence for a complex and polyphasic replacement. At first, the clinopyroxene is altered to an amphibole (actinolite?), which is subsequently altered to chlorite and epidote. Plagioclase phenocrysts are mostly euhedral, ranging from ~0.5 to ~1mm, and are almost completely replaced by albite; early/primary plagioclase composition is preserved in patches, and the grains are set in a brownish-greenish phyllosilicate-rich groundmass.

Swallow-tailed plagioclase microlites are also found within the phyllosilicate-rich matrix; these plagioclase microlites and matrix alteration are marked by (I) increase of the albitic component in the microlites (as documented by EPMA, see Chapter IV.2); (II) pervasive phyllosilicate, and minor epidote, alteration, affecting the matrix and early Fe-Mg silicate phases. Iron and titanium primary oxides –

titanium-rich magnetite -are found disseminated within the matrix, between the plagioclase microlites, showing corroded outer rims, intergrown with secondary small titanite crystals.

The abundance of vesicles, size and distribution within the volcanic rocks varies and represents the channels generated by volatile escape. These vesicles are filled with secondary mineral phases, precipitated during alteration processes. Usually they are rimmed by fine-grained phyllosilicates and filled with radial aggregates of the same phyllosilicates, quartz, zeolites and/or carbonates.

Volcanic glass was found in two samples, in contact with a basaltic rock; this glass-basaltic rock interface corresponds, probably, to a contact between two different lava flows, where the rapid cooling of the base of the latter inhibited crystallization and, consequently, fostered the formation of volcanic glass. This volcanic glass shows devitrification textures -– spherulites – and aligned vesicles, mostly filled with phyllosilicates. The latter are also found replacing the volcanic glass, suggesting that the brownish groundmass observed in other volcanic rocks matrix is a result of volcanic glass alteration. Partly altered clinopyroxene and plagioclase microphenocrysts are also found within the volcanic glass, as well as hematite sealing microfractures.

Monomict autoclastic breccia rocks occur within the hanging wall volcanic sequence. These consist of basalt pseudo-clasts surrounded by a micro to cryptocrystalline pseudo-matrix, composed of chlorite, quartz and minor carbonates. Although the primary igneous texture is still recognizable, the basalt pseudo-clasts show evidence of strong alteration: intense albitic replacement, in plagioclase, and strong phyllosilicates deposition, although preserving relics where the early breakdown of pyroxene into amphibole, preceding the formation of *Chl+Ep*, can still be seen. The intensity of this alteration increases towards the pseudo-matrix, blurring the contact between both; in other cases, the (-pseudo-)clast/matrix contact is outlined by late chlorite aggregates or by microfractures filled with carbonates. This reflects the distribution of fractures, generated by *in-situ* fragmentation, allowing an increase in the permeability and, consequently, an increase in fluid circulation. Thus, these samples might represent the top of massive flows/pillow lavas, where quenching favoured fragmentation and fluid circulation.

The hanging wall volcanic sequence is crosscut by a series of late veinlets, with different mineral infills: (I) early (calcic) zeolites, with calcite intergrowths; (II) abundant calcite, with minor zeolites, whose deposition is correlative with brecciation episodes, possibly synchronous of the late events of vesicle infilling; and (III) minor late, fine-grained, chlorite and quartz or carbonate.

During the final stages of carbonate precipitation, hematite occurs, sometimes, developing intergrowths with calcite and chlorite. Otherwise, hematite precipitation is controlled by structural discontinuities (fractures and veins/veinlets) and sometimes its deposition occurs together with microcrystalline silica/quartz. Hematite also occurs widely disseminated in the basaltic rocks, transposing the primary texture. In these situations, the volcanic primary texture is only recognizable by the occasional presence of primary clinopyroxene and minor plagioclase microphenocrysts. This pervasive hematitic alteration is also associated with the deposition of jaspers and umbers, which can be later crisscrossed by anastomosed carbonate and minor chlorite veins, with associated brecciation.

It is important to highlight the absence of sulphides in the hanging-wall sequence, whether disseminated within the matrix, vesicles or even in later mineral infills along distinct sets of structural discontinuities veins/sealing, indicating the absence of mineralizing hydrothermal (*s.s.*) processes.

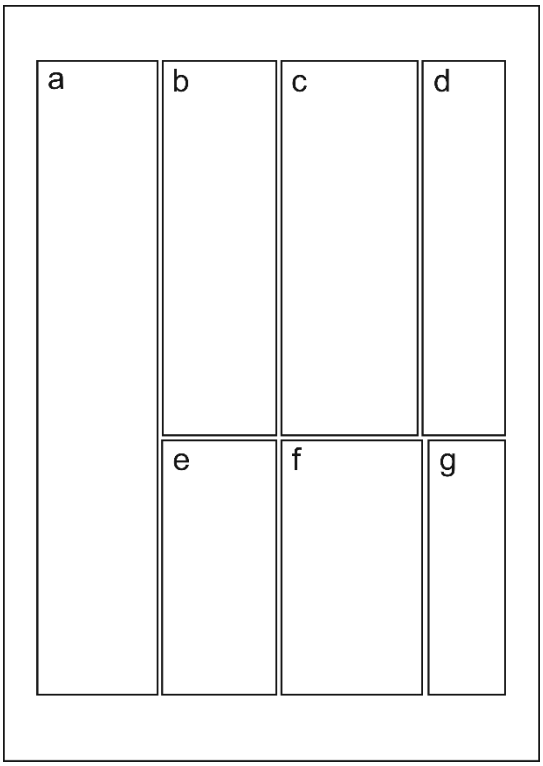

Figure IV.1- Main features of hanging-wall hand samples: **(a)** greenish/bluish grey fine-grained basaltic rock, showing phyllosilicate-rich alteration in the matrix, carbonate-filled vesicles and carbonate + hematite-sealed veins/veinlets; **(b)** and **(e)** both samples consist of a chlorite altered, fine-grained basaltic rock with carbonate-filled vesicles, crosscut by greyish veins (chlorite+quartz?) and by later chlorite+carbonate ± hematite veins; **(c)** hematite-impregnated fine-grained basalt, cut by hematite sealed veins; this basalt contacts with a umber, which shows more intense carbonate-cemented veins and local brecciation textures; **(d)** chlorite-altered? fine-grained basalt with carbonate-filled vesicles and crosscut by late chlorite ± carbonate veins; at the bottom a contact with volcanic glass is found, with sparse carbonate-filled vesicles, later cut by hematite-bearing veins; **(f)** Monomict pseudo-breccia, revealing isolated basaltic pseudo-clasts, with chloritic? alteration, surrounded by a microcrystalline chlorite, quartz? and carbonates pseudo-matrix; **(g)** chlorite altered greenish grey, fine-grained basalt with greyish (quartz and chlorite?) veinlets, cut by later hematite bearing veins/veinlets.

White bars are 2cm long.

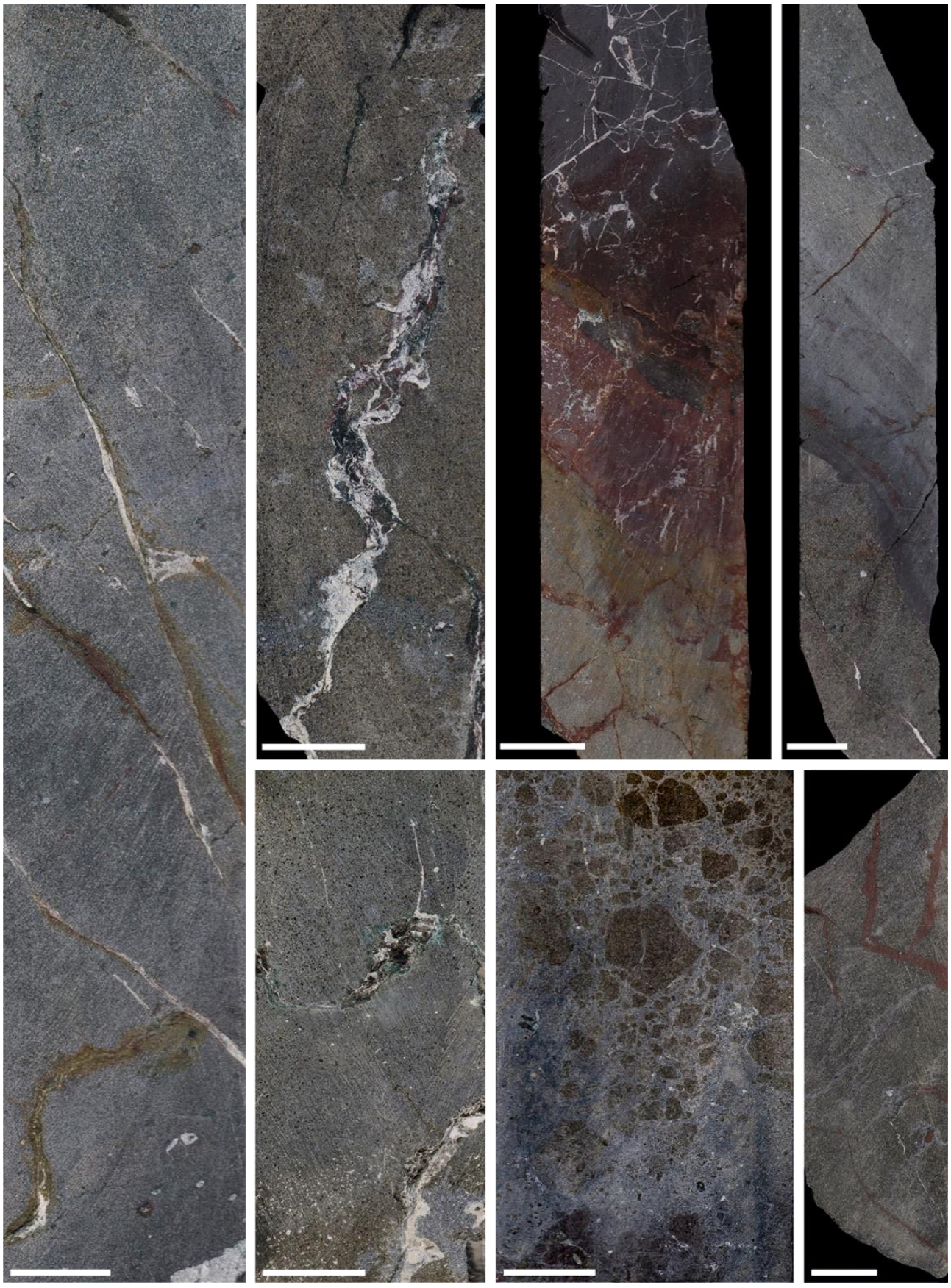

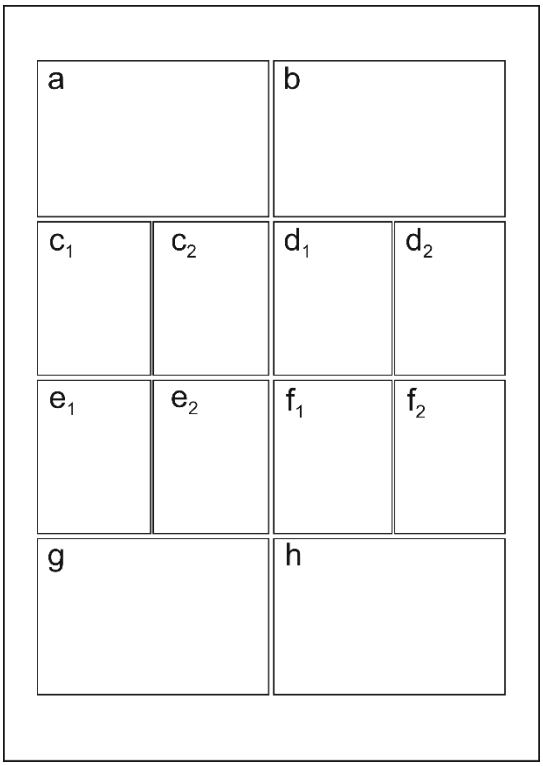

Figure IV.2- Hanging-wall petrographic features: **(a)** and **(b)** euhedral plagioclase microphenocrysts, almost completely replaced by albite, within a dark, fine grained groundmass with plagioclase microlites; disseminated primary oxides, in the *Chl-Sme*-rich groundmass, are altered to titanite, and cut by later carbonate veinlets. [TL; PP (a) & XP (b); 5x]; **(c_1), (c_2), (d_1)** and **(d_2)** euhedral clinopyroxene crystals, showing partial to near complete replacement by an amphibole and chlorite (±epidote) assemblage, within a phyllosilicate-rich groundmass with plagioclase microlites and primary Fe-Ti oxides altered to titanite. [TL; PP (c_1) & (d_1) & XP (c_2) & (d_2); 5x]; **(e_1)** and **(f_1)** vesicle filled with radial chlorite-smectite aggregates [TL, PN & XN; 5x]; **(e_2)** and **(f_2)** chlorite rimmed, carbonate filled vesicle. [TL; PP (e_2) & XP (f_2); 5x]; **(g)** and **(h)** basaltic pseudo-clasts, with phyllosilicate-rrich groundmass, plagioclase microlites and primary iron-titanium oxides, altered to titanite, locally outlined by fine-grained chlorite set in a microcrystalline pseudo-matrix of quartz, chlorite and carbonates. [TL; PP (g) & XP (h); 5x].

White bars are 400µm long.

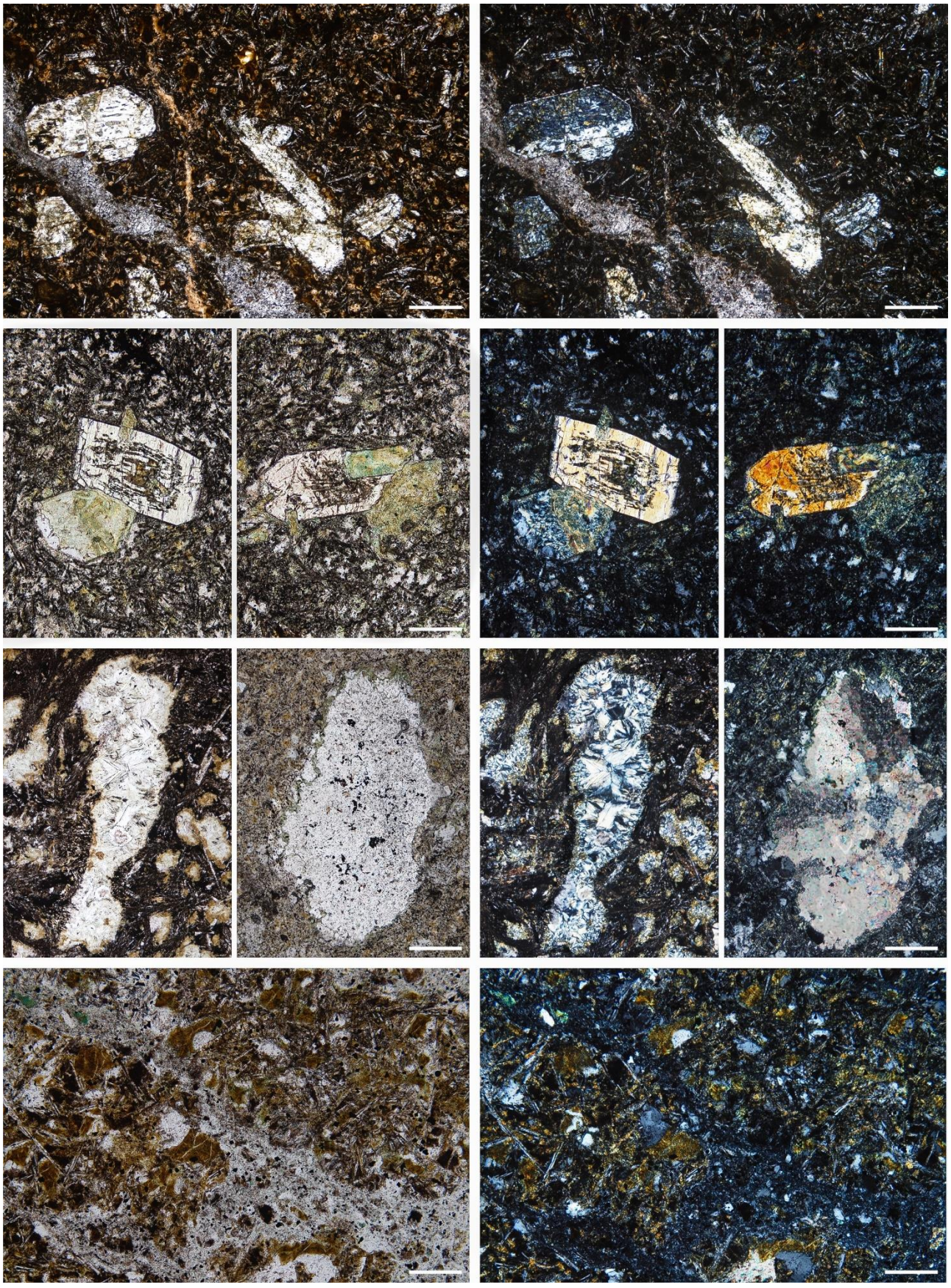

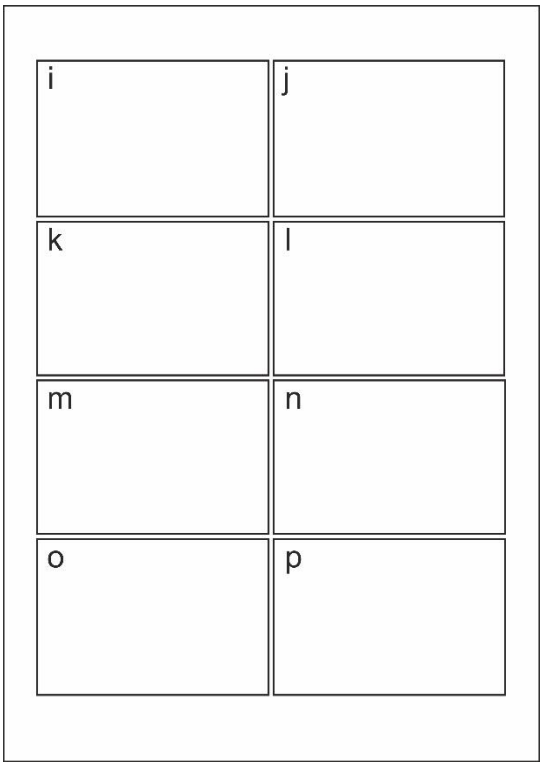

Figure IV.2- Hanging-wall petrographic features: **(i)** and **(j)** euhedral plagioclase and clinopyroxene microphenocrysts partly to completely replaced by albite and amphibole, respectively, within a very dark to nearly opaque matrix, due to strong hematite dissemination; carbonate+chlorite filled vesicles, are cut by late carbonate veinlets, locally displaying brecciation textures. [TL; PP (a) & XP (b); 5x]; **(k)** and **(l)** late vein composed of carbonate, chlorite and hematite, cutting the fine-grained plagioclase microlitic rich matrix of the basaltic rock [TL; PP (c) & XP (d); 5x]; **(m)** and **(n)** vesicle cut by carbonate-hematite intergrowths and minor chlorite. [TL, PN (d) & XN (e); 5x]; **(o)** and **(p)** brecciation texture, wherein carbonate veins display *en echelon* arrangement. [TL; PP (g) & XP (h); 5x]

White bars are 400µm long.

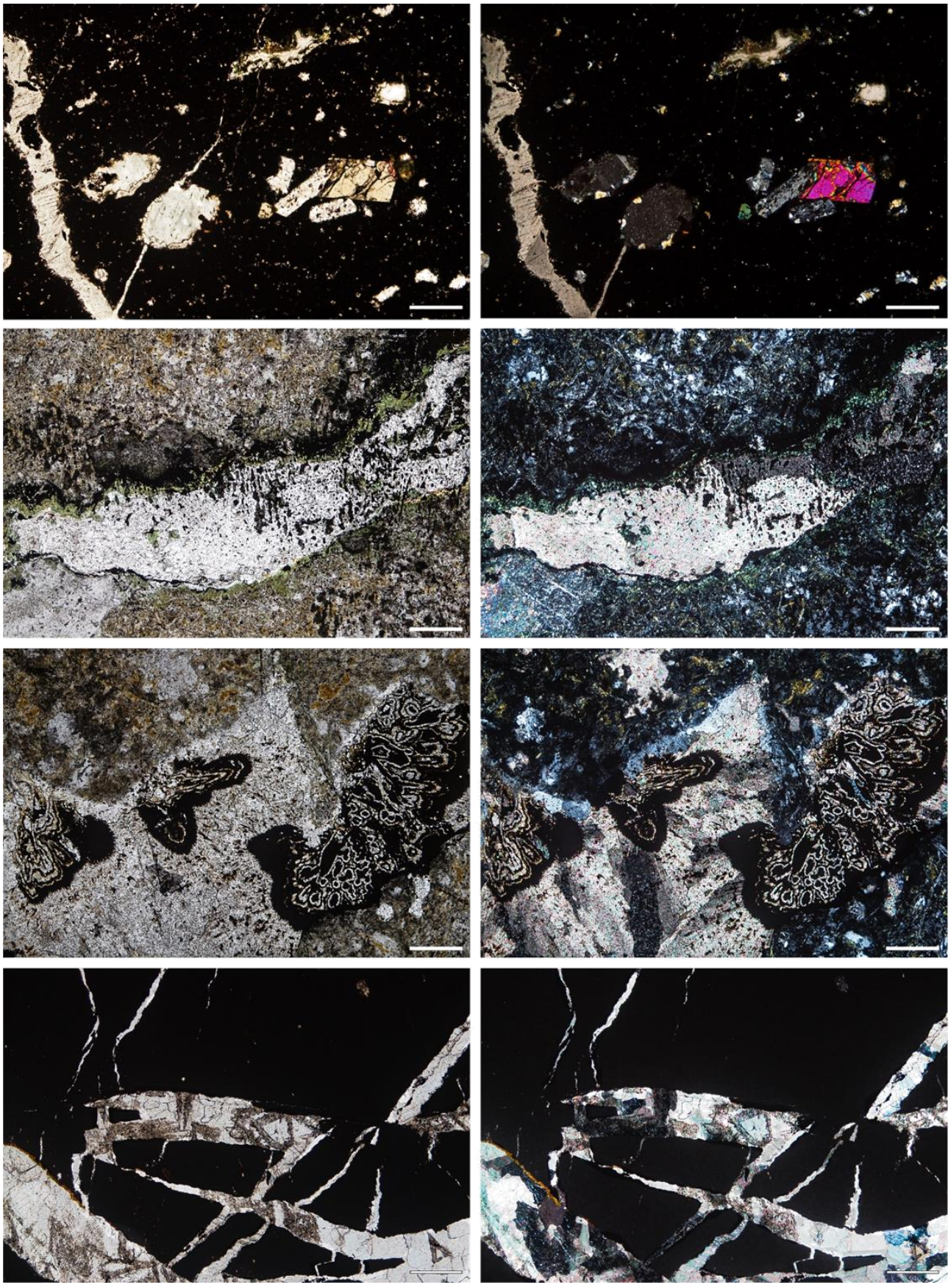

Footwall

The footwall volcanic sequence is mostly composed of basaltic rocks, with primary textures almost completely obliterated, documenting an intense and possibly long-lasting alteration process. The only remnants of the primary mineral assemblage are feldspar microlithic laths.

Plagioclase microlites show skeletal remains of the primary feldspar crystals, with Na-rich cores and, sometimes, intense quartz neo formation, overgrowing the original microlites and/or replacing them. Fine-grained chlorite aggregates, with bluish-anomalous interference colours, outline probable remnants of ferromagnesian phases (clinopyroxene). This is accompanied by the precipitation of fine-grained chlorite and euhedral pyrite crystals, in the rocks matrix; the same paragenesis is found filling vesicles. Nevertheless, this mineral association represents the less intense hydrothermal alteration association (*Chl+Py+Qz*) and characterizes the hydrothermal alteration observed in the footwall volcanic rocks sampled in the drill-cores. The hydrothermal alteration process is more intense when volcanic rocks are more vesicular, due to enhanced fluid circulation, induced by earlier high permeability. Thus, volcanic rocks record variable intensity of silicification and chloritization processes, with Na-rich plagioclase microlites recording also the effects of the early-developed regional alteration stage, as described before (see hanging-wall). The silicifiation ± pyritization processes are more pervasive and intense in the basaltic rocks recovered from the open pit, where, in extreme cases of hydrothermal alteration, samples are partly to completely replaced by *Qz+Py±Ccp±Sph*, with greenish, *i.e.* chloritzed, remnants of the basaltic rock and feldspar microlites. These samples are also characterized by an intense brecciation and infill by the same mineral association found in the rocks matrix.

The hematitic alteration described for the hanging-wall volcanic sequence is also present in the footwall volcanic sequence. Hematite-impregnated basalts/jaspers/umbers are present in the southern/southwestern sampled portion of the deposit, affected by the same hydrothermal processes as the basaltic rocks, whereas hematite (±quartz)-bearing veinlets/veins are found throughout the rest of the sampled volcanic rocks. Additionally, some hematite veins cut the hydrothermally altered rocks, especially noticeable in the open pit samples.

In the hematite-altered basaltic rocks, and in jaspers, formed prior to the development of the hydrothermal system and mineralization, evidence for bleaching processes is seen, adjoining quartz veins where the reddish hematite coloration becomes weaker or disappears, accompanied by dissemination of small pyrite crystals. Such relationship indicates iron bleaching/leaching and reduction, followed by minor sulphide precipitation.

Four phases of formation of hydrothermal quartz veins can be identified, some of them evidencing brecciation that crosscuts the footwall volcanic sequence, as well as re-opening evidences, suggesting a tectonic control on the circulation of silica-rich (saturated) hydrothermal fluids. Sometimes, these quartz crystals present a mild wavy extinction, revealing sub-granulation, consequence of intra-crystalline plastic deformation. Occasionally, these hydrothermal veins are found overlapping, evidencing that these veins are reactivated/re-opened and, thus, denouncing a structural control on the fluid circulation.

The first phase comprises comb-like quartz crystals, and, in the late-stages, chalcopyrite. These are cut by a second generation of veins, finer grained, granular quartz crystals, pyrite and chalcopyrite; the latter also precipitates in microfractures, outlining first-stage pyrite crystals.

The third and fourth late quartz generations comprise microcrystalline quartz veinlets/veins, where microcrystalline quartz occurs, sometimes as bands, suggesting that deposition was triggered by rapid cooling; these bands are subsequently disrupted by an almost orthogonal set of quartz infilled

microfractures, also with no sulphides associated. These quartz bands sometimes have the same orientation as previously formed veins, which might indicate re-opening of the structures.

Late carbonate veins, with minor pyrite, cut the earlier quartz veins, some of which are reopened and sealed by *Cb+Py*.

The various hydrothermal stages are conspicuous in the more intensely hydrothermally altered rocks (open pit samples), and in the hematite impregnated and jasper samples (S/SE drill-core samples), with silicification and dissemination of *Py*, sometimes together with Al-rich phyllosilicates. Thus, it is possible to establish a relative chronological relationship for the different hydrothermal stages. In some cases, this hydrothermal alteration is epitomized by fine-grained chlorite and/or quartz veins, with sulphides, pyrite with minor chalcopyrite, bearing veins and by disseminated, sub-microscopical, euhedral to subhedral apatite crystals. This is possibly related to a structural control of the alteration processes, suggesting that these mineral assemblages and textural arrangements can be used as proxies to the ore-forming system. In some cases, there is an overlap between more than one hydrothermal phase, similar to what is observed in the hematite impregnated basalts/jaspers, with the microcrystalline quartz bands corroding granular quartz and sulphide veins.

In samples of the footwall volcanic sequence, fom the open pit, zeolites occur, with quartz, in veins and as vesicle infills. Such veins clearly cut the volcanic rocks after its weak to moderate hydrothermal alteration (*Py+Qz*) and they show evidence of reactivation, with hydrothermal microcrystalline quartz crystals.

Doleritic rocks, with well-developed intersertal texture, occur also in the footwall sequence. These rocks display a primary mineralogy similar to the one found in the hanging-wall rocks, larger (in comparison to the hanging-wall volcanic rocks) primary iron-titanium oxides grains, and sparse clinopyroxene and feldspar microphenocrysts; phyllosilicate-filled vesicles occur sparsely. These doleritic rocks show a pervasive alteration similar to the one described above, with the breakdown of primary Fe-Mg phases and intense phyllosilicate alteration, demonstrating that these rocks underwent a similar fluid-assisted alteration process analogous to the one described for the hanging-wall volcanic sequence. Nevertheless, some sub-microscopical *Py* crystals are present, as well as apatite. The presence of such mineral phases will be later discussed (see Chapter V).

Based on the mineralogical and textural relationships previously described, a paragenetic sequence is depicted in Figure IV.8 (see end of section). This is divided into three main alteration stages, the first (Alteration stage I) comprising the breakdown of primary igneous phases and vesicle and vein infills, evident on the hanging-wall sequence. The second alteration stage (Alteration stage II), found in both hanging and footwall rocks consists in a low-temperature hydrothermal alteration, including the formation of jaspers and/or umbers, and, occasionally coupled with pervasive hematite dissemination, transposing the primary igneous textures. Hydrothermal alteration, related to sulphide deposition follows (Alteration stage III), found only in the footwall volcanic rocks, with the development of quartz-sealed veins, distinguishing different stages, some of them with associated sulphides and, occasionally, apatite.

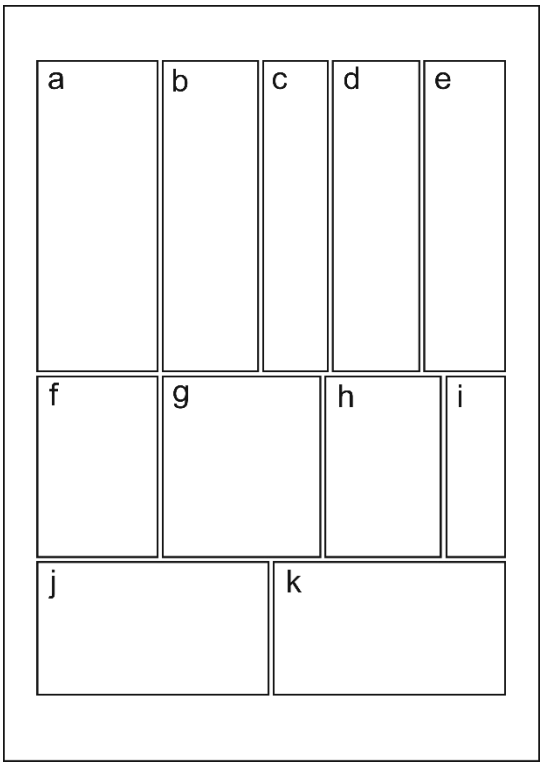

Figure IV.3- Footwall hand samples-features: **(a)** fine-grained basaltic rock, showing intense chloritic alteration in the matrix, with sparse carbonate-chlorite-infilled vesicles and hematite veinlets; **(b)** chlorite-altered, fine-grained basaltic rock with disseminated sulphides and chlorite-filled vesicles, cut by quartz and chlorite veins, with pyrite; **(c)** chlorite altered, fine-grained basaltic rock with disseminated sulphides and chlorite-filled vesicles, cut by hematite veins and later by quartz, chlorite and sulphide veins; **(d)** silicified basalt, with disseminated sulphides within the matrix and quartz+pyrite-filled vesicles, cut by quartz and sulphides pyrite veins; **(e)** Jasper sample, cut by I) quartz and pyrite and II) quartz, pyrite, chalcopyrite veins; **(f)** Jasper(/hematized basalt?/umber?) cut by a set of quartz and sulphides pyrite veins, showing evidence of bleaching, in the vicinity of the veins- loss of reddish coloration and precipitation of small pyrite crystals- with some disseminated sulphides, as well as vesicles infills; **(g)** basaltic rock with chloritized matrix, showing pyrite dissemination, with quartz and chlorite-filled vesciles, later cut by hematite veinlets; **(h)** silicified basalt, cut by quartz and hematite veins and, subsequently cut by a set of quartz+pyrite and quartz+chalcopyrite veins/veinlets; **(i)** doleritic rock that cuts through the footwall sequence, with a coarser-grained and carbonate and phyllosilicate filled vesicles; **(j)** silicified basalt, with zeolite-filled vesicles, cut by quartz vein(s); **(k)** silicified basalt with quartz-filled vesicles and zeolites and quartz filled veins.

White bars are 2 cm’s long.

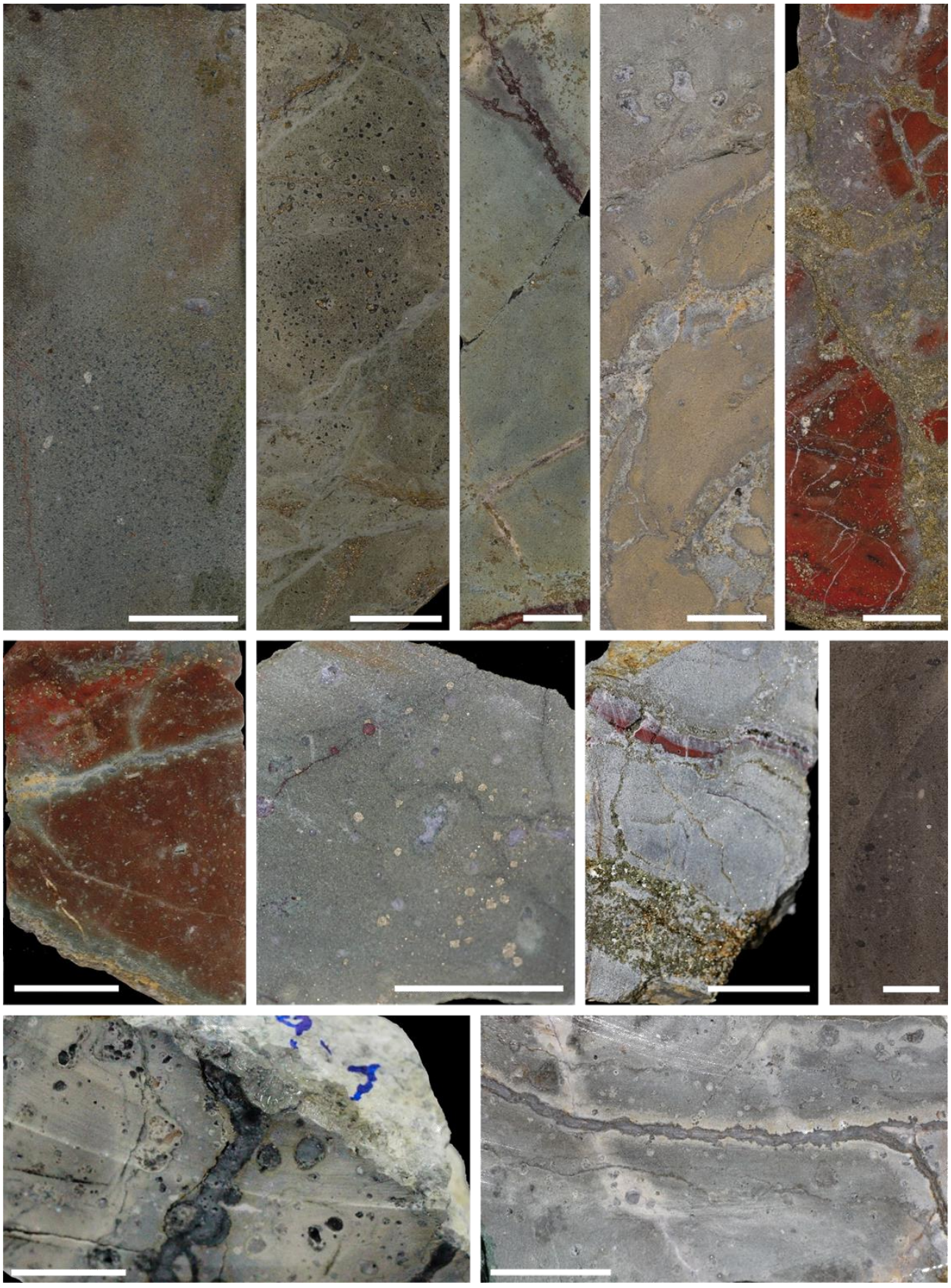

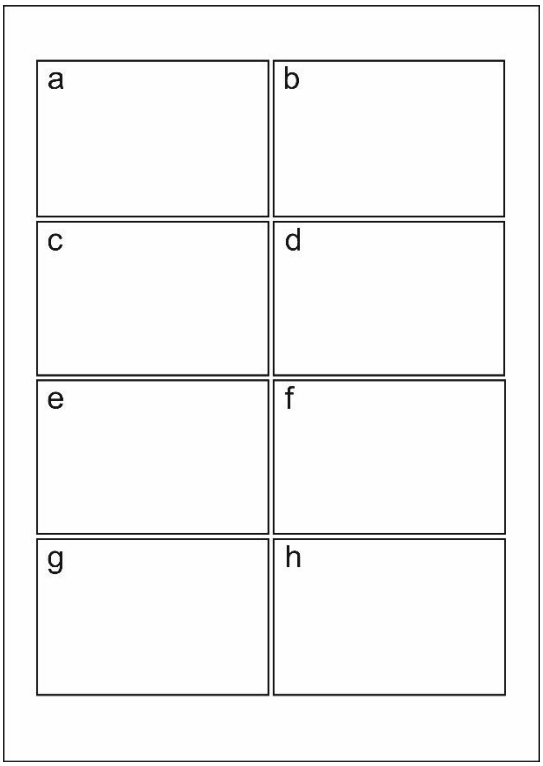

~

Figure IV.4- Footwall microscopic features: **(a)** and **(b)** weakly silicified basalt, with preservation of plagioclase microlites, displaying disseminated sulphides, cut by hematite veins, later crosscut by a granular quartz with minor pyrite [TL; PP (a) & XP (b); 5x]; **(c)** and **(d)** weakly silicified and chloritized basalt, with remnants of microlitic matrix and quartz+chlorite filled-vesicles, disseminated pyrite, cut by veins composed of microcrystalline quartz and euhedral chlorite, pyrite crystals and chalcopyrite [TL; PP (c) & XP (d); 5x]; **(e)** and **(f)** jasper sample with evidence of bleaching- loss of its reddish colour at the edge of the contact with quartz + pyrite vein [RL, PN (d) & XN (e); 5x]; **(g)** and **(h)** comb-like growth of quartz crystals and synchronous pyrite precipitation [RL; PP (g) & XP (h); 5x]

White bars are 400μm's long.

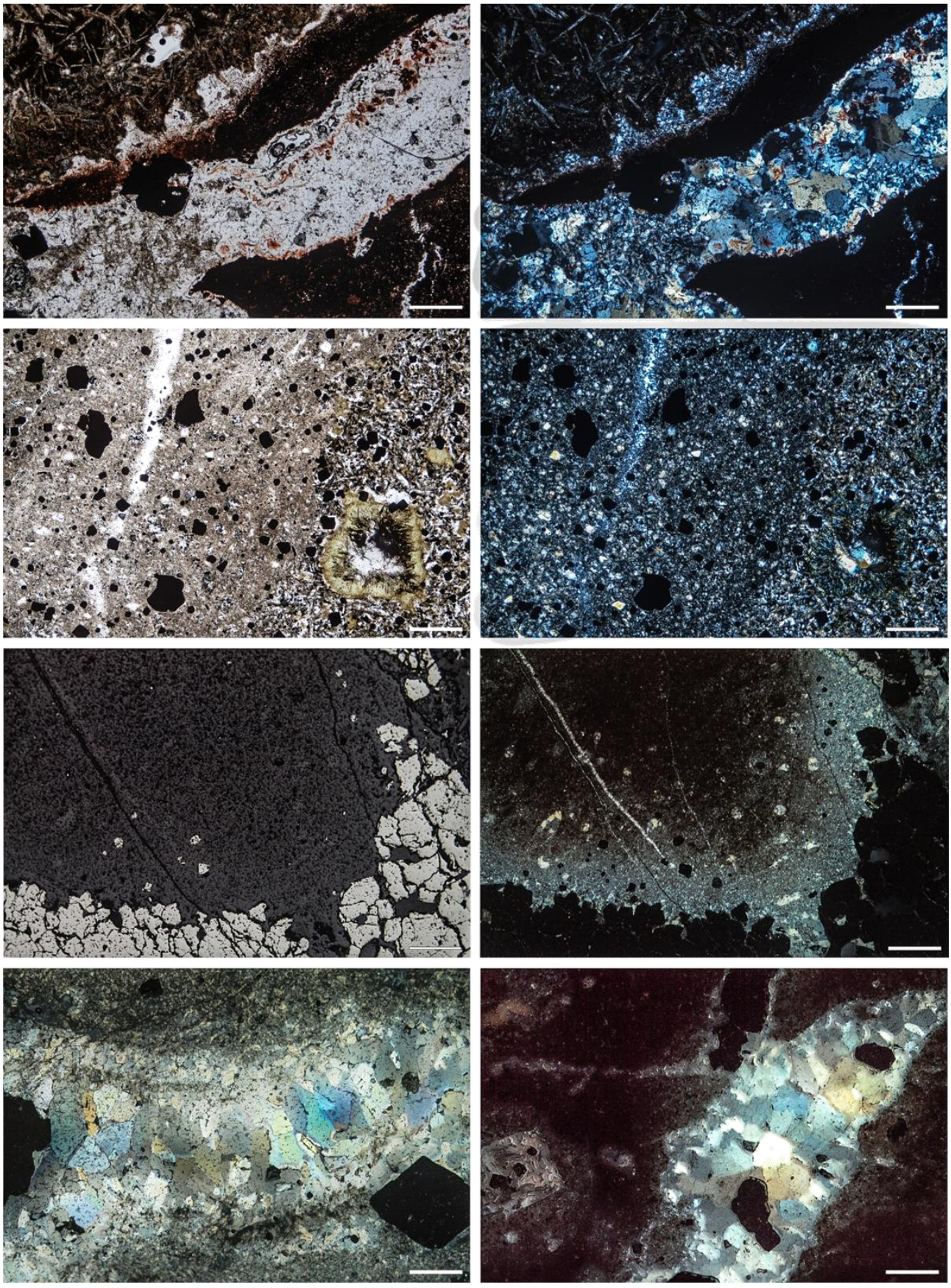

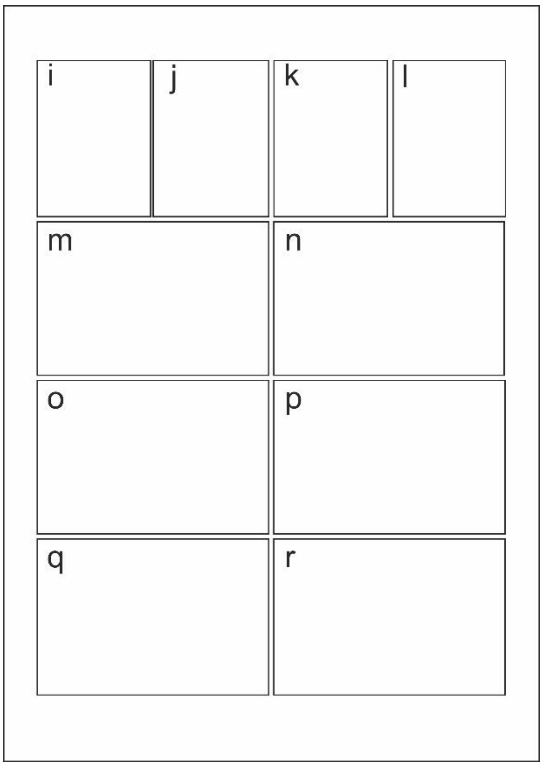

Figure IV.4- Footwall microscopic features: **(i), (j), (k)** and **(l)** examples of chalcopyrite precipitation contemporaneously and following pyrite deposition: [(b)&(d)] and chalcopyrite precipitation within microfractures that cut through pyrite and quartz-sealed veins [(b)&(d)] [TL; PP (a), (c) & XP (b), (d); 5x]; **(m)** and **(n)** hematite dissemination within jasper? with quartz-filled vesicles and later cut by comb-like quartz crystals growth veins, with pyrite, some of which later re-opened and were sealed by carbonate and pyrite. [TL; PP (e) & XP (f); 5x]; **(o)** and **(p)** slightly to moderately silicified basaltic rock, with plagioclase microlitic matrix relics and disseminated pyrite, with quartz-filled vesicles, cut by a quartz and calcic zeolite vein showing corroded rims, when in contact with a later microcrystalline quartz band [RL, PP (g) & XP (h); 5x]; **(q)** and **(r)** weakly to moderately silicified basaltic rock, with remnants of the plagioclase microlites with zeolite, with minor carbonate, phyllosilicates and quartz, filled vesicles [RL; PP (i) & XP (j); 5x].

White bars are 400μm's long.

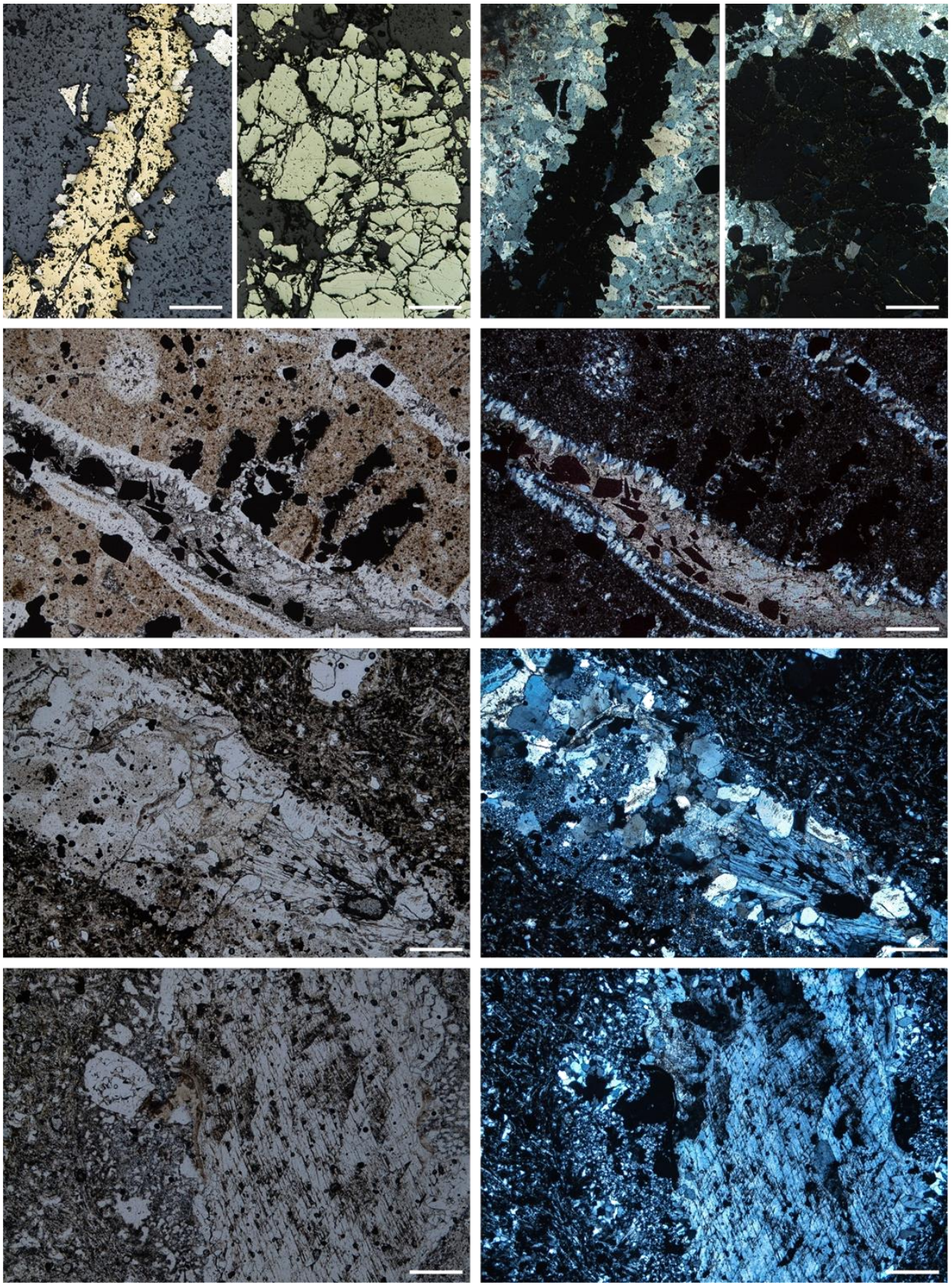

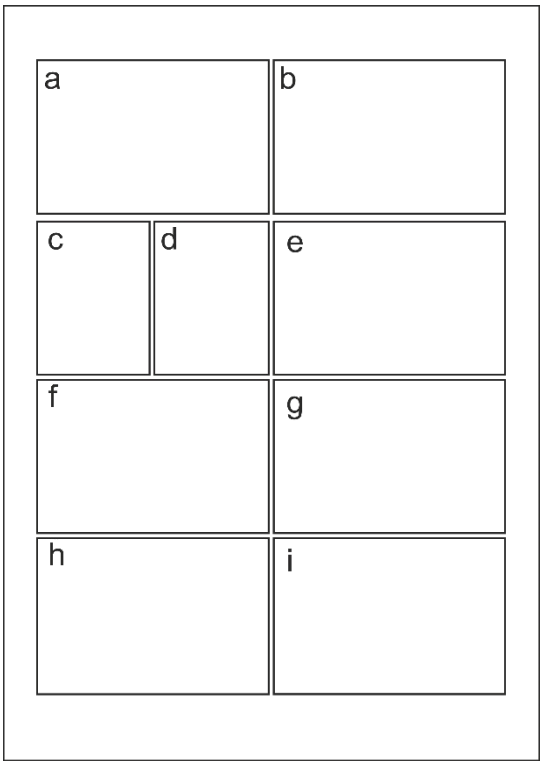

Figure IV.5- Back-scattered electron (BSE) photomicrographs of several features of Hanging-wall rocks: **(a)** Feldspar microphenocrysts, replaced by albite (dark grey), with patches of bytownitic composition (lighter grey); **(b)** Zeolite crystals (darker) showing one cleavage direction, with calcite (lighter grey). Back-scattered electron (BSE) photomicrographs of several features of Footwall rocks: **(c), (d), (e)** examples of apatite crystals, precipitated during hydrothermal alteration, near vesicles filled with fine-grained phyllosilicates, in a quartz and pyrite-rich matrix; **(f)** chalcopyrite (ligher grey) and pyrite crystals (darker grey), in a quartz and chlorite vein; **(g)** chalcopyrite filling cracks between first-stage euhedral pyrite, in quartz vein; **(h)** phyllosilicate accompanying quartz and pyrite; **(i)** and **(j)** iron and titanium oxides with corroded cores, in dolerite phyllosilicate rich matrix.

White bars are 100 μm long in all figures, except in (h), where it is 0.5mm.

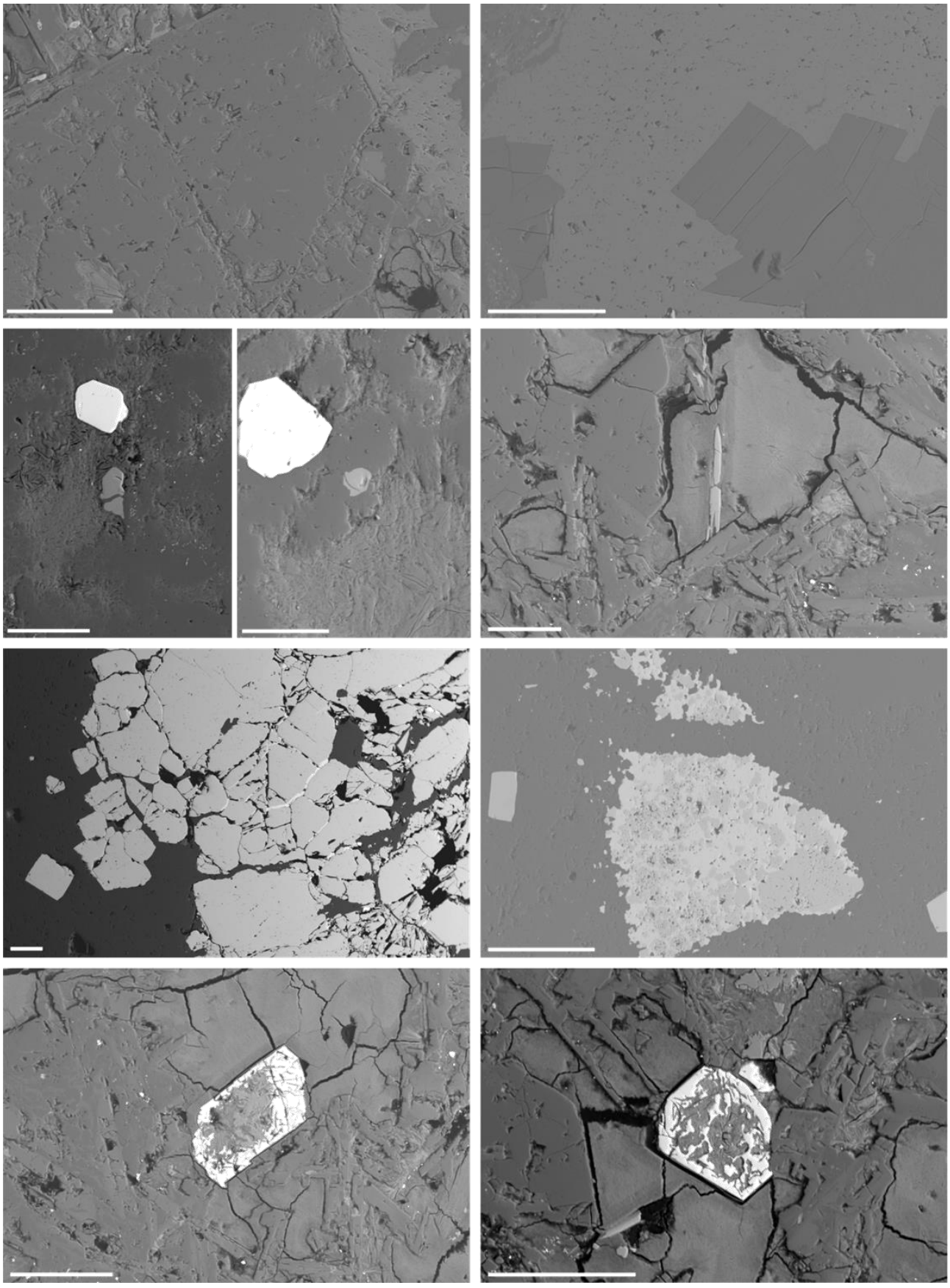

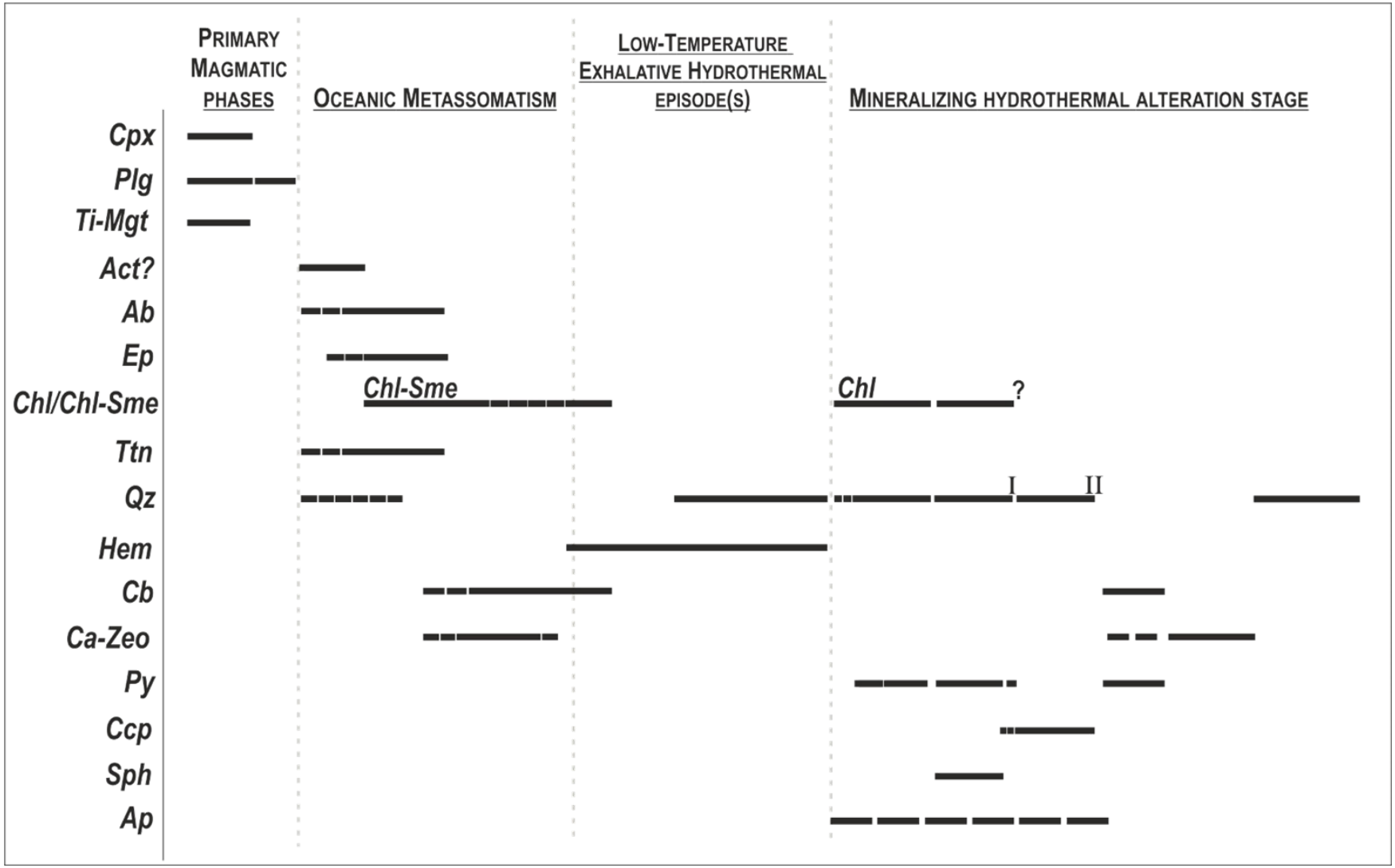

Figure IV.6- Paragenetic sequence, distinguishing three main alteration stages, based on the petrographic description and interpretation.

IV.2. MINERAL CHEMISTRY

This section reports the chemical compositions of the mineral phases, found on the volcanic rocks that host the Mandoos massive sulphide. For this, 8 representative thin sections were chosen representing the different textural arrangements. This analysis focused on silicates- namely primary phases such as feldspars (*s.l.*) and pyroxenes, or secondary, such as chlorite group minerals, oxides, carbonates, sulphides (pyrite, chalcopyrite, sphalerite) and phosphates- apatite. Some of the identified mineral phases were not analysed due to their small dimensions or because the polishing was not ideal, the obtained results indicating the effects of contamination from the adjacent mineral grain; that was often the case of titanite, hematite or magnetite. The data management and processing was based on the previous petrographic characterization and it consisted on the confirmation of the mineral phases, ensuring that the EPMA analysis were valid and consistent with the mineral stoichiometry. The results of this detailed mineralogical characterization will contribute to constrain geochemistry-based models for the geological evolution these volcanic rocks and related ore forming processes.

IV.2.1. SILICATES

Silicates form most primary and secondary mineral phases in volcanic rocks, both in the hanging and footwall rocks. They include pyroxene, feldspar, chlorite minerals, zeolite group minerals, with some unidentified phyllosilicates.

IV.2.1.a. PYROXENES

In order to characterize the compositional variability of the pyroxene microphenocrysts found in the hanging-wall volcanic rocks, 71 analyses were performed, in three polished sections (see Appendix IV). Their study followed the recommendations of the pyroxenes CNMMN-IMA subcommittee (Miromoto *et al.*, 1988).

The general group formula is given as $M2(R^{2+})M1(R^{2+})T_2(2R^{4+})O_6$, in which T represents the tetrahedral position, occupied by Si and Al, and M1 and M2 the octahedral coordination positions, where divalent (R^{2+}) cations are present (Morimoto *et al.*,1988).

The discriminating J-Q diagram (Morimoto *et al.*, 1988) (Figure IV.7), show that all the analysed pyroxenes fall into the "quadrilateral" chemical group field, i.e. they have Ca, Mg and Fe as major components, displaying also a strong compositional homogeneity. Following the recommendations proposed by Moritomo et al., (1988), the use of the $Mg_2Si_2O_6$ (enstatite) – $Fe_2^{2+}Si_2O_6$ (ferrosilite) – $CaMgSi_2O_6$ (diopside) – $CaFe^{2+}Si_2O_6$ (hedenbergite) quadrilateral system allows a chemical classification and the evaluation of the variation in the chemical compositions, where the solid solution end-members for Ca-Mg-Fe quadrilateral pyroxenes are expressed in % of enstatite (*En*%=100Mg/(Ca+Mg+ΣFe), wollastonite (*Wo*%= 100Ca/Ca+Mg+ ΣFe) and ferrosilite (*Fs*%= 100 ΣFe/Ca+ Mg+ΣFe), where ΣFe = Fe^{2+}+Fe^3, including also Mn.

The available data fall within the augitic clinopyroxene compositional field, with an average chemical formula $En_{39\text{-}54}Wo_{27\text{-}43}Fs_{8\text{-}23.}$ These pyroxenes are also characterized by low Al and Ti contents (1.22-4.02; 0.07-0.41 *wt*%, respectively), typical of tholeiitic rocks (BVSP[1], 1981). Additionally, Cr contents are also low (0.06-1.11 wt%).

[1] BVSP- Basalt Volcanism Study Project

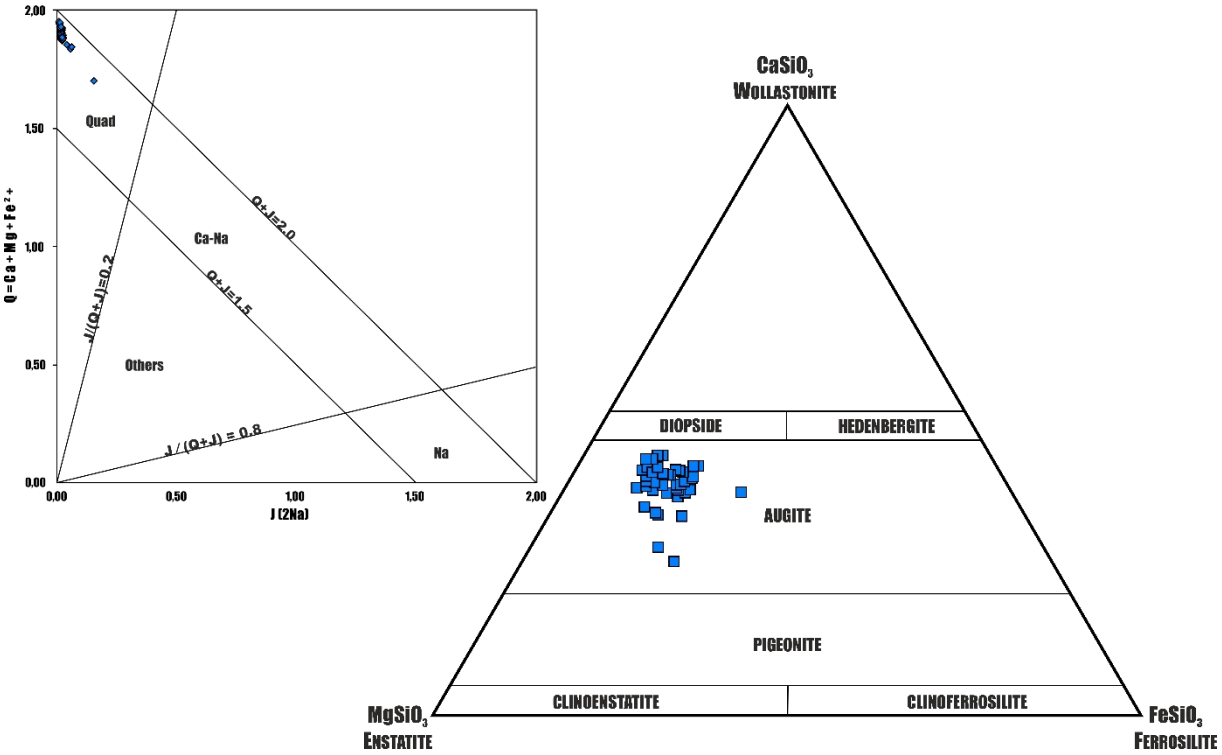

Figure IV.7- Pyroxene classification diagrams: Q-J discriminating diagram and the Compositional diagram for quadrilateral pyroxenes, following the recommendations of the pyroxenes CNMMN-IMA subcommittee (Morimoto *et al*., 1988).

IV.2.1.b. FELDSPARS

Feldspar (s.l.) crystals are the most common primary mineral phase, occurring as minor euhedral microphenocrysts and, most commonly, as microlites in the groundmass of volcanic rocks. Its chemical composition variation were examined on the basis of 125 analyses in 5 thin sections (see Appendix V).

The feldspar group are tectosilicates with general formula MT_4O_8, where T is occupied either by Si^{4+} or Al^{3+} cations; the M position is occupied by Ca^{2+}, Na^{+} and/or K+, allowing an incomplete solid solution between albite ($NaAlSi_3O_8$), anorthite ($CaAl_2Si_3O_8$) and K-feldspar ($KAlSi_3O_8$) (Deer et al., 2008). Thus, a compositional classification can be made, using the relative percentage of the three end-members (*An*%, *Ab*% or *Or*%; Figure IV.7).

The analysed feldspars belong to the plagioclase series, i.e. with less than 10% *Or*%, with two main compositional groups, spanning from Ca-rich terms to Na-rich phases: the first comprises the primary plagioclase compositions, falling within the bytownite and labradorite compositional field, reflecting a primary Ca-rich plagioclase. Primary plagioclases are still found in relic patches within microphenocrysts ($An_{70.1\text{-}84.9}$) and microlites ($An_{61.3\text{-}71.1}$). The second compositional group is characterized by plagioclase with a higher albitic component ($Ab_{84.7\text{-}99.5}$). This represents the altered portion of the feldspar phenocrysts and microlites, in which there is a sodium incorporation, leaving cores of Ca-rich primary plagioclase (Figure IV.8).

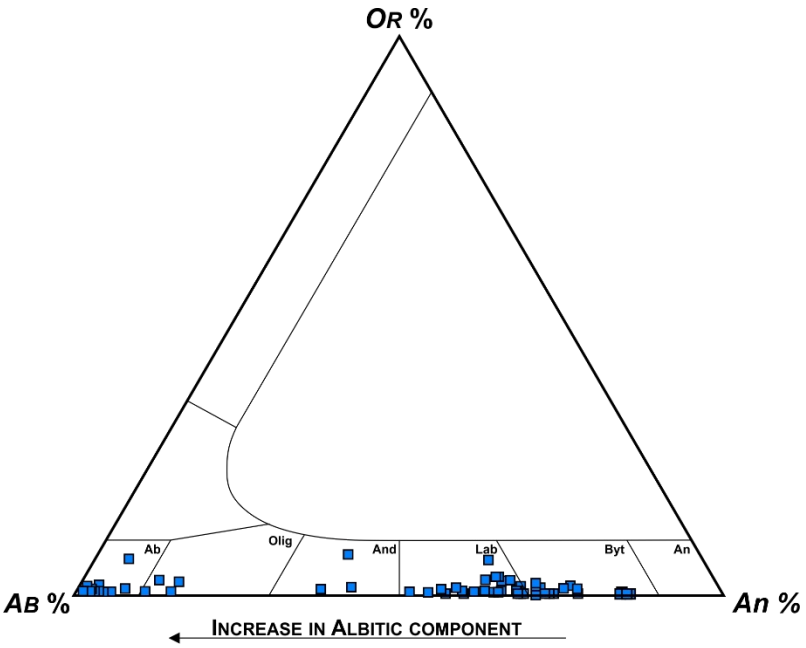

Figure IV.8- Triangular compositional diagram for feldspars based on *An%*, *Ab%* and *Or%* (adapted from Deer *et al.*, 2008). *An- anorthite; Byt- bytownite; Lab- labradorite; And- andesine; Olig- oligoclase; Ab- albite*.

IV.2.1.c. CHLORITE GROUP

Chlorite-group minerals are abundant throughout the whole volcanic sequence, having formed in the different alteration stages and found in different textural contexts (see Chapter IV.1). Its chemical variability was studied; 16 valid analyses were obtained, in 1 polished sections, belonging to the footwall volcanic sequence, sampled through the drill-cores (see Appendix VI). Due to the poor polishing of the polished thin sections, as previously mentioned, most of the performed analysis were considered as not-valid. Additionally, only the chlorite crystals found as vesicle infills exhibited appropriate dimensions and polishing to obtain acceptable analytical results.

Chlorites are characterized by a wide range of compositions, with a general crystallchemical formula $(R_u^{2+}R_y^{3+}[\ ]_z)^{VI}(Si_{4-x}Al_x^{3+})^{IV}O_{10}(OH)_8$, where the R^{2+} position is usually occupied by Mg, Fe^{2+}, Mn, Ni, Zn and R^{3+} by Al, Fe^{3+} and Cr; u+y+z=6 and z=((y-w-x))^2 and [ ] represents octahedral structural vacancies (Caritat et al., 1993). Chlorite structure is characterized by alternating octahedral-positive brucite layers and tetrahedral-octahedral-negative talc-like layers in 2:1 proportion (Caritat *et al.*, 1993).

The analysed chlorite grains are characterized by a wide variability of SiO_2 Al_2O_3 and MgO, with Ti and Cr as main trace elements.

The compositional variability of chlorite minerals can be explained by three substitution processes. I) the most common substitution found in chlorite minerals, the Tschermak exchange/substitution (TK), consists in the redistribution of charges between the tetrahedral and octahedral sites, but maintaining the overall charge balance given by $Al^{IV}Al^{VI}(Mg,Fe^{2+})_{-1}^{VI}Si_{-1}^{IV}$, $Al^{IV}(Cr^{3+})^{VI}Si_{-1}^{IV}(Mg,Fe^{2+})_{-1}^{VI}$ and $Al_2^{IV}(Ti^{4+})^{VI}Si_{-2}^{IV}(Mg,Fe^{2+})_{-1}^{VI}$; II) the di-octahedral substitution (AM), which creates octahedral structural vacancies, given by $Al^{IV}Al^{VI}[\ ]^{VI}(Mg,Fe^{2+})_{-2}^{VI}$; and III) the FM substitution, given by $FeMg_{-1}$ (Zane *et al.*, 1988).

In most of the analysed chlorites almost no Fe^{3+} is present. It is also interesting to note that there is a positive correlation between $(Al+2Ti+Cr)^{VI}$ - Al^{IV} *vs* $\sum VI$ (Figure IV.9 [A]), highlighting the influence of the TK substitution in the chlorites composition. Furthermore, the positive correlation between

$(Fe^{2+}+Mg)^{VI}$ and $(Si)^{IV}$- $(2[\ ])^{VI}$ (Figure IV.9 [B]) shows that the di-octahedral substitution (AM) is also one important mechanism that controls these chlorites chemical composition. Thus, these common substitutions cause deviations from the chlinochlore-chamosite compositions $[(Mg_5Al)(Si_3AlO_{10})(OH)_8]$, to more sudoitic compositions (Figure IV.19 [D]).

Chlorites chemical composition is recognized to be influenced by temperature, pressure and other physical-chemical parameters, hance its use as proxies for inferring such conditions, especially regarding the temperatures at which the mineral was formed. Thus, the chemical composition of chlorite serves as basis of several geothermometers; these can be divided into two different groups: I) empirical geothermometers, initially proposed by Cathelineau and Nieva (1985) and Cathelineau (1988), and later updated by several other authors, accounting for the cation exchanges between octahedral positions, producing better results (Jowett, 1991; Kranidontis & MacLean, 1987). They are based on the empirical relationship between Al^{VI} with temperature, based on observations for present-day active geothermal systems. Thus, these empirical models are often flawd, since they are only valid for minerals formed in equilibrium with the fluid, posing problems to long-lived and multistage paleo-systems. Additionally, some authors denote that the use of empirical geothermometers do not consider the bulk-rock composition as a factor controlling chlorites chemical composition (Bourdelle *et al.*, 2013); and II) (semi-)thermodynamic-based geothermometers, which offer better and more precise results, considering other parameters that control chlorites chemical composition. However, there are some uncertainties in these models, regarding the *P-T* data for the calibration of these models, innacuracies of the thermodynamic properties of chlorite solid-solution models and difficulties in the measurement of $Fe^{3+}$and accounting for it in the solid-solution models. Nevertheless, various models with a (semi-)thermodynamic base have been proposed (*e.g.* Walshe, 1986; Inoue *et al.*, 2009; Bourdelle *et al.*, 2013). Thus, for the calculation of the temperature of chlorite formation, the calculations were made using the above mentioned geothermometers (Figure IV.9 [E]). The Jowett (1991) and Bourdelle *et al.* (2013) empirical and thermodynamic-based geothermometers, respectively, were chosen as the most appropriate ones: the first - Jowett's empirical model – due to the fact it offers the best approximation and better results, for empirical geothermometers, while the use of Bourdelle *et al.*, (2013) (semi-)thermodynamic-based geothermometer was used considering it accounts for the whole-rock composition as controlling factor for chlorites composition. The analyses of the temperatures obtained suggests that these chlorites precipitated from hydrothermal fluids at temperatures between 195 to ~430ºC; the temperature data distribution is highly assymetrical, hence instead of the average, the appropriate measure of central tendency is the median, obtaining a T of 273ºC±13 ºC. It is also possible to conclude that the empirical approach yielded the highest values for chlorites, opposed to the (semi-)thermodynamic-based geothermometer, which produced lower temperatures (Figure IV.9 [F]). It is then plausible to ascertain that the temperatures obtained for the empirical geothermometers can be considered as the maxmium temperatures for chlorite formation and the thermodynamic-based ones allow to obtain the minimum temperatures for chlorite formation, for the same chlorite crystal.

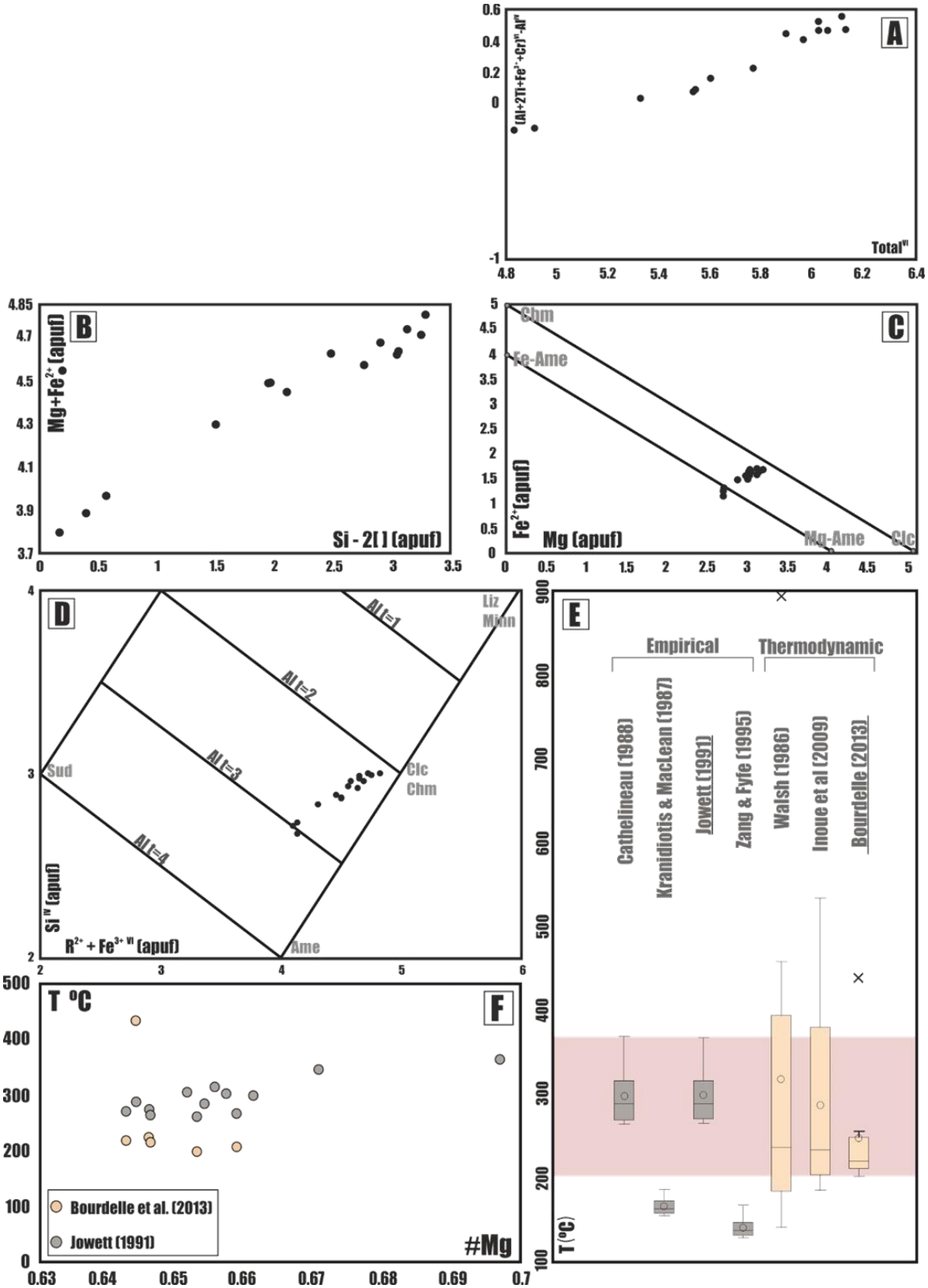

Figure IV.9- [A] $(Al+2Ti+Fe^{3+}+Cr)^{VI}$-Al^{IV} *vs* $Total^{VI}$ plot; **[B]** $Mg+Fe^{2+}$*vs* Si-2[ ] plot; **[C]** Fe^{2+} (apuf) *vs* Mg (apuf) plot **[D]** $(R^{2+}+ Fe^{3+})^{VI}$ *vs* $(Si)^{IV}$ plot, where the compositional end-members are defined as: Ame – amesite $[(Mg_4Al_2)(Al_2Si_2)O_{10}(OH)_8]$, Clc-Chm – chlinochore-chamosite $[((Mg,Fe^{2+})_5Al)(Si_2AlO_{10})OH_8]$, Liz-Minn – lizardite-minnesotaite $[(Mg_6(Si_4O_{10})(OH)_8]$, and Sd – sudoite $[(Mg_2Al_3)(AlSi_3)O_{10}(OH)_8]$; **[E]** Box-whiskers plot for comparing the obtained temperatures, using empirical [Cathelineau (1988), Kranidotis & MacLean (1987), Jowett (1991), Zang & Fyfe (1985)] and thermodynamic-based [Waslsh (1986), Inoue *et al.*, (2009) and Bourdelle *et al.*, (2013)] chlorite geothermometers, and in red, the considered temperature range for the analysed chlorites; **[F]** obtained temperatures using Bourdelle *et al.*,(2013)'s and Jowett (1991)'s geothermometers vs #Mg.

IV.2.1.d. INTERLAYERED CHLORITE-SMECTITE (*CHL-SME*)

Interlayered chlorite-smectite are 1:1 mixed-layer chlorite-smectite and/or chlorite-vermiculite. They are, by far, one of the dominant type of natural interlayereds that occur in natural systems, in low to high temperature conditions, in evaporitic deposits, soils, sedimentary and volcanic rocks, as well as in burial diagenetic processes, in fossil or active hydrothermal systems and even in contact or low-grade regional metamorphism. In the literature, the overall given chemical formula for interlayered *Chl-Sme* is $(Ca, Na, K)_{1-x}(Mg, Fe, Al)_9O_{20}(OH)_{10} \cdot nH_2O$.

Usually identified by X-Ray Diffractometry, the interlayered phyllosilicates in the present study were identified on the basis of their expansive properties and chemical composition of: $(Ca, Na, K)_{0.141}(Mg_{6.00}, Fe_{2.66}, Al_{0.76})\ \ (Si_{6.00}, Al_{1.99})_8O_{20}(OH)_{10} \cdot nH_2O$ (See appendix VII).

IV.2.1.e. ALUMINIUM RICH-PHYLLOSILICATES

In the open pit samples, where volcanic rocks exhibit more intense silicification processes, Al-rich phyllosilicates are found, together with quartz and pyrite, occurring as fine-grained aggregates. Their chemical composition is characterized by low amounts of Mg and Fe, besides Si and Al. (see Appendix VIII). The chemical analyses of these phyllosilicates were recalculated on a 9 and 12 oxygens base, but they failed to adjust to a specific aluminium phyllosilicate stoichiometry such as illite, montmorillonite, halloysite or kaolinite.

IV.2.1.f. ZEOLITES

Zeolites are found as secondary mineral phases, filling vesicles or sealing veinlets, along with calcite, during the first alteration stages. For the study of their chemical variability, 150 analyses were performed, in 4 polished sections, one from the hanging-wall and three from the footwall. Zeolite-group minerals are hydrated aluminium silicates with open framework of linked $(Si,Al)O_4$ tetrahedra. This framework contains cavities, which are occupied by H_2O molecules and non-framework cations; non-bridging anions can be protonated, becoming OH^-, or altogether substituted by F^- (Armbruster and Gunter, 2001).

The analysed grains are calcic zeolites, with little or no potassium and/or sodium. Although it is possible to distinguish different zeolites, based on the chemical analyses alone, it was not possible to assign these re-calculated analyses to a specific calcic zeolite stoichiometry, *e.g.* laumontite, stellerite, scolecite, wairakite or epistilbite. This can be interpreted as analytical inacuracy related to volatilization of light-weight components under the electron beam (Campbell et al., 2016). Nonetheless, two groups of analysis can be matched to coincide with epistilbite and laumontite's stoichiometry, with reasonable confidence (Appendix IX).

IV.2.2. CARBONATES

Carbonates, together with zeolites, hematite and chlorite, trace the late stages of the first alteration episode and/or the transition to the second; they occur as well in later re-opening of previous *Qz+Py* veins, together with pyrite, in the hydrothermal (*s.s.*) mineralizing stage. A total of 129 analyses were performed in 3 different polished sections, one belonging to the hanging-wall and two from the footwall rocks (see Appendix X). The analyses reveal a strong compositional homogeneity, around calcite ideal composition, around $(Ca_{1.76-1.96})CO_3$. Mn occurs as trace-element but no difference was found between Mn contents for hanging-wall vs footwall rocks and open-pit vs drill-core samples, despite the different textural contexts and the different precipitation episodes.

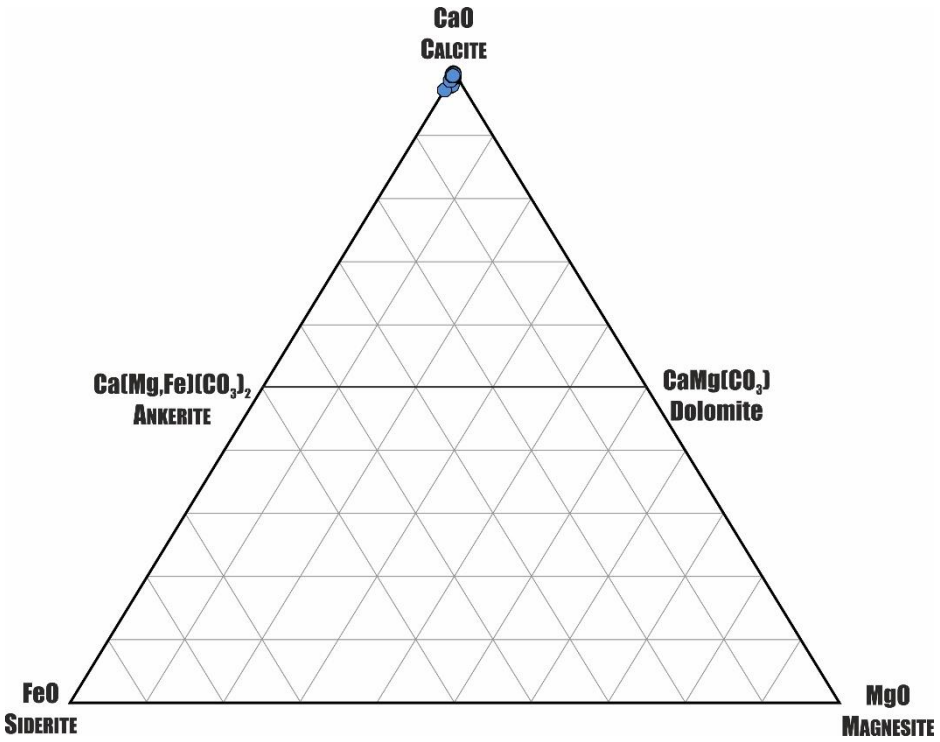

Figure IV.10- $CaCO_3$-$MgCO_3$-$FeCO_3$ ternary plot with the carbonate analyses from veins and vesicles found in the volcanic rocks.

IV.2.3. SULPHIDES

Sulphides are absent throughout the hanging-wall volcanic sequence, but are relatively common mineral phases within the footwall volcanic rocks. A total of 305 analyses were performed: 220 in pyrite crystals, 77 in chalcopyrite and 15 in sphalerite grains (Table IV.I).

All analysed pyrite crystals are found to have a homogeneous chemical composition, similar to the ideal pyrite chemical formula FeS_2, with $Fe_{0.96-0.99}S_{1.97-2.05}$, showing trace amounts of Co and, sometimes, Cu and Sb. This applies to all analysed pyrite crystal, regardless of all the different textural contexts: matrix, vesicles and the different pyrite hydrothermal precipitation phases.

The 82 chalcopyrite analyses also revealed a strong compositional homogeneity, close to the ideal composition of this mineral phase. The average composition is given as $Cu_{0.98}Fe_{0.99}S_2$, with systematic trace amounts of Mo, Zn and Co, and occasional trace amounts of In, Cd, Ag, Pb, As and Se.

Sphalerite crystals, occurring as (sub)euhedral grains in quartz + pyrite veins and disseminated within the matrix, exhibited a predominance of the sphaleritic component (*i.e.* Zn-rich), with average composition of $Zn_{0.95}Fe_{0.03}S_1$, showing trace amounts of Cu.

Table IV.1- Sulphide compositional variation (average, median, standard-deviation (σ), minimum, maximum, in *apuf*).

Pyrite

n = 221	Average	Median	Std-Dev	Min.	Max.
S	2.0032	2.0019	0.0123	1.9796	2.0505
Fe	0.9958	0.9965	0.0035	0.9607	0.9993
Co	0.0011	0.0007	0.0021	0	0.0189
Cu	0.0002	BDL	0.0013	0	0.0165
Sb	0.0007	BDL	0.0012	0	0.0061

Chalcopyrite

n = 77	Average	Median	Std-Dev	Min.	Max.
Fe	0.9911	0.9912	0.0140	0.9627	1.0244
Cu	0.9779	0.9749	0.0159	0.9442	1.0290
Zn	0.0012	0.0082	0.0012	BDL	0.0041
Mo	0.0006	0.0006	0.0005	BDL	0.002
Co	0.0005	0.0004	0.0004	BDL	0.0015
In	0.0002	BDL	0.0003	BDL	0.0013
Cd	0.0001	BDL	0.0003	BDL	0.0015
Ag	0.0002	6.8E-05	0.0003	BDL	0.0011
As	0.0002	BDL	0.0003	BDL	0.0015
Se	0.0005	0.0004	0.0005	BDL	0.0021
Pb	0.0004	0.0003	0.0004	BDL	0.0015

Sphalerite

n = 15	Average	Median	Std-Dev	Min.	Max.
Fe	0.0299	0.0227	0.0213	6.99E-5	0.0756
Zn	0.9067	0.9222	0.0557	0.7905	0.9693
Cu	0.0296	0.0029	0.0493	BDL	0.1526

IV.2.4. PHOSPHATES

Apatite occurs as an accessory mineral phase in hydrothermally (*s.s.*) altered volcanic rocks, as small crystals, disseminated within the rocks matrix and also in the doleritic rocks. The ideal composition of apatite is $Ca_5(PO_4)_3(F, Cl, OH)$, where Ca can be replaced either by monovalent cations, with loss of F, OH or Cl, thus developing structural vacancies, or by other divalent cations, or even by trivalent cations, with substitution of P by tetravalent anions (Deer *et al*., 2001).

The 9 analysed apatite grains are classified as fluorapatites with a chemical composition of $Ca_{4.69-5.05}(PO_4)_{2.97-3.12}F_{0.42-0.79}OH_{0.1625-0.435}Cl_{0.018-0.194}$, with Fe, Mg and Na occurring as trace elements (see Appendix XI).

Nevertheless, and despite the limited amount of analyses, the fluorapatites analysed in the doleritic rocks are characterized by higher median values of Cl^- (0.16 *apuf*), when compared to the hydrothermally altered rocks (0.05 *apuf*); the latter also show higher OH^- contents (0.35 *apuf*), comparing to the doleritic rocks apatites (0.31 *apuf*).

IV.2.5. OXIDES

Iron oxides occur as primary mineral phases in the volcanic rocks (magnetite), as euhedral crystals, sometimes with corroded cores and preserved rims, dispersed within the volcanic rocks groundmass, or as a secondary mineral phase, sealing veins and microfractures (hematite). As previously mentioned, due to poor polishing, analyses of secondary oxides had to be rejected.

These magnetite crystals are characterized by considerable amounts of Ti and Al, with Mn and Mg as trace elements (see Appendix XII). The magnetite analyses were recalculated on a 4-oxygen base but magnetite stoichiometry was not obtained, possibly due the low total elemental oxides- lower than 94.35%., conceivably due to poor polishing conditions.

IV.3. WHOLE-ROCK GEOCHEMISTRY

A total of fourty one samples, nineteen from the hanging-wall and twenty-two from the footwall, representative of the different alteration facies found throughout the volcanic sequence were chosen, for major and trace element analysis, with the purpose of characterizing the range of geochemical variability of the volcanic rocks, considering the above-mentioned aims for this study (Appendix XIII)

A correlation matrix, for the major and trace element data was computed and the correlation values (r) were considered as i) linear, very good if $|r| > 0.95$ (for positive and negative correlations); ii) good if $0.8 \leq |r| < 0.95$, both positive and negative linear correlations, but with some deviations and iii) |r| values between 0.75 and 0.8, as probable linear (positive and negative) correlations.

Expected results were obtained: no significant negative correlations were found, the most important positive correlations are as follows, Zn and Cd are found to have a very good correlation, as well as Sb with As. Y establishes a very good correlation with the HREE, Zr with Hf and Th and Nb with Ta. Also, the HREE show very good correlations amongst themselves and good correlaions with LREE. P_2O_5 covaries positively with Nb, Ta and LREE, while K and Ba are characterized by having good linear correlations between the two. Cu develops good correlations with As, Ge, Mo, Cd and Tl; while Zn has a good correlation with U. Titanium establishes good correlations with Th, Zr, Nb and with most of the REEs, Zr with the REEs and Th, Cr with Ni, Co with Se, As with Tl and Pb, Ag with In, Sb, Tl and Pb; Cd with U.

IV.3.1. MAJOR ELEMENTS

The major element geochemistry data is presented in Harker Diagrams, where Fe_2O_3, Al_2O_3, MgO, CaO, Na_2O, K_2O, TiO_2 and P_2O_5 have been plotted against SiO_2 (Figure IV.10 (I) and (II)).

The Al_2O_3 *vs* SiO_2 plot shows that most of the hanging-wall samples follow a negative linear trend, with some dispersion, following a decrease in SiO_2 contents and Al_2O_3 enrichments tendency. This is related to the low magmatic differentiation, possibly enhanced during oceanic metasomatic alteration but also attributed to the formation of secondary Al-bearing mineral phases in more intensely altered footwall samples. Despite this, the difference between the previously described trend, for the hanging-wall and this, lies in the distinct nature of the alteration processes that affect the two groups: while oceanic metasomatism consists mainly in phyllosilicate formation, therefore there is an increase in aluminium contents, the hydrothermal alteration that affects footwall rocks is characterized not only by chlorite precipitation but with variable silicification processes, causing an increase in SiO_2. One sample deviates considerably from these two trends, with lower Al_2O_3 values and high SiO_2 contents and it corresponds to a jasper sample, formed during exhalative hydrothermal activity. The plot of Na_2O *vs* SiO_2 shows a relative linear correlation, with increase of Na_2O accompanied by gains in SiO2, related to the albitization of the feldspar microlites and microphenocrysts, during oceanic metassomatic alteration and also preserved in some footwall volcanic rocks. As for the plot K_2O *vs* SiO_2, no linear correlation is found, with large dispersions found for the hanging and footwall samples.

In the $Fe_2O_{3\ tot}$ *vs* SiO_2 plot it is also possible to distinguish an inverse linear trend, defined by the hanging-wall and footwall samples; one of the footwall volcanic rocks is characterized by significantly higher contents in Fe_2O_{3tot}, possibly related to more intense hydrothermal alteration, possibly related to pyritization processes. The exhalate sample thas a considerable increase in Fe_2O_3 due to the abundance of iron oxi-hydroxides. Regarding the CaO *vs* SiO_2 plot, the hanging-wall samples also follow an inverse compositional linear trend, with some of the samples of this group defining another trend, characterized by lower CaO contents. Even lower CaO values characterize the footwall samples and the jasper sample.

The trend observed for the hanging-wall samples possibly reflects magmatic trend for these rocks, where the alteration of *Cpx* and the albitization of the plagioclase was possibly compensated by the neo-formation of secondary Ca bearing mineral phases, such as epidote, carbonates and zeolites, during oceanic metasomatism. For the footwall volcanic rocks, the Ca contents are significantly lower, due to hydrothermal leaching, which produces rocks with few Ca-bearing mineral phases. The MgO *vs* SiO_2 can be characterized using a similar reasoning: the recognizable trend reflects magmatic differentiation tendency, where the precipitation and neo-formation of Mg bearing minerals (*e.g.* chlorite) explains why both hanging and footwall rocks follow the same trend.

The P_2O_5 *vs* SiO_2 and MnO *vs* SiO_2 plots are fairly similar: overall low P and Mn values, for both hanging and footwall volcanic rocks, with significant increases in P and Mn in the jasper sample. The plot of TiO_2 *vs* SiO_2 reveals two distinct trends: one with the increase of TiO_2 with SiO_2, mostly recorded by the hanging wall samples, and likely related to magmatic differentiation and Ti-magnetite formation, and a second trend, observed for the footwall and some hanging-wall volcanic rocks, characterized by decreases in TiO_2, possibly related to those oxides alteration during progressive alteration.

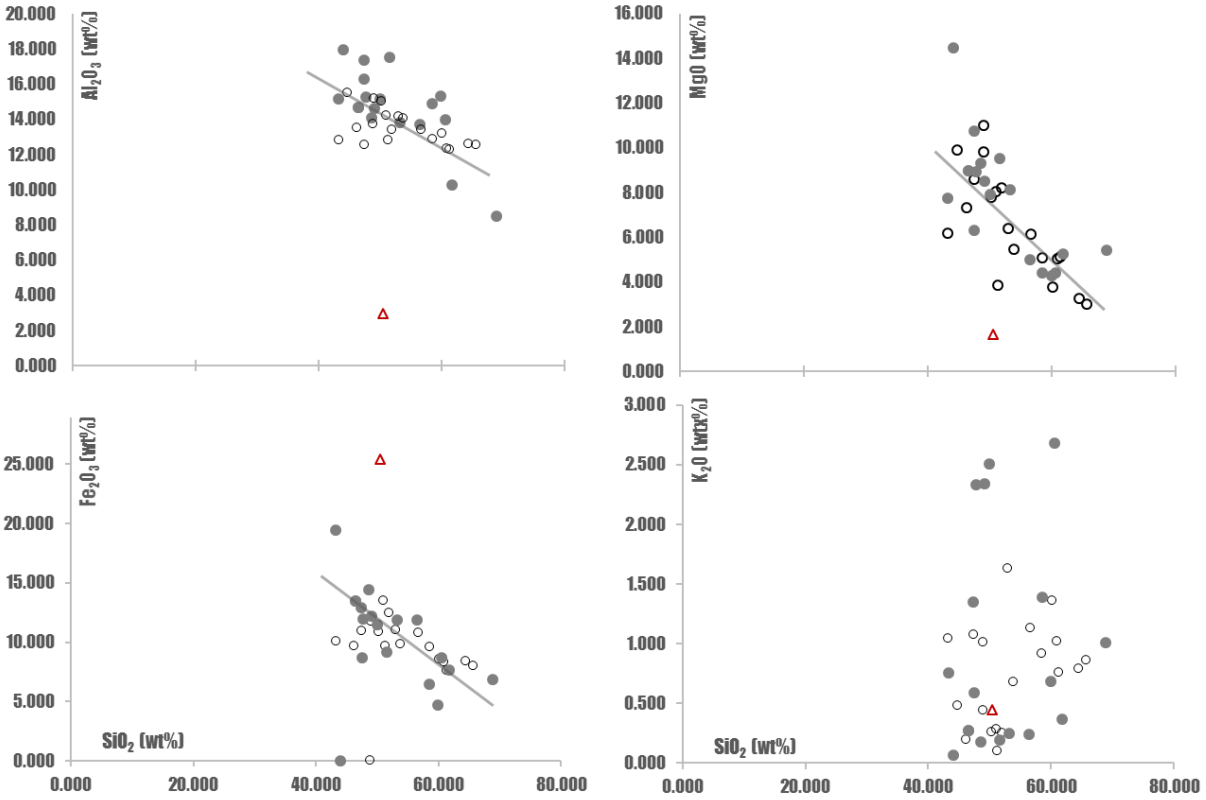

Figure IV.11 (I)- Harker diagrams correlating Al2O3, MgO, Fe2O3and K2O vs. SiO2, for hanging wall samples (open circles) and footwall volcanic rocks (filled circles). Red triangle represents jasper sample.

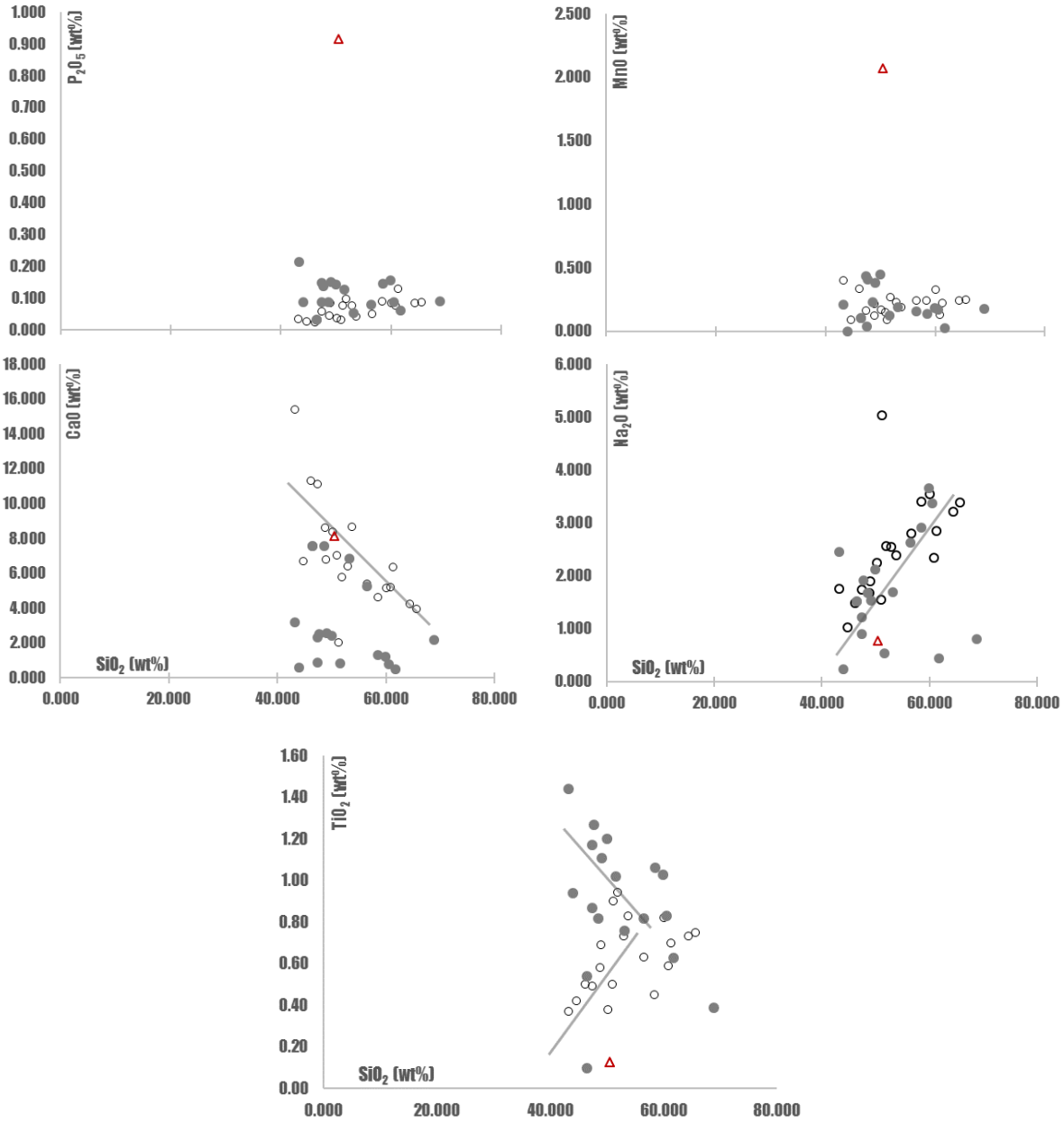

Figure IV.11 (II)- Harker diagrams correlating Al2O3, MgO, Fe2O3and K2O vs. SiO2, for hanging wall samples (open circles) and footwall volcanic rocks (filled circles). Red triangle represents jasper sample.

IV.3.2. MINOR AND TRACE ELEMENTS

Minor and trace elements occur in the primary mineral phases structure and some of them are found to have immobile behaviour during alteration. In this section, the variation of minor and trace elements will be assessed, using I) REE patterns, and II) Spider diagrams. Some lithogeochemical indices will also be used, to evaluate the relationship between mineralogical and geochemical data, thus providing a qualitative interpretation of the alteration degree these rocks underwent, as well as a basis for mass balance calculations.

IV.3.2.2. C1-NORMALIZED REE

For the C1[2] chondrite-normalized REE plots (Figure IV.11), samples were grouped according the intensity of the alteration exhibited, and the Eu* and Ce anomalies were calculated. The first is calculated using the expression $Eu/Eu^* = Eu_N/(Sm_N \times Gd_N)^{0.5}$, and it measures the depletion or enrichment, relative to Sm and Gd. The Ce anomaly measures its enrichment or depletion in relation to La and Sm, and ($Ce/Ce^* = 5Ce_N/(4La_N + Sm_N)$), being negative when its value is lower than 1.

REE patterns for hanging-wall volcanic rock samples (Figure IV.11 [A]), exhibiting only evidence of oceanic metasomatic alteration, are characterized by a LREE (~3 to 20× C1) depletion, relative to HREE (7 to ~30× C1) – $\overline{(La/Lu)_{CN}} = 0{,}3$, an increasing LREE segment and a relative flat HREE pattern. Two samples display a mild negative Eu anomaly, otherwise the Eu anomaly is absent (Eu*= 0,804 to 1,097). The samples are, overall, characterized by a negative Ce anomaly, expcet for two samples (Ce* = 1.00 and 1.09), with values spanning from 0.80 to 0.99. Overall, whithin this group it is possible to distinguish two sub-groups: one with higher bulk REE and, the other characterized by significantly lower bulk contents.

The second group is composed of the footwall volcanic rock samples which show a lower hydrothermal alteration (dissemination of pyrite, incipient chloritization and/or silicification) with common oceanic metasomatic alteration evidences, as a well as the low-T hydrothermal episode (hematite-bearing veins) (Figure IV.11 [B]). They show a REE pattern similar to the first group, differing on a less steep slope of the LREE segment and lower LREE/HREE fractionation ($\overline{(La/Lu)_{CN}} = 0{,}71$), although, as a group, the REE contents are higher than the first group. Some samples exhibit a negative Ce (0,826 and 0,847) and Eu anomaly, in spite of positive-sloped LREE segments.

The third group (Figure IV.11 [C]) comprises the footwall samples that show the most intense hydrothermal alteration (moderate to intense silicification, chloritization and pyrite dissemination) and consequently the widest range of variation in their REE patterns (see also Figure IV.12 [C]). The fractionation between LREE and HREE becomes less pronounced ($\overline{(La/Lu)_{CN}} = 0{,}693$), sometimes with mild LREE/HREE enrichments. The Eu anomaly becomes more pronounced, being positive in the case of two samples (MD-P2-4-1 and MD-P2-4-2), which also show the lowest bulk REE concentrations.

The typicalREE compositions of N-MORB, E-MORB, OIB, BAAB and, more specifically, Lau Basin's basaltic rocks REE compositions were added (Figure IV.11 [D]) for comparison.

The studied REE patterns are characterized by overall REE depletions, low LREE/HREE, Eu and, in some cases, Ce anomalies. These rocks REE contents are consistent from being relatively evolved, derivate liquids from gabbroic rocks, in which plagioclase crystallized, having retained the Eu. They are

[2] C1 Chondrite data from Palme *et al.* (2012) (Appendix XI)

altogether similar with present-day back arc basin basaltic rocks (Tonga back-arc) or N-MORB basalts. Nevertheless, their overall REE contents are lower possibly result from being derived from a mantelic source from which MORB-like melts were previously extracted. Additionally, alteration processes are also responsible for REE contents modifications such as bulk REE decrease and development of Ce negative anomalies, which indicate that REE were mobile during both sea-water regional alteration, as well as during hydrothermal alteration. Additionally, the positive Eu anomaly, seen in the more hydrothermally altered samples, translate a direct influence of hydrothermal fluids, typically characterized by such Eu anomalies.

Table IV.2- REE ratios for the Hanging and Footwall volcanic rocks

Hanging-wall					
n= 19	Average	Median	Std-Dev	Min	Max
La/Sm	0.522	0.527	0.07	0.417	0.624
Ce/Ce*	0.928	0.939	0.067	0.804	1.097
Eu/Eu*	0.899	0.917	0.055	0.798	0.963
$(La/Lu)_{CN}$	0.419	0.399	0.110	0.204	0.597
$(La/Yb)_{CN}$	0.423	0.422	0.105	0.212	0.598
$(La/Nd)_{CN}$	0.596	0.602	0.052	0.523	0.679
$(Sm/Yb)_{CN}$	0.804	0.804	0.130	0.493	1.017
Footwall					
n= 22	Average	Median	Std-Dev	Min	Max
La/Sm	0.685	0.596	0.056	0.419	1.273
Ce/Ce*	0.953	0.999	0.144	0.624	1.129
Eu/Eu*	0.847	0.876	0.254	0.482	1.494
$(La/Lu)_{CN}$	0.675	0.667	0.247	0.267	1.141
$(La/Yb)_{CN}$	0.672	0.682	0.244	0.270	1.171
$(La/Nd)_{CN}$	0.680	0.617	0.163	0.488	1.049
$(Sm/Yb)_{CN}$	0.979	0.958	0.202	0.629	1.331

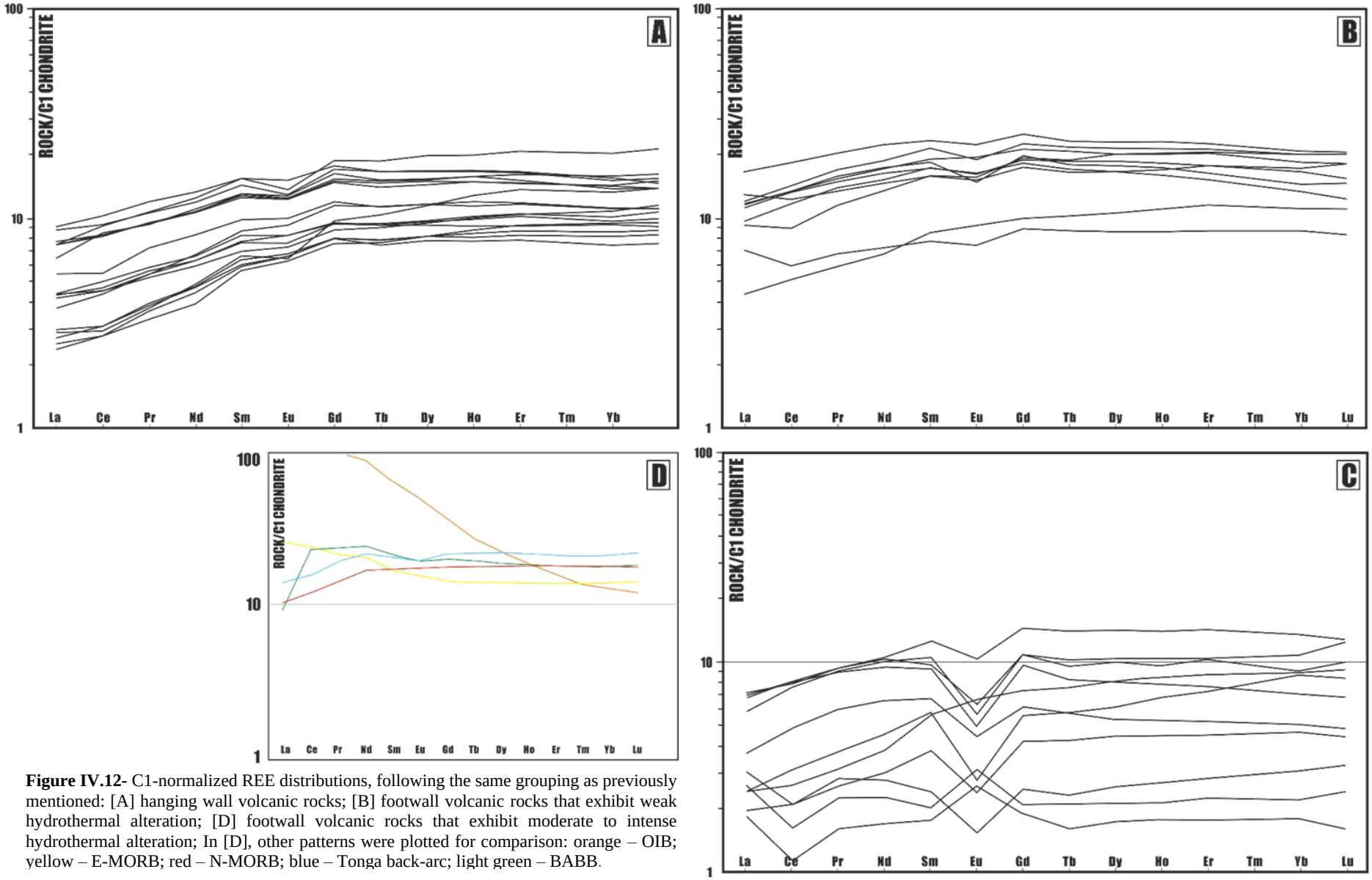

Figure IV.12- C1-normalized REE distributions, following the same grouping as previously mentioned: [A] hanging wall volcanic rocks; [B] footwall volcanic rocks that exhibit weak hydrothermal alteration; [D] footwall volcanic rocks that exhibit moderate to intense hydrothermal alteration; In [D], other patterns were plotted for comparison: orange – OIB; yellow – E-MORB; red – N-MORB; blue – Tonga back-arc; light green – BABB.

IV.3.2.2. SPIDER DIAGRAMS

Representation of the different elements follows the increasing atomic number growth, from left to right, and samples were PM-normalized. They were also grouped according to the criteria previously defined: the first group of samples corresponds to the hanging wall rocks that chiefly display the effects of oceanic metasomatism. The two other groups comprise footwall samples: the second group comprises volcanic rocks with weak hydrothermal alteration, while the third is composed of samples which show evidence of more intense and pervasive alteration. This allows the distinction of the geochemical signatures and their correlation with each alteration episode.

Figure IV.12 [A] shows that the hanging-wall volcanic rock samples, which exhibit only oceanic metasomatic alteration, show very similar and consistent patterns, with low P values (0.2 to 2× PM), Cu and Zn (~1× PM), a positive low-Ti anomaly (2 to 5× PM) and moderate K (3 to ~12× PM) As (~8 to ~150× PM), Sb (3 to ~16× PM), and Bi (~5× PM) enrichments, as well as Pb (3 to ~17× PM) and U (from ~1 to 10× PM). Elements such as Rb, Sr, Ba and REE are also characterized by 1-10xPM variations. Conversely, the multi-elemental patterns for these rocks are marked by deep Cr, Ni and Cs negative anomalies, with lower-magnitude – and sometimes more variable – Co, Nb, Ta and Th negative anomalies, relatively to the PM.

For the second group (Figure IV.12 [B]), which consists in samples that show evidences of oceanic metassomatic alteration (mostly albitized plagioclase), some evidences of the low-T hydrothermal event (hematite veins) and of hydrothermal mineralization (disseminated pyrite and incipient to moderate silification), the patterns are characterized by identical titanium concentrations (in relation to the first group), similar low concentrations in K, P, Cr, Ni and Cs and a substantial variation, *i.e*. enrichment, in Zn (4 to 60 × PM), Cu (2 to 20 × PM), As (~70 to 1000× PM), Cd (~2 to 8× PM), Sb (~7 to 100× PM), Pb (~5 to 50× PM) and U (~4 to ~17× PM).

The patterns for the more hydrothermally altered samples (figure IV.12 [C]) show a slightly wider range of variations, for a given element in comparison to the samples pictured in [B]. Ti and P values and the Cs negative anomaly are also similar to the one described for the previous groups and the positive anomalies evident in the preceding diagrams are present – for K, As, Sb, Ba, Pb, Bi and U – although they show a broader range of variation: in the case of Ti, the positive anomaly decreases, whereas Cs, Zr and Nb (and, to some extent, Ta) anomlalies become more negative, relative to PM values. Cu, Co, As, In, Sb, Pb and U increase prominently in samples that show more intense hydrothermal alteration. The two samples with the highest As, Cu and Pb enrichment and the most depleted Sc, Ti, Rb, Nb and REE concentrations, show pervasive silicification and pyritization with only small remnants of a thoroughly chloritized basalt. The sample with the second highest As, Cu and Pb concentrations coincides with the jasper sample, cut by mineralized hydrothermal veins, with *Qz*, *Py* and *Ccp*.

Spider N-MORB-normalized diagrams were not made, although it is a common practice, since they are not found to be useful, as the MORB “group” (N-MORB, E-MORB, T-MORB suites) trace elements abundances constitute a complete continuum spectrum of compositions, spanning from the more depleted MORB’s to OIB-like REE contents (Hofmann, 2014).

The mild positive Ti anomaly, together with the negative Co, Ni, Cs and Cr anomalies translate primary magmatic trends and are compatible with a basaltic melt, extracted from a MORB-like mantle source; the detailed affiliation of these volcanic series will be further explored in section IV.5. These patterns also reveal that the rocks hosting the Mandoos deposit experienced several trace-element compositional modifications, during the different stages of alteration. The U, Pb and As positive anomalies, as well as those observed for Sb, Rb and Sr are most likely the result of sea-water induced regional alteration

(oceanic metasomatism), since most of these elements are usually mobile in the presence of oxidizing fluids. Several other positive anomalies, such as Cu, Zn, Pb, Ba, In and Cd can be explained by the influence of hydrothermal ore-forming processes of different intensities.

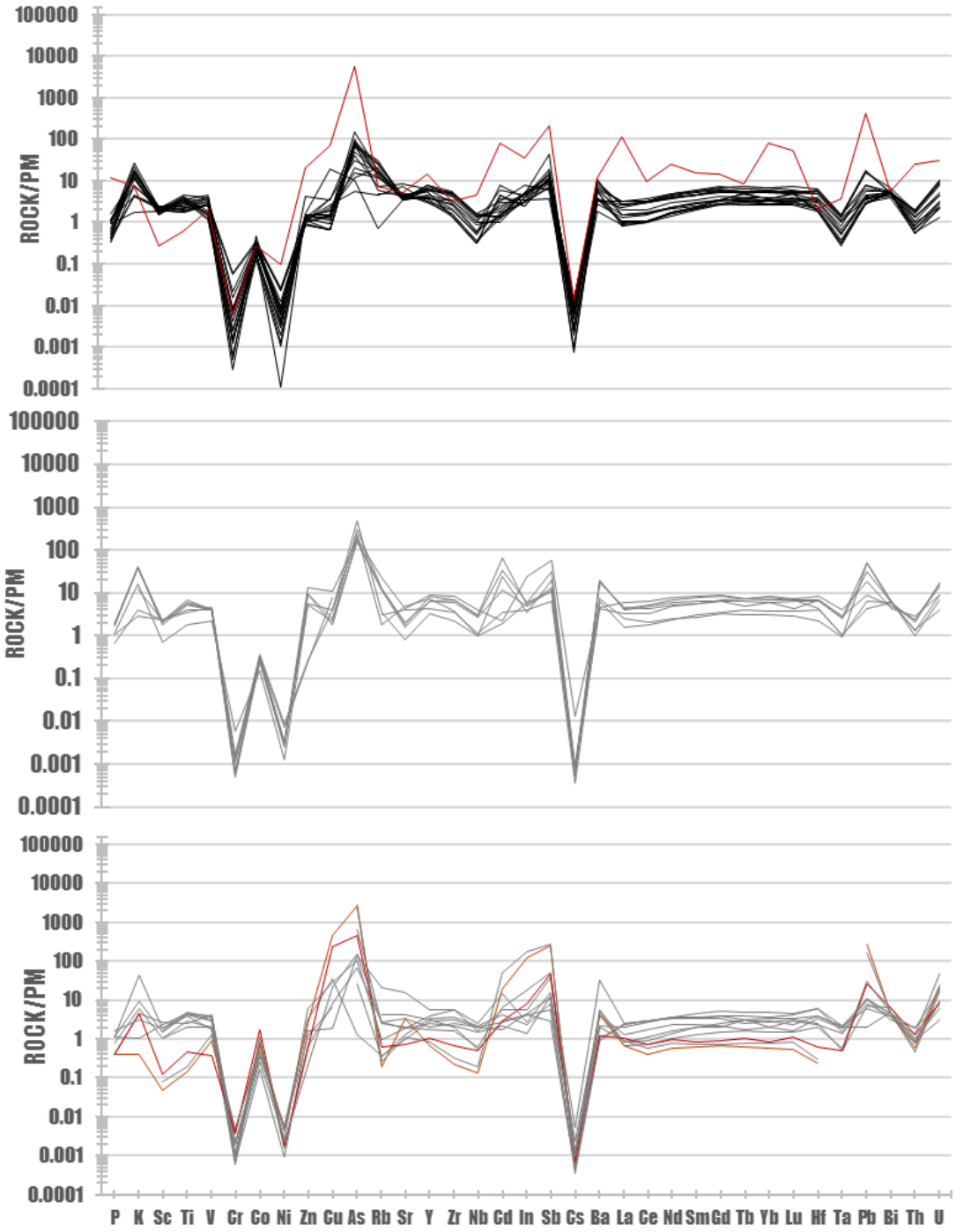

Figure IV.13- PM-normalized multi-elemental diagrams (spider diagrams); the first group of samples correspond to hanging-wall samples, while the second and third group comprise samples hydrothermally altered volcanic rocks. The second group preserves effects of oceanic metassomatism; the third group corresponds to the samples which show a more intense hydrothermal; In first group, the red line represents a jasper/umber, while in the third spider diagram it represents a mineralized jasper; the brown line represents sub-superficial massive sulphide replacement

IV.3.4. ALTERATION INDEXES

The volcanic rocks that host the Mandoos massive sulphide deposit record mineralogical and compositional modifications attributed to different, and superimposed, alteration stages, not all of them related with hydrothermal ore forming processes. To geochemically differentiate among the various alteration stages, Large *et al.*, (2001) proposed the use of a plot that relates mineralogical transformations with geochemical data and the gain/loss of particular elements, during these alteration processes. This allows the distinction between alteration stages with metallogenetic significance and regional, diagenetic trends. Two indices are proposed: the AI (Ishikawa Alteration Index) and the CCPI (chlorite-carbonate-pyrite index), each each related with typical mineral assemblages associated with both regional/diagenetic processes (*e.g.* feldspar hydrolysis and albitization during widespread oceanic metasomatism) and ore-forming hydrotermal events (*e.g.* chloritization and pyritization of volcanic rocks, closer to the mineralization).

$$AI = \frac{100(K_2O + MgO)}{(K_2O + MgO + Na_2O + CaO)}$$

$$CCPI = \frac{100(MgO + FeO)}{(MgO + FeO + Na_2O + K_2O)}$$

The Mandoos samples in this diagram (Figure IV.16) define a clear trend for some samples related with the following compositional modifications: i) chlorite and pyrite (trend 3); ii) carbonate ± sericite (trend 5) for the hydrothermal trends. As for the diagenetic trends, it is possible to identify the albite-chlorite (trend 7) and albite-chlorite-epidote (trend 8) mineral associations. Some dispersions are also observed, simulating other compositional tendencies, such as the diagenetic trend 9, possibly resulting from the combination of other two, such as the trend 5 and 7. Despite this, there are numerous samples that fall within the least altered box, even those that show pervasive hydrothermal alteration. This may be due to the superimposed alteration phenomena: *e.g.* first, a diagenetic trend such as 7 and afterwards, hydrothermal ore-forming alteration that follows vector 5.

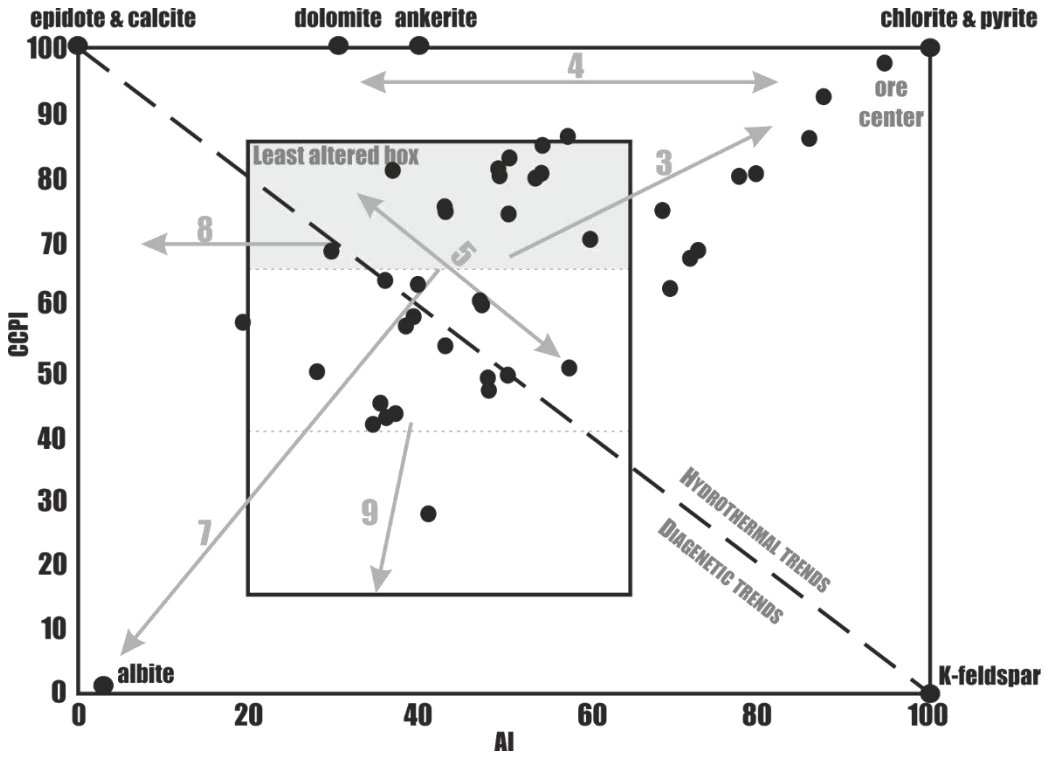

Figure IV.14 (Previous page)- Alteration box-plot with hanging and footwall volcanic rocks. The trends (arrows) are from Large *et al.* (2001): Hydrothermal trends: 3- *Chl*-Py; 4- *Chl-Cb*; 5- *Cb±Ser*; Diagenetic trends 7- *Ab-Chl*; 8- *Alb-Chl-Ep;* 9- *K-feldsp-Ab*. The shaded area represents the least altered plot for the basaltic and andesitic rocks compositions, according to Large *et al.* (2001)

The use of major and trace alteration indices proposed by Häussinger (1993), together withtogether with AI and CCPI (Large *et al.*, 2001) can be a useful tool in exploration surveys, as they discriminate different compositional trends, associated to: a) widespread regional alteration effects (Field III); b) diffuse and exhalative hydrothermal activity- without associated mineralization (Field I); and c) compositional modifications associated to ore-forming hydrothermal systems (Field II). This has been successfully applied by other authors in different VMS metallogenetic provinces, such as the IPB (Codeço, 2015). These indexes are calculated through the equations:

$$AI_{major} = \frac{\sum Fe_2O_{3_{tot}} + MnO + MgO}{\sum Fe_2O_{3_{TOT}} + MnO + MgO + CaO + K_2O + Na_2O};$$

$$AI_{trace} = \frac{\sum Cu + Zn + Pb + As}{\sum Cu + Zn + As + Pb + Rb + Sr}$$

The computed indices for the volcanic rocks that host the Mandoos massive sulphide deposit are represented in Figure IV.15:

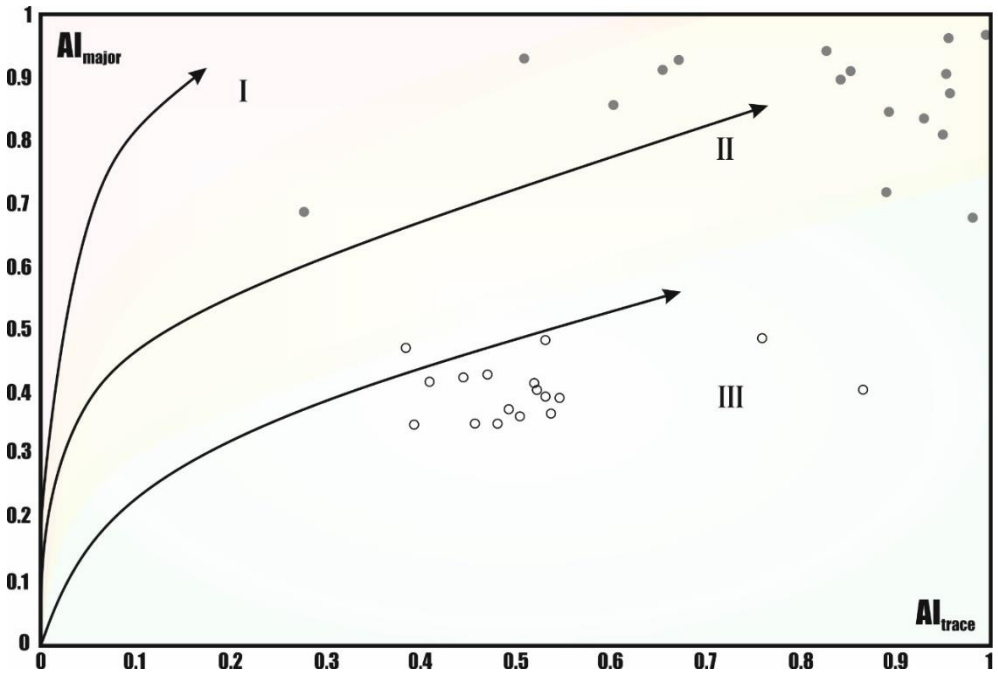

Figure IV.15- AI_{trace} *vs* AI_{major} plot, for the volcanic rocks that host the Mandoos deposit. Open circles represent hanging-wall samples and grey-filled circles footwall volcanic rocks; Field I defines diffusive, barren, hydrothermal activity; Field II represents ore-forming hydrothermal systems; Field III defines trends related to regional alteration

These indices yield more interesting results, which follow petrographic evidence more closely. All hanging-wall samples, which show no mineralization or hydrothermal activity related to sulphide precipitation fall in field III, corresponding to a widespread and regional alteration- oceanic metasomatism. Most of the footwall volcanic rocks fall in the upper right corner of the diagram, plot with high AI_{major} and AI_{trace} indexes, within field II, where rocks affected by hydrothermal alteration related to ore-forming hydrothermal systems plot. Despite of the good results some dispersion is observed, possibly due to a heterogeneous, multi phase alteration history; that is the case of rocks displaying less pervasive hydrothermal alteration but still preserving some of the mineralogical aspects related to oceanic metasomatic alteration.

. IV.3.5. ELEMENT MOBILITY

Considering the range of alteration of the studied rocks, it is essential to assess the mobility of some elements, especially of trace elements, during the course of the recognized alteration strages. Immobile elements can be used for mass balance calculations which are important to quantify mass exchanges that occur within alteration zones. Understanding element mobility is paramount to establish mineral exploration criteria and for petrological applications, such as determining protoliths and the magma-type, besides geodynamic/tectonic setting in which the rocks erupted.

The recognition of metasomatic and hydrothermal (*s.l.*) alteration processes in the studied rocks eliminates the possibility of using LILE elements such as K, Rb, Sr, Eu, Cs or Ba, as their considerate mobility during these processes is well documented (*e.g.* Rollinson, 1993). It is then more useful to use HSFE (*e.g.* REE, Zr, Hf, Ti, Nb, Ta, Pb) since they show relative immobile behaviour during alteration phenomena (Rollinson, 1993). Some authors select REE, Ti, Zr, Al, Hf, Y, and in some cases, Cr, V and Sc, as the least mobile elements (*e.g.* McLean & Kranidiotis, 1987; McLean, 1990; Barret & McLean, 1994). Despite of the overall evidence, it has been reported (*e.g.* McLean & Barret, 1993), that Y and REE may be fairly mobile under some specific conditions (in comparison to other HSFE), reason why it is advisable to test their behaviour. The basis for the use of immobile elemens is that their ratios will remain constant throughout any alteration process the rocks may undergo.

The TiO_2 *vs* Zr (Figure IV.16 [A]) plot reveals a well-defined trend, especially for the hanging wall samples, between two extreme positions, probably recording their primary compositions. Regarding the plots Zr *vs* Al_2O_3 and TiO_2 *vs* Al_2O_3 (Figure IV 16 [C] and [B], respectively) a wide dispersion is recorded, being wider for the hanging-wall samples. The normalization of immobile elements allows to remove the dispersion effects during multiple alteration processes, allowing to devise trends more clearly. Hence, the use of Al_2O_3/TiO_2 vs Zr/TiO_2 plot should be useful in the distinction of different igneous protoliths. The interpretation of the Figure IV.16 [D] suggests that the previously observed dispersion (Figure IV.16 [B]) is due to the mobility of this element (Al) during alteration processes, rather than due to the existence of different compositional protoliths.

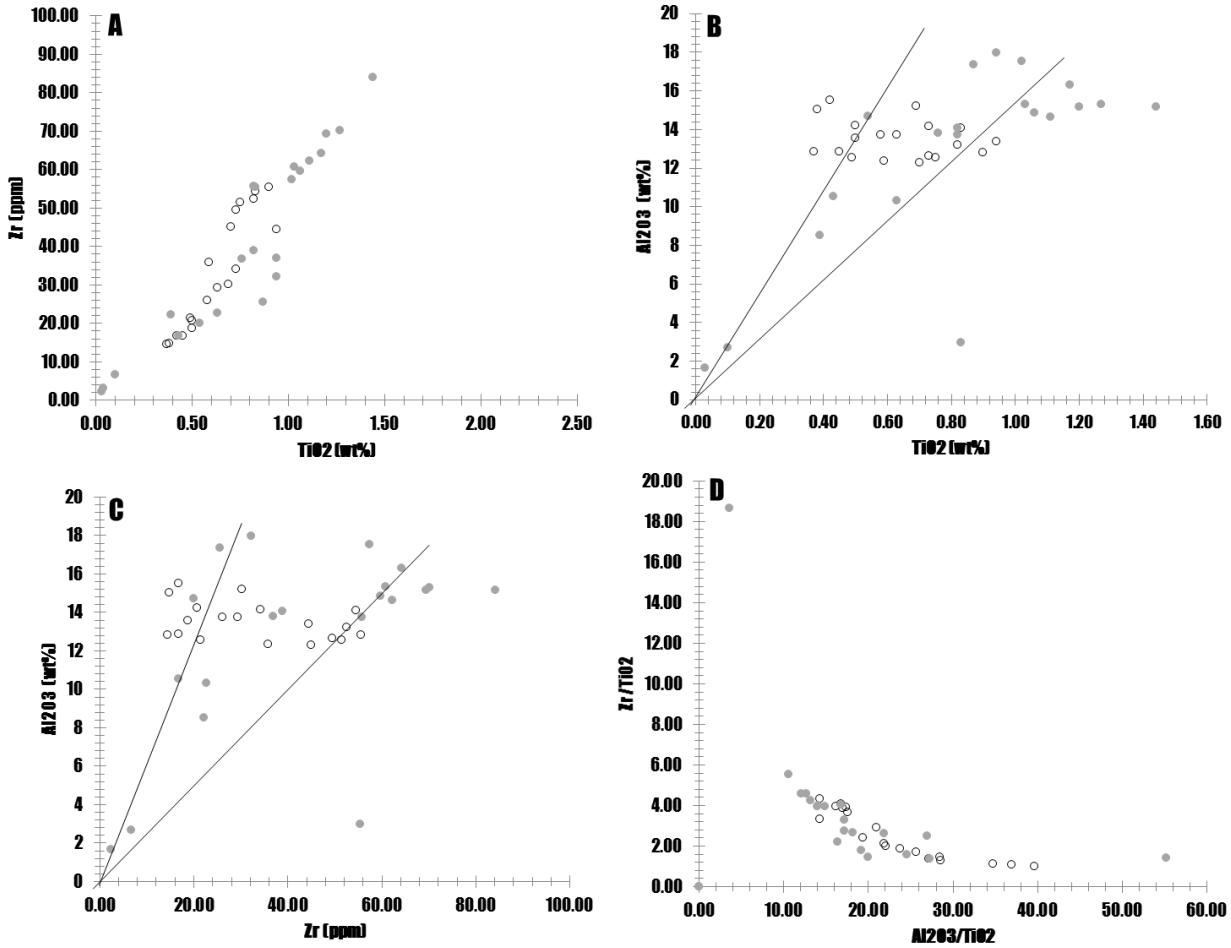

Figure IV.16- [A] TiO_2 *vs* Zr plot; **[B]** TiO_2 *vs* Al_2O_3 plot; **[C]** Zr *vs* Al_2O_3 plot; **[D]** Zr/TiO_2 *vs* Al_2O_3/TiO_2 plot. Open circles represent hanging-wall samples and the grey-filled circles, the footwall volcanic rocks.

Binary plots for HFSE, REE, Y and Fe against TiO_2 and Zr (Figure IV.17) reveals that, in addition to Al, such elements as Fe, Ba, Y, Co and to less extent La, show some mobility, especially during the most intense hydrothermal alteration processes. Thus, V, together with Sc and Fe_2O_3 chiefly show mobile behaviour, especially during metasomatic alteration but also during hydrothermal alteration. Similarly, Ba and Y are also mobile, but in this case, more so during hydrothermal alteration processes. It is also possible to conclude that elements such as Zr, Ti, Hf and Ta show an immobile behaviour, whereas elements such as Nb, Y or Yb showing an overall immobile behaviour but, under certain alteration conditions, they can show be mobile.

.

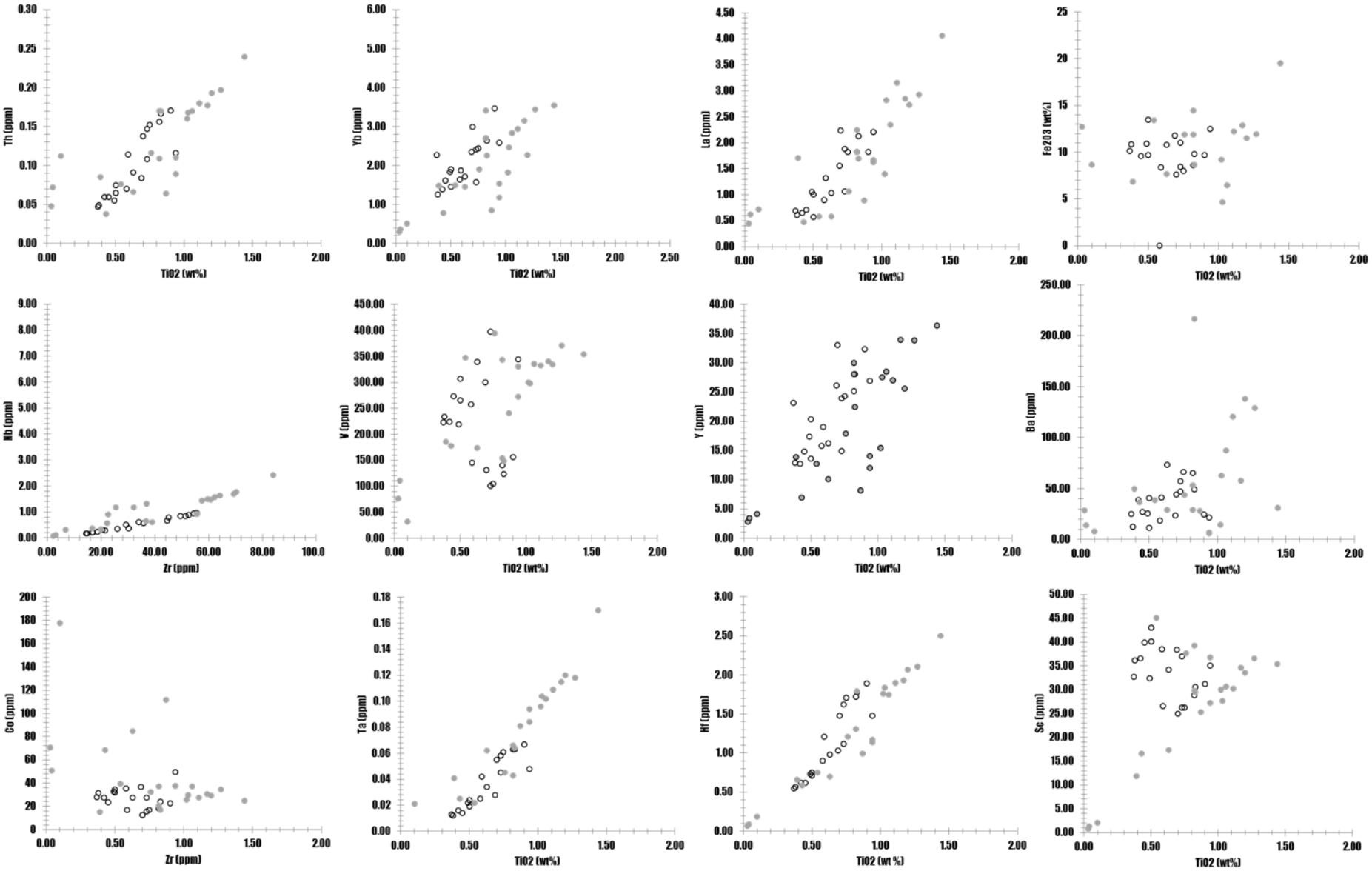

Figure IV.17 - Th, Yb, La *vs* TiO_2, Nb *vs* Zr and Hf, Nb, Ta, Y and Fe_2O_3 *vs* TiO_2 plots. The circles which are not filled represent hanging-wall samples and the grey-filled ones, the footwall volcanic rocks.

I.V.3.5. MASS BALANCES

Mass balance calculations are extremely important to characterize the alteration processes the rocks underwent. This is useful in the definition of proxies for mineralized, productive hydrothermal systems during exploration surveys. Using the procedure reported in MacLean (1990) procedure, also indicated in MacLean and Barret (1993) and Barret (2008), the elemental mass balance calculations were made using the expression:

$$\Delta x = C_{(x,altered)_f} - C_{x,protolith};$$
$$C_{(x,altered)_f} = f \times C_{x,altered};$$
$$f = [C_{immobile,protolith}/C_{immobile,altered}]$$

where $C_{(x,alt)_f}$ represents the concentration of a given element (x) in the altered rock, multiplied by an f factor, which represents the ratio between an immobile element in the precursor and the concentration of the same immobile element, in the altered sample. For these calculations, f was calculated using TiO_2 and Zr previously proved to be immobile (see IV.3.4).

The **precursor composition** was obtained by calculating the average values of the elemental concentrations for samples MD431-42.1 and MD431-91.0. These samples represent rocks with less intense metasomatic alteration, amongst the studied hanging-wall volcanic rocks. This chosen precursor composition bears, nonetheless, some alteration which cannot be quantified. Despite the mass gains related with the infilling of vesicles and veins, such alteration probably resulted in a negative mass balance, related to the alteration of primary igneous phases and leaching of some mobile elements.

The mass balance calculations considered the alteration of the calculated precursor for the different hydrothermal "facies", throughout the whole sampled area based on their intensity, mineralogy and location. Thus, four samples from the open pit were used (**group 1)**: i) two samples showing weak to moderate hydrothermal alteration, with pyrite dissemination, mild silicification, *Zeo+Qz* veins and zeolites infilled vesicles, with preserved albitized microlites in the rocks matrix (MD-P2-8-1 and MD-P2-9-1); ii) one sample showing moderate to strong hydrothermal alteration, related to the sulphide mineralization, with moderate silicification, pyrite, chalcopyrite and sphalerite dissemination (MD-P3-1-1); and iii) one sample showing intense hydrothermal alteration and brecciation, with quartz and sulphides (*Py*, *Ccp*, *Sph*) replacing the basaltic rock and infilling veins, where chloritized, silicified cores are preserved (MD-P2-4-1). Additionally, three samples from the SSW area of the deposit were also used to establish mass balance calculations (**group 2)**: MD431-121.7, MD430.127.7 and MD430-126, characterized by increasing hydrothermal alteration, and showing dissemination of pyrite, chloritization, weak silicification and scarse *Qz+Chl+Py±Ccp±Sph* veins.

The use of Zr and Ti in the calculations of the f factor provided similar results, with some variations, especially in the case of the sample MD-P3-1-1, belonging to the first group. In the other samples, the calculations are consistent. It is also important to note that the use of Zr, for the f factor calculations, result in higher values (losses or gains) than when TiO_2 is used with the same aim. Thus, the following reported values refer only to the results obtained while using Zr:

Although the following calculations relate only to the mass exchanges associated to the hydrothermal alteration, it is possible to infer on the volume changes, associated to the hydrothermal alteration, based on the obtained f factor. Overall, for the samples that exhibit a less intense hydrothermal alteration, from group 1 and group 2, the f factor indicates volume loss (f= ~0.5-0.8), possibly related to the chloritization processes, and to the leaching of mobile elements, while the samples from these two groups that exhibit a more intense and pervasive hydrothermal alteration are characterized by volume increases (f= 1.3; 1.4; the sample MD-P2-4-1 exhibits a f of 12), related to the silicification processes

and, especially valid for MD-P2-4-1, related to the fracturing and brecciation episodes, with hydrothermal infills.

Considering the samples from the SSW part of the deposit (group 2), mass calculations were used to quantify the hydrothermal alteration elemental exchanges that occurred during hydrothermal alteration (Figure IV.18 (I) [A]). Overall, these rocks record loss of Na_2O, K_2O, MnO and SiO_2 gains, while the sample MD431-121.7 shows SiO_2 loss, of around 9.8-6.62 *wt%*. For the least hydrothermally altered rocks, MgO, CaO, Al_2O_3 and Fe_2O_3 are lost, whereas the sample with the strongest hydrothermal alteration evidences show significant gains for the same elements, around 5-7 *wt%*. All samples are enriched in Cu around 100-156 ppm, the one with more intense hydrothermal alteration further showing Zn gains, with a magnitude order in the tens of ppm. Other trace elements show relatively small negatives mass balances, such as Sc, Ni, Rb, Cr and Sr. Others, such as Co, show depletions in the least hydrothermally altered sample of approximately 4-6 ppm but mass gains characterize the other two.

As for the open pit samples (Figure IV.18 [B]), the two samples characterized by weak silicification, show very similar negative mass balances, characterized by losses in Na_2O, MgO, Al_2O_3, SiO_2, CaO, MnO and Fe_2O_3, up to 11 *wt%*. Both samples are found to have considerable gains (tens to hundreds of ppm) in Zn, as well as As and Pb. Sample MD-P2-9-1 shows a small decrease in Cu, whereas MD-P2-8-1 is characterized by positive Cu mass balance (≈ 110ppm). These two samples also show depletion for Ba. For the rest of the trace elements (*e.g.* Sr, Ba, Bi) the mass balance is, overall, negative. The samples which show a more intense hydrothermal alteration (MD-P3-1-1 and MD-P2-4-1) show variable results: regarding the sample MD-P3-1-1, the mass balance results differed when using Zr or TiO_2. Using Zr, the mass balance result in losses in Na_2O, CaO, up to 4%, in Cr, Ba, as well as Sr and Rb. Such mass balances are also responsible for gains in MgO ≈ 10 *wt%*, Al_2O_3 ≈ 19 *wt%*, SiO_2 ≈ 46 *wt%*, Fe_2O_3 ≈ 6 *wt%*. These are accompanied by additions in Cu ≈ 0.1 *wt%*, Zn ≈ 0.05 *wt%*, V ≈ 275 ppm and small gains (up to dozens of ppm) in Y, Ge, Nb, Ni and Ag. However, for the same sample, when TiO_2 is used in the calculations, the resulting mass balance calculations are different: Na_2O depletion is of the same magnitude (≈ 2%), which is also valid for MgO (≈ 1.8 *wt%*) and K_2O (≈ 0.6 *wt%*), but additional depletions are also evidenced, in Al_2O_3 ≈ 2.9 *wt%*, SiO_2 ≈ 19 *wt%* and Fe_2O_3 ≈ 5 *wt%*. Cu and Zn additions are lower than those obtained using Zr (≈ 317 and 133 ppm, respectively), with comparable Cr, Sr and Ba mass losses. Finally, for the most altered sample (MD-P2-4-1), the calculated mass balances are characterized by considerable additions in SiO_2, Al_2O_3, MnO, Fe_2O_3. This sample is also characterized by significant gains in Cu (11 *wt%*) and Zn (0.15 *wt%*), as well as increases in As (0.3 *wt%*), V, Co, Pb, Sr and Ba (hundreds to thousand ppm), In, Sn, Tl and Cd (tens of ppm).

These mass balances results represent heterogeneous alteration processes: while the majority of the negative mass balances can be explained by the breakdown of primary igneous phases and generation of secondary minerals, such as phyllosilicates, carbonates, epidote and/or titanite, the mass gains associated to hydrothermal activity are restricted to samples where the hydrothermal alteration is more intense. In hydrothermally altered samples, the gains in Fe are generally accompanied by conspicuous additions in Mg, representing the formation of secondary phyllosilicates or the influence of diluted hydrothermal fluids, possibly result of mixtures between ascending hydrothermal fluids and sea-water. This Fe and Mg addition is only absent in MD-P2-4-1, which represents an area adjacent to the mineralization, where gains in Si and Fe, associated to high Cu, Zn, As, Sr and Ba mass increases, are not accompanied by Mg, reveal the influence of non-diluted, metal-rich, hydrothermal fluids. The additions of calcophile elements such as In, Cd and Sn, for more intense hydrothermal altered samples may also reinforce the possibility of a late-stage magmatic input for the hydrothermal fluids. Additionally, there are no litogeochemistry data for basaltic samples affected by the hematite impregnation, associated to the jaspers and umbers deposition (see Chapter IV.1). Based on the petrographic evidences, this low-temperature exhalative hydrothermal episode is most likely characterized by positive mass balances, with considerable gains of Fe±Mn, as well as Mg, Ca, associated to the precipitation of chlorite and carbonates, respectively.

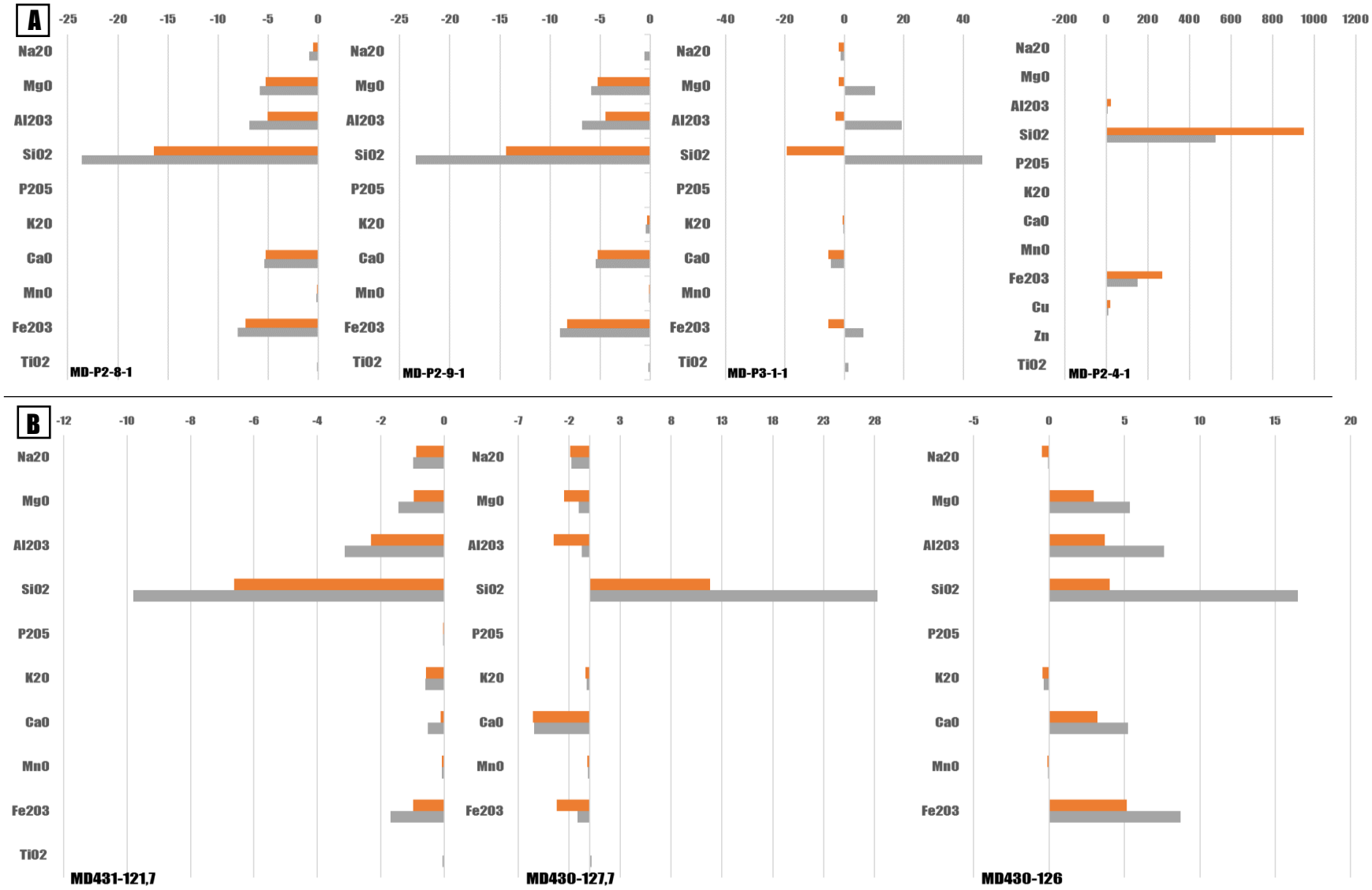

Figure IV.18- Mass balance losses and gains, regarding major elements in wt%, for [A] first group (open pit samples) and [B] second group (SW distal samples). The orange bars were calculated using TiO_2, when calculating the f factor, while the grey represents the mass balance calculations using Zr for the f factor determination.

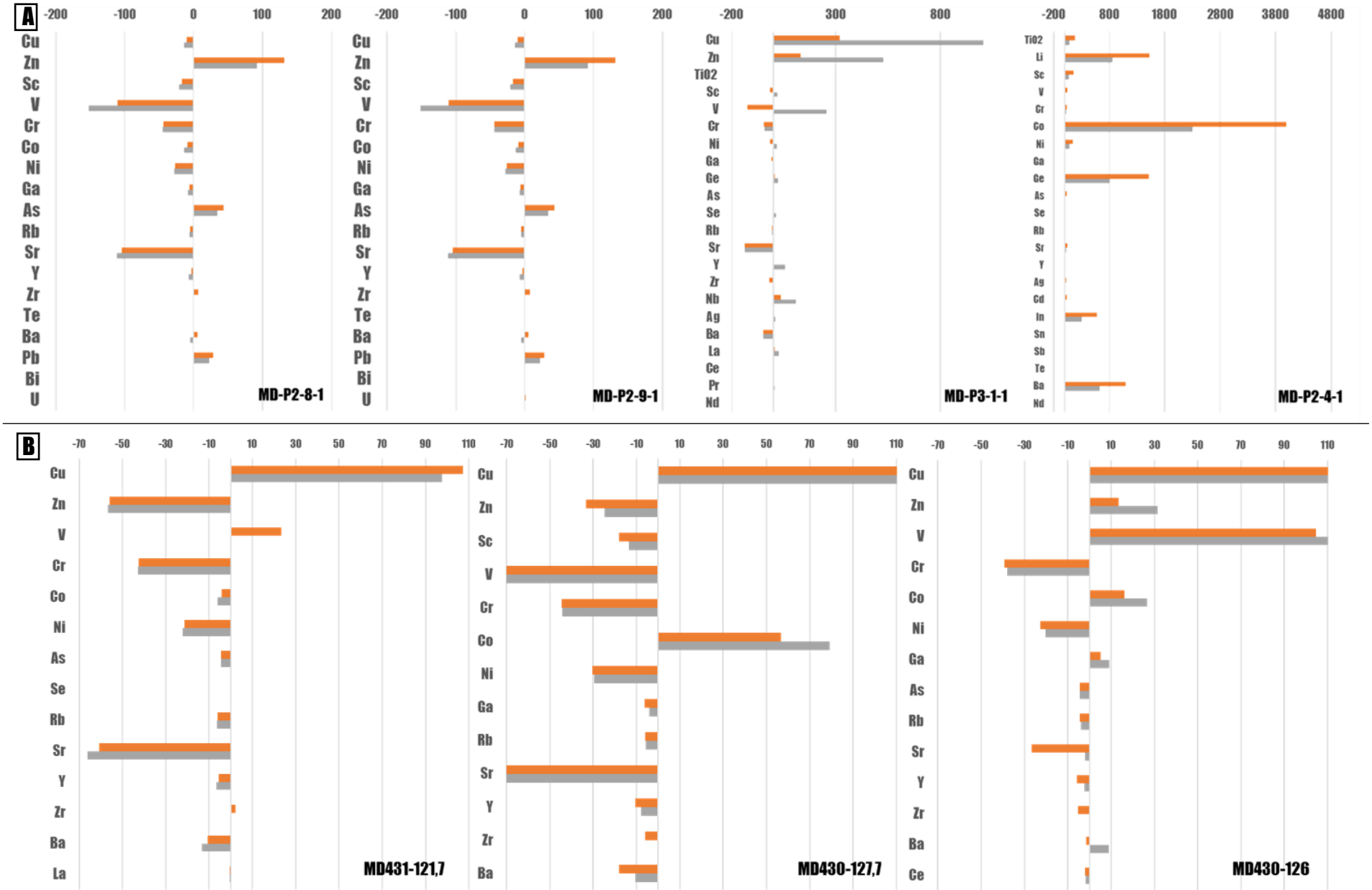

Figure IV.18- Mass balance losses and gains, regarding major elements in wt%, for [A] first group (open pit samples) and [B] second group (SW distal samples). The orange bars were calculated using TiO_2, when calculating the f factor, while the grey represents the mass balance calculations using Zr for the f factor determination.

I.V.3.6. COMPOSITIONAL CLASSIFICATION, VOLCANOSTRATIGRAPHY AND TECTONIC SETTING

Several classical geochemical diagrams can be used both for classification of volcanic rocks and for discriminating geotectonic eruptive settings. The total alkali-silica (TAS) diagram, distributes volcanic rocks into 15 different compositional fields, from primitive to more evolved and discriminates alkalik and sub-akalic series., using the total silica and alkali content (SiO_2 vs $Na_2O + K_2O$) (LeBas, 1986). The application of the TAS diagram is thought to be inefficient for the classification of highly hydrothermally altered or metamorphosed volcanic rocks as it is based on a set of elements which are mobile during such processes. Hence, a series of similar diagrams, especially useful for altered volcanic rocks were developed, using immobile elements as proxies for the classification. The adaptation of Floyd & Winchester's diagram (Floyd & Winchester 1977) proposed by Pearce (1996) remains one of the most widely used tools, using the the Zr/Ti ratio as a measure of the primitive character of volcanic rocks (basic *vs* acid) and Nb/Y to distinguish between tholeiitic *vs* alkalic affinities. In the TAS diagram (Figure IV.19) most of the samples fall within the **basalt, basaltic andesite** or **andesite** fields, the dispersion probably resuting from the alteration procsses rather than from magmatic differentiation. Here, the term "andesite" has been applied to rocks of intermediate composition, and not used in its more usual petrogenetic meaning of rocks related to active oceanic-continental margins, which is not the case of the Sumail ophiolite. For the Zr/Ti *vs* Nb/Y plot, the samples fall within the **basalt** and **alkali basalt** fields. The samples falling within the **alkali basalt** field show more intense hydrothermal alteration which is consistent with the previously shown minor mobility of some of these elements (Nb, Y) under extreme hydrothermal alteration (see Chapter IV.3.4). Hence, it is possible to infer that the volcanic rocks that host the Mandoos deposit are basic to intermediate, basaltic rocks, with tholeiitic affinities (Figure IV. 19 [C] and [D]).

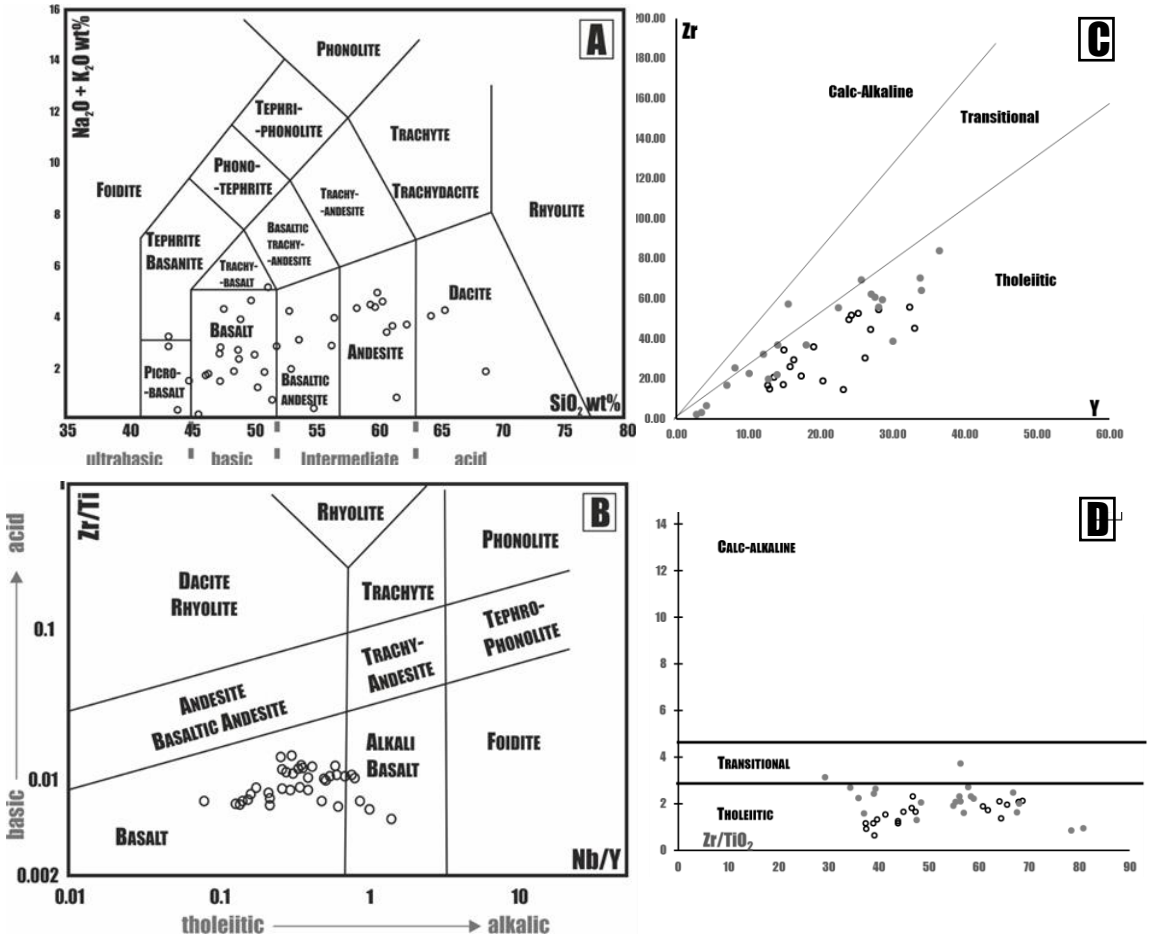

Figure IV.19- [A] TAS diagram (LeBas *et al.*, 1986) with projected data for the hanging-wall and footwall volcanic rocks; **[B]** Zr/Ti *vs* Nb/Y plot, for compositional classification of volcanic rocks (Pearce, 1996); **[C]** Y *vs* Zr plot, to discriminate magmatic affinities, from Ross & Bédard (299) after Barret & MacLean (1999); **[D]** magmatic affinities pinpoint plot, using Zr/TiO_2 *vs* Zr/Y, following Barret & MacLean (1994)

Trace-element and/or immobile element criteria have sometimes been used to distinguish the different volcanic units of the Sumail ophiolite. Besides the C1-normalized REE patterns and incompatible elements ("spider diagrams"), HSFE ratios, such as the Zr/Hf or Nb/Ta ratios, are found to be useful (*e.g.* Godard *et al.*, 2003 2006) (Figure IV.20). Some alternative methods to distinguish volcanic units, namely those based on clinopyroxene chemistry (*e.g.* Ishikawa *et al.*, 2002; Kusano *et al.*, 2012; Gilgen *et al.*, 2014) have been proved unreliable by published data.

Table IV.3- Nb/Ta and Zr/Hf ratios for the hanging and footwall rocks and the ranges of these ratios for the volcanic units.

Hanging-wall					
n= 19	Average	Median	Std-Dev	Minimum	Maximum
Nb/Ta	14.0348	13.9672	0.6439	12.8421	15.2143
Zr/Hf	28.9275	29.3915	1.6473	25.9123	30.5899
Footwall					
n= 22	Average	Median	Std-Dev	Minimum	Maximum
Nb/Ta	14.4379	14.4495	0.3226	14.0238	14.9661
Zr/Hf	31.8646	32.7579	2.7396	25.7777	35.8888

	Zr/Hf	Nb/Ta
Geotimes	33.15-38.7	12.5-14
Lasail	23.6-30.5	12.35-14.4
Alley		10.53-11.65

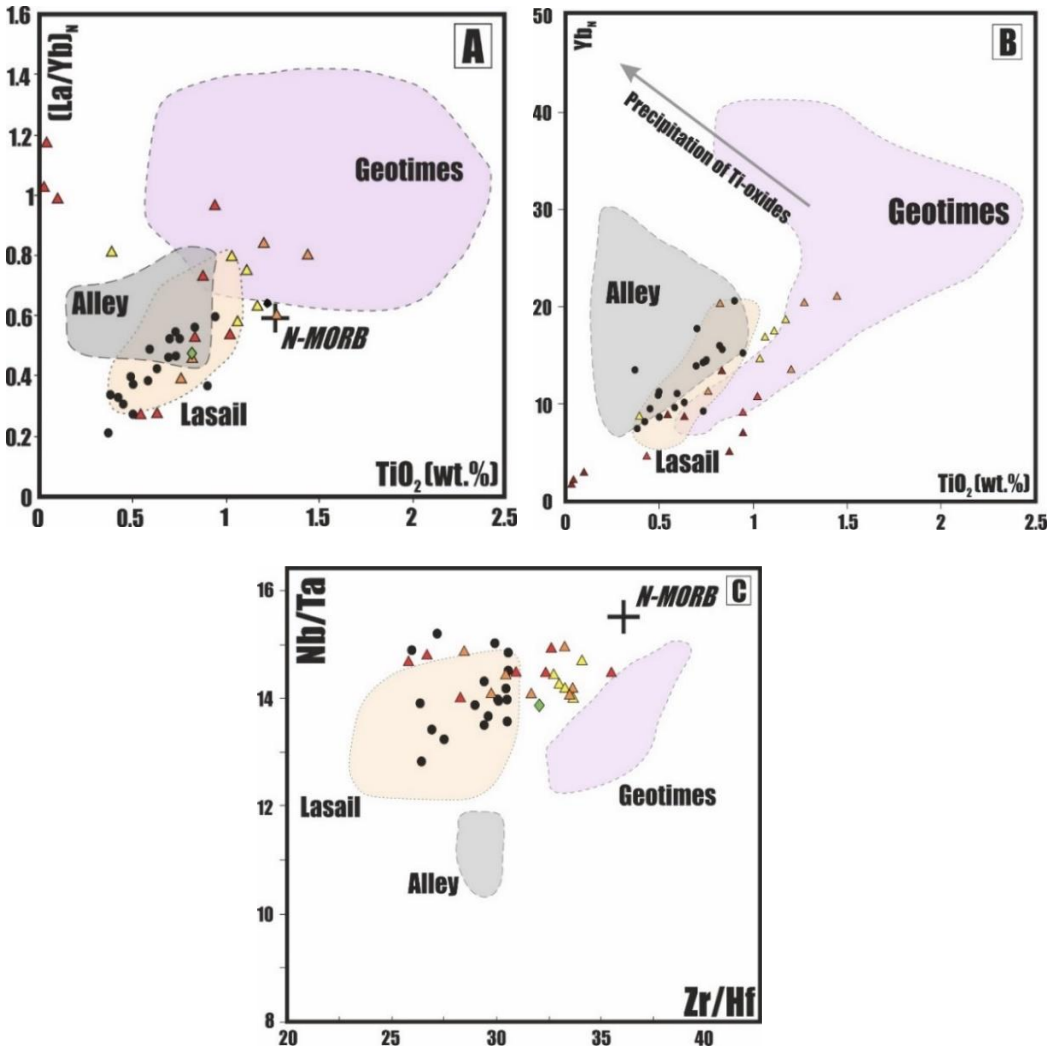

Figure IV.20- [A] $(La/Yb)_{C1N}$ *vs* TiO_2 plot; **[B]** Yb_N *vs* TiO_2; **[C]** Nb/Ta *vs* Zr/Hf plot . Adaptated from Godard *et al.*, (2006); Shaded areas represent the main volcanic units in the Sumail ophiolite (Godard et al., 2003, 2006; Kusano et a., 2012): Geotimes (purple), Lasail (orange); Alley (dark grey). Black circles represent hanging-wall samples and triangles stand for footwall volcanic rocks; their color is related to their degree of alteration.

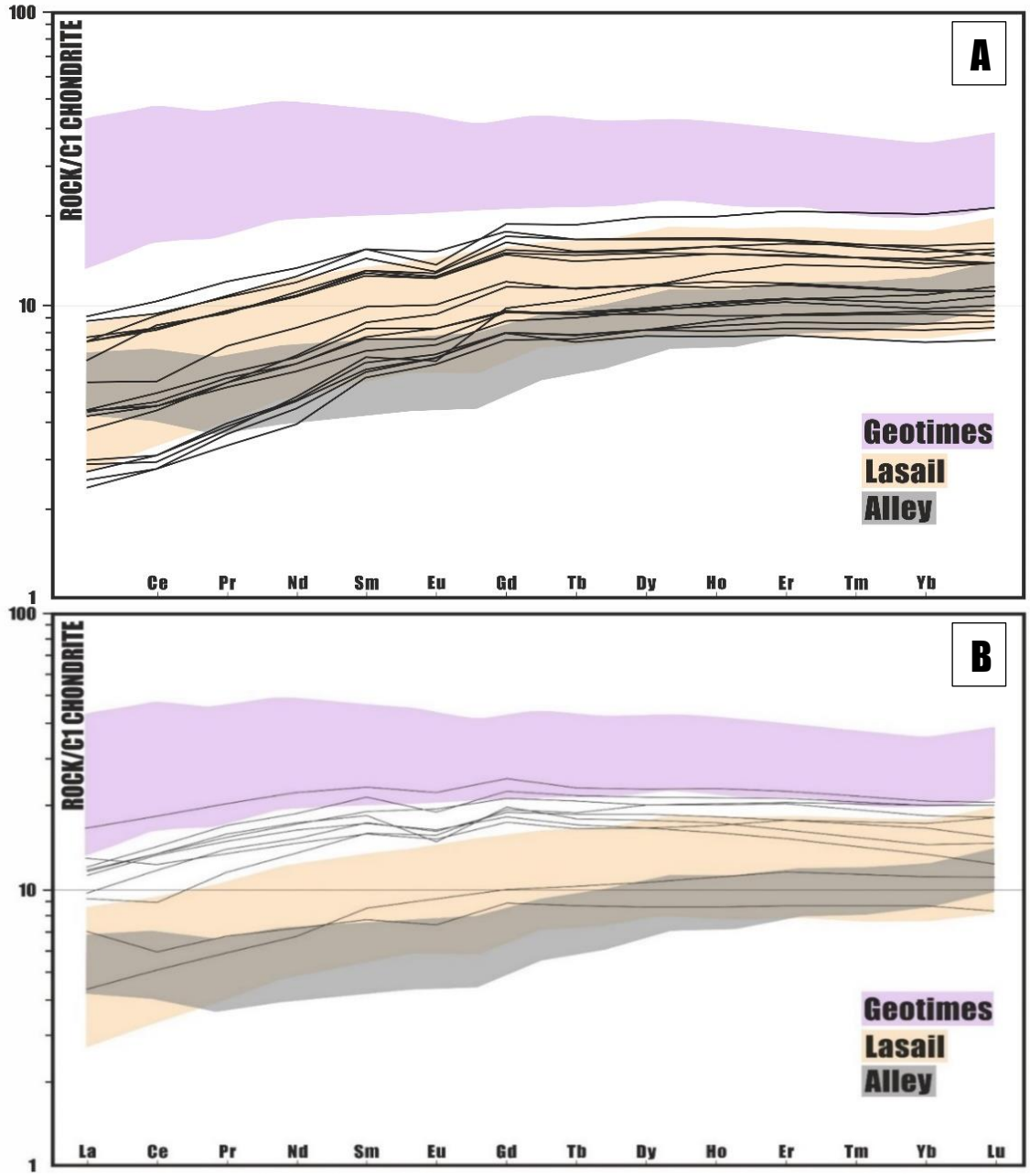

Figure IV.21- C1-normalized REE distributions, [A] for hanging-wall rocks and [B] for footwall rocks; most hydrothermally altered samples (part of the third group) weren't compared. Shaded areas represent the REE patterns for the three main volcanic units found in the Sumail, using published data from: Godard *et al.*, (2003, 2006), Kusano *et al.*, (2012), Gilgen *et al.*, (2016).

Using some of these plots (Figure IV.20 & IV.21), the hanging-wall and some of the footwall samples fall within the Lasail field; additionally, some dispersion is observed for the footwall volcanic rocks which exhibit less intense hydrothermal alteration processes. Furthermore, the HSFE ratios (Table IV.3), the REE patterns and the Nb and Ta concentrations (section IV.3.2) of the hanging-wall basaltic rocks are also consistent with those described for the Lasail unit (Godard *et al.*, 2003, 2006; Kusano *et al*., 2012). Despite some differences in their REE patterns, the average HSFE ratios of the footwall and hanging-wall volcanic rocks are rather similar. The differences possibly result from the more intense alteration processes in these rocks, and it will be discussed ahead, especially for the REE patterns (see Chapter V). Thus, considering the HSFE ratios and, especially the REE patterns, both the hanging and footwall volcanic rocks are attributed to the **Lasail** volcanic unit.

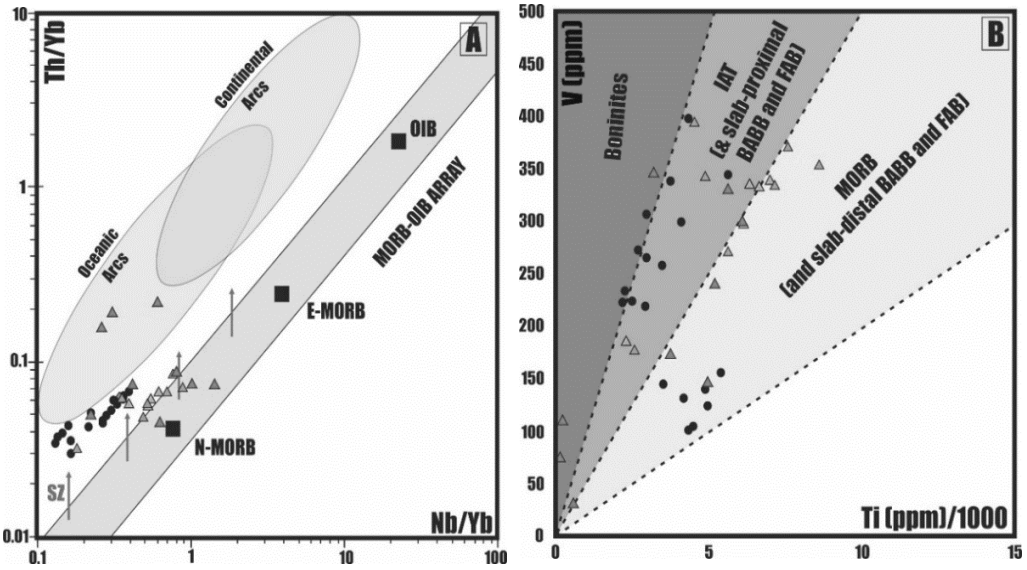

Figure IV.22- Discriminant diagram used to fingerprint the tectonic settings of ophiolites: **[A]** Th/Yb *vs* Nb/Yb, from Pearce *et al*. (2008); **[B]** V *vs* Ti/1000 plot, from Pearce *et al.*, (2008). Black circles represent hanging-wall samples, while triangles stand for footwall volcanic rocks.

The use of Th/Nb and V/Ti ratios (Pearce, 2014) in the Th/Yb *vs* Nb/Yb, V *vs* Ti plots are useful to discriminate the possible tectonic settings of ophiolites, particularly SSZ ophiolites (*e.g.* Pearce, 2008, 2014). The first plot (Th/Yb *vs* Nb/Yb) is based on Th and Nb incompatibility and their distinct mobility during metassomatism. Since Th is mobile during the dehydration of the subducting slab, but Nb is not, suprasubduction lavas are characterized by higher Th values, in comparison to Nb (Pearce *et al.*, 2008). The second plot (V *vs* Ti), from Shervais (1982) is based on the difference in the Ti and V contents and relies on their incompatibility: in water-induced partial melting, magmas are richer in V and have lower Ti contents. In Figure IV.22 [A], both the hanging and footwall rocks that host the Mandoos deposit are found to have higher Th/Yb values compared to MORB, possibly indicating a modification of the mantle source, by subduction-derived fluids. These values are higher for the hanging wall volcanic rocks and present a wider dispersion for the footwall rocks, possibly due to the hydrothermal alteration, during the mineralizing episode(s). This data is also supported by the N-MORB-normalized incompatible elements (Figure IV.23), as these patterns are typically interpreted as characteristic of suprasubduction zones (*e.g.* Saccani *et al*., 2011). Additionally, most of the studied samples fall within the MORB-like and IAT compositional fields, in the V/(Ti/1000) diagram. Despite the general agreement that these plots are useful to fingerprint the tectonic setting of ophiolitic rocks, their interpretation should be cautious, as there are other geochemical and petrological mechanisms that might explain the geochemical features of these rocks, as discussed ahead (see Chapter V).

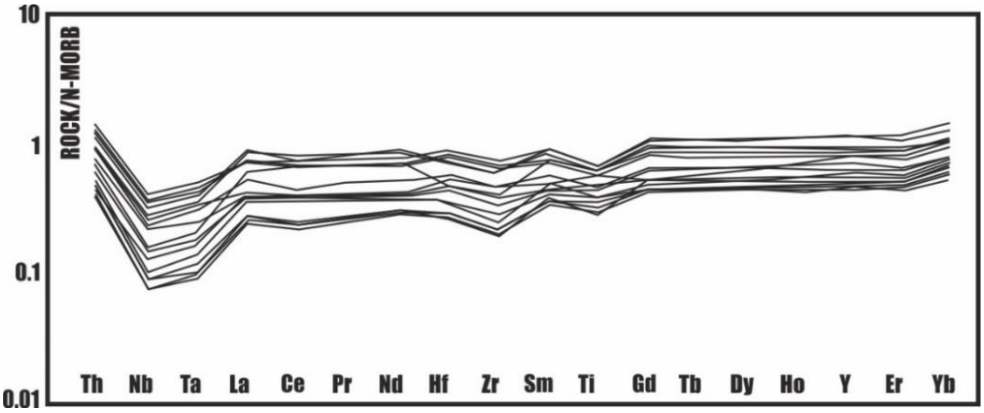

Figure IV.23- N-MORB-normalized multi-elemental diagrams of the hanging and footwall volcanic rocks.

CHAPTER V
DISCUSSION AND CONCLUSIONS

IV.1. DISCUSSION

The volcanic rocks that host the Mandoos VMS deposit occur as microporphyritic massive flows and/or pillow lavas, locally brecciated. Their primary mineralogy is composed of augite and bytownite euhedral microphenocrysts, set in a microlitic matrix composed of bytownite microlites, with similar Ca-rich compositions, with small and sparse, skeletical Ti-rich magnetite grains. All the hanging-wall samples and some footwall rocks show pervasive alteration marked by the breakdown and substitution of the microphenocrysts: the clinopyroxene is altered into a calcic amphibole (actinolite?) and then to a chlorite±epidote assemblage, while plagioclase are partly to completely replaced by albite. The same (partial to complete) substitution is also observed in the plagioclase microlites. The groundmass is composed of phyllosilicates (*Chl-Sme*), that also occur as vesicle infills, as radial aggregates, possibly representing the alteration of a volcanic glassy groundmass. The small skeletical iron oxides often show corroded rims and small titanite crystals in its surroundings. These basaltic rocks are ocasionally, brecciated *in situ*, the fractures acting as channels, increasing the permeability and allowing the circulation of sea water derived fluids, causing the alteration to proceed and the precipitation of microcrystalline quartz and chlorite, with minor carbonates, producing a "breccia-like" texture, with altered basaltic pseudo-clasts, surrounded by a fine-grained matrix. This fragmentation reflects the generation of physical discontinuities, wich enabled fluid circulation, during which late precipitation of quartz and chlorite. The alteration processes resulted in a breccia-like texture, with no jigsaw-fit geometry and/or block rotation, but instead characterized by isolated basaltic pseudo-clasts within the fine-grained pseudo-matrix. Thus, these samples might represent the top of massive flows/pillow-lavas, where the interaction with seawater caused quenching and *in*-situ fracturing, and the consequent increasing permeability favoured fluid circulation.

This pervasive metasomatic alteration is found in all hanging-wall samples and in the footwall samples which show a less intense hydrothermal ore-forming alteration, thus suggesting a widespread regional-scale metasomatic event. Taking the secondary mineral phases into account, it is likely that this stage corresponds to low temperature oceanic metassomatism, caused by sea water, and derived fluids; during this stage, the primary minerals of these volcanic rocks may have acted as a buffer for the chemical reactions, controlling the chemical composition of the secondary mineral phases, and thus metasomatism progressed under low water/rock ratios. Later calcite, calcite + calcic zeolites, formed veins and vesicles infills, possibly marking an increase in the temperature of the system.

Low-temperature exhalative hydrothermal episodes are also identified, and in some cases, preceeded the ore-forming hydrothermal episode. This stage is marked by hematite + carbonates + chlorite veins, by local hematite impregnations and by the formation of jaspers and umbers. While the jaspers/umbers are mostly found in specific areas (E, SE area, and locally in the open pit), the hematite-bearing veins are found throughout the volcanic sequence. It is likely that the formation of these silica and hematite (and Mn)-rich exhalative rocks is structurally-controlled, involving the circulation of Fe(±Mn)-rich and

sulphur-poor, siliceous and oxidizing hydrothermal fluids. These are later crosscut by calcite veins, in the hanging wall sequence, and by *Qz+Py* and *Cal+Py* veins in the footwall rocks. In some cases, hematite-silica veins are found cutting the hydrothermally altered rocks. This indicates that temperature decrease, during the final waning-stage of the hydrothermal system, triggered the development of another exhalative low-T hydrothermal episode.

The hydrothermal stage related to the mineralization event, is recorded by a set of quartz veins, with pyrite, chalcopyrite, and minor sphalerite and apatite disseminations; in certain areas of the deposit (central part, near the open pit), the hydrothermal alteration is marked by silicification, accompanied by pyrite dissemination and, in other cases (drill-core samples), by more intense chloritization pyrite dissemination with quartz, pyrite ± chalcopyrite veins. This difference is possibly a consequence of i) abundant vesicles promoting the circulation of hydrothermal fluids and leading to more pervasive and intense of alteration (*e.g.* open pit area) and; ii) secondary permeability due to the «network of fractures and veins which form the stockwork and enabled more focussed fluid-flow. Additionally, the existence of footwall samples that do not show evidences of hydrothermal alteration also supports the structural control on the development of this hydrothermal system, representing samples which were not cut by the structures that channeled the hydrothermal fluids and, consequently, were not pervasively altered by their circulation. The development of such fracture(s) and vein(s) network is related to hydraulic fracturing, associated to the circulation of the mineralizing fluids.

Zeolites are also found in the footwall volcanic rocks. In some cases, they occur within veins, which are later crosscut by microcrystalline quartz veins; they fill the vesicles in weak to moderately hydrothermally altered rock (from the open pit), and they are also found filling open spaces in the massive sulphide which show typical primary textures found in black-smokers-type vents. This indicates that during the hydrothermal circulation, zeolites precipitated directly from a more alkaline hydrothermal fluid, possibly during the late stages of the hydrothermal fluid circulation, denoting a possible mixture or increase in the sea-water derived component of the hydrothermal fluid, coeval to the reopening of some hydrothermal veins and calcitic Cb + *Py* precipitation, as previously described (see Chapter IV.1, Figure IV.3). Despite the difficulties in adjusting the analysed minerals to any calcic zeolite stoichiometry, some analysis made in the samples collected at the open pit resemble laumontite and (Ca-) epistilbite. These zeolites have been described in present day and fossil mineralised hydrothermal/geothermal systems, *e.g.* Iceland and Troodos ophiolite (Marosvölgyi *et al.*, 2010; Dill *et al.*, 2007), where the temperature record was below 200-250ºC.

The presence of the aluminium-rich phyllosilicates (kaolinite, halloysite, donbassite?) in the open-pit samples, combined in association with more intense hydrothermal alteration (silicification and pyritization) reinforces the idea that these rocks experienced a more intense and pervasive leaching and hydrothermal alteration process under strong acid conditions.

Less vesicular volcanic rocks, further from the open pit (and possibly from structural discontinuities), exhibit less pervasive alteration, with occasional quartz, chlorite and pyrite ± chalcopyrite veins, in a mildly silicified matrix, with more intense chloritization and pyrite dissemination. Despite this, most of the samples from the footwall volcanic sequence were retrieved relatively far from the area where the hydrothermal activity was more intense and focalized, while some of the samples that show a more intense hydrothermal alteration came from the open pit, where the sulphide lens was thickest (thus, sampling the basaltic rocks that were most affected by the hydrothermal processes related to the mineralization).

The intermittence of volcanic eruptions and the residual heat from sub-volcanic intrusions have sustained hydrothermal activity, which consisted of: i) exhalative, low-temperature hydrothermal episodes, characterized by hematite veins and deposition of jaspers and umbers; and ii) a ore-forming hydrothermal system, with development of a network of crack-and-seal veins and veinlets, where sulphides (pyrite, chalcopyrite and minor sphalerite) precipitated, together with quartz, chlorite and accessory apatite, in a stockwork-like arrangement with an intensely silicified zone; *Py*, *Cpy* and *Sph*, disseminations formed close to the massive sulphide mineralization, and late Zeol and *Cal+Py* veins sometimes re-open previous structures. In extreme cases (such as the sample MD-P2-4-1), the hydrothermal ore-forming processes resulted in pervasive pyrite (with minor chalcopyrite and sphalerite) and quartz replacements, with intense brecciation and hydrothermal (*Qz+Py±Ccp*) precipitates, leaving only chlorite+quartz rich cores, remnants of the intensely replaced basaltic rocks. This suggests that the mineralizing system developed, as well, in sub-superficial conditions, as sub-sea floor replacements. This process can also be promoted by the presence of pre-existent discontinuities, such as the ones described for the *in situ* fragmentation, in the hanging-wall sequence.

The spatial distribution of these hydrothermal alteration facies is structurally controlled, but variations in the amount and distribution of vesicles, determined the volcanic rocks primary permeability, also influencing the circulation of the hydrothermal fluids. In order to fully characterise the distribution of the hydrothermal alteration haloes a more comprehensive sampling would be necessary

Evidences of widespread low-temperature alteration (oceanic metassomatism) followed by temperature increase (hematite veins and jaspers formation) in the hanging and footwall rocks supports a multi stage cyclical evolution of the system, having common heat-sources (such as sub-volcanic intrusions) wich favoured the recurrence of similar processes in different time-periods, before and after the mineralization processes took place.

The hydrothermal fluids involved in the mineralization are nonoxidizing, siliceous fluids, probably sea-water derived, which scavenged metals from the underlying volcanic and hypabyssal rocks. During fluid circulation, the fluid-chemistry controlled the progression of the mineralogical transformations at high water/rock ratios, also supported by the intense quartz and chlorite alteration in the open pit samples (Hannington, 2014). According to the chlorite-based geothermometers of Jowett (1991) and Bourdelle *et al.*, (2009), mineralizing fluids would have circulated at temperatures between ~200-430ºC (median T ~275ºC). This temperature range is provided for the overall hydrothermal mineralising stage, since it was not possible to differentiate to which of the episodes the analysed chlorites belonged to. These temperatures were obtained using samples from the more distal SSE part of the deposit. Thus, it is admissible that these temperatures are lower than those expected for chlorites from the stockwork directly below the open-pit area, where the hydrothermal system was more vigorous.

Additionally, the presence of small crystals of fluorapatite related to the hydrothermal alteration and mineralization, possibly indicates: I) the leaching of P from overlying pelagic organic matter-rich sediments; or II) an input of late-stage magmatic fluids/volatiles for the hydrothermal fluids (P and F), related to the crystallization of the doleritic rocks, since *Ap* is also found in these rocks; such crystals result precipitate directly from exsolved late-magmatic, volatile-rich (*e.g.* F) fluids, also responsible for the presence of small, disseminated, sulphides.

The rocks that host the Mandoos deposit record several mineralogical transformations and major and trace-element compositional modifications, caused by the different interpreted alteration events. During such alteration events, elements like Zr, Ti, Hf, show an immobile behaviour, while elements such as Al, Nb, Ta, Y or Yb are found to be slightly mobile, under specific conditions. These alteration

evidences, during the different distinguished stages, are expressed in the mineralogical transformations observed and can be quantified through mass balance calculations.

The application of the alteration box-plot proposed by Large *et al.* (2001) based on whole rock geochemical data, corroborates the mineralogical transformations and the precipitation of secondary mineral phases, observed in the studied rocks especially those affected by the mineralising hydrothermal alteration event. The hanging-wall rocks follow a regional/diagenetic alteration trends wherein the formation of a secondary k-feldspars+albite mineral association is predicted. However, K-feldspar is not observed in the studied samples and instead, secondary K-bearing phyllosilicates are formed. Finally, the use of AI_{major} and AI_{trace}, proposed by Häussinger (1993), allowed a clear the distinction between hydrothermally altered samples, associated to mineralizing hydrothermal activity and regional metasomatic alteration.

Mass balance calculations were not possible for the initial metasomatic alteration event due to lack of samples without this alteration imprint. Nevertheless, through the analysis of the major and trace element data, it is possible to infer that oceanic metasomatism led mainly to negative mass balances, characterized by a high mobility of elements like K, Na, Ca, Rb, Sr, U, in spite of the mass gains, result of the veins sealing and vesicles infills by secondary mineral phases. This sea-water induced regional alteration is, possibly, also responsible for the observable negative Ce anomalies in the hanging and footwall lavas, as these fluids are typically characterized by such anomalies. For the low-temperature, exhalative hydrothermal alteration, mass balances were also not calculated, due to the inexistence of litogeochemical data for volcanic rocks that are only affected by this alteration processes. Nevertheless, considering the petrographic analysis and interpretation and the other products of these exhalative processes (formation of jaspers and umbers), it is possible to infer positive mass balances, with net gains in Fe ± Mn, Ca, Mg and possibly in P and other elements, such as As or Pb.

The mass balances, calculated for the hydrothermal alteration, conspicuous of the ore-forming stage, are characterized by overall negative balances, with some exceptions regarding the samples recording more intense hydrothermal alteration. The breakdown of primary mineral phases and the formation of secondary mineral phases resulted in depletion in Si and other elements such as Ca or Mg, generally accompanied by losses in Si. These hydrothermal alteration haloes are further characterized by Fe additions, followed by mass gains in Mg and significant Zn and Cu; these may account for more diluted hydrothermal fluids, possibly related to sea water infiltration and mixture. Nevertheless, in the open pit samples, where the mineralization is more developed, the results show additions in Si and Fe, as well as Cu, Zn, As, Ba and lower or negative mass balances of Mg, revealing the input of non-diluted, hydrothermal, metal-rich fluids. The In and Sn, Tl and Cd gains, in the most intensily mineralized samples, can also support the possibility of a late-stage magmatic fluid input in the hydrothermal fluids, since these elements are usually associated with (late-stage) exsolved magmatic fluids.

These mineralogical transformation and textural features, as well as the lithogeochemical data, are compatible with previously described hydrothermal alteration haloes, in mafic-hosted VMS deposits. The intense silicification and the dissemination of pyrite, in the vicinity of the massive sulphide body (open pit samples), is well documented within the literature (*e.g.* Galley and Koski, 1999; Franklin *et* al., 2005; Galley *et al*., 2007; Hannington, 2014; "Quartz-Pyrite stockwork), where Si precipitates directly from the hydrothermal fluids, possibly from the rapid cooling of the hydrothermal fluids. The chloritization and pyrite dissemination, found in the SE drill-core samples, is also commonly described within the literature (*e.g.* Galley and Koski, 1999; Franklin *et* al., 2005; Galley *et al*., 2007), corresponding, usually, to the lower-temperature, stockwork-related alteration.

Finally, petrogenetic and volcanostratigraphic significance the volcanic rocks are discussed. The comparison of their geochemical features (REE bulk contents, their LREE depleted and HREE flat-segment, incompatible element ratios, and incompatible elements trace contents), with published data for the ophiolite volcanic units strongly suggests that the volcanic rocks that host the Mandoos deposit are part of the Lasail volcanic unit. The more enriched REE patterns of the footwall volcanic rocks (Figure IV.15) can be explained by apparent gains during alteration processes and the neoformation of secondary mineral phases that retain these elements in their mineral structure. Nevertheless, such differences can also be interpreted as resulting from magmatic differentiation; in this situation, these features could indicate a transition from the more evolved, REE enriched Geotimes volcanism to more primitive, REE depleted Lasail rocks, as previously documented in the literature (Godard *et al*., 2006). In this case, these footwall lavas can still be attributed to the Lasail unit, mostly based on their HSFE ratio, but would represent a transitional volcanism, between the two volcanic units.

The REE ratios (La_N/Sm_N, La_N/Yb_N), N-MORB-normalized patterns (Figure IV. 20), especially their Ti contents and their Nb depletion and high Th contents of the volcanic rocks hosting the Mandoos deposit are compatible with the Medium Titanium Basalts (MTB), as defined by Saccani *et al.*, (2011), and also with other interpretations for similar volcanic rocks (Saccani *et al*., 2011 and references therein). These authors suggest that MTB rocks originated from partial melting of a more refractory mantle source than that associated with typical MORB; such source could be a SSZ mantle wedge which underwent 8-10% of partial melting after a first MORB-melt extraction. They also interpreted the LREE depletion of the MTB's as an evidence that the subduction related fluid-induced partial-melting was not responsible for significant enrichments of the SSZ mantle wedge. The V2 volcanic sequence of the Sumail ophiolite (Alley. followed by boninites has been interpreted as being generated in a SSZ setting, associated to the interpreted intra oceanic thrusting, followed by dehydration and consequent metasomatic modification of the mantle source (*e.g.* Searl, 2007). The lower Geotimes unit, thought to have erupted in a MOR-setting, was targeted in recent studies (MacLeod *et al.*, 2013), where it was concluded that the water content involved in its fractionation is not consistent with an eruption in a MOR setting, instead, the geotectonic setting was interpreted as a back-arc basin. Indeed, the geochemical compositions of the Geotimes and Lasail rocks are consistent with those found on back-arc basins, distant from subduction zones (*e.g.* Lau-basin or North Fiji Basin; Godard *et al.*, 2006 and references therein; see Figure IV.15). While the Alley unit is considered to have a clear arc/SSZ signature, some authors suggest that Lasail volcanic rocks also bear the same geochemical signature (*e.g.* Searl, 2007).

Godard *et al.* (2006) interpreted the LREE depletion, the lower incompatible element abundances (except for mobile elements such as Rb, Sr), such as Ta, Nb, Ti, and the Nd, Pb and Sr isotopic composition for the Lasail unit as the result of a later partial melting from the same mantle source as Geotimes (DMM), the Sumail peridotites, which underwent high degrees of melt extraction (15-30%). This later partial melting, that originated the depleted Lasail volcanics, would have involved the mixture between high-degree fractional melting (25%) of DMM and a small fraction of melt (2%) in equilibrium with the peridotitic rocks, resulting in geochemical compositions altogether similar to the ones described for the volcanic rocks that host the Mandoos deposit (Godard et al., 2006). Furthermore, the isotopic compositions of Lasail and Geotimes rocks are similar to those in Geotimes unit: their εNd and Pb isotopic signatures do not resemble any present-day slab-derived contamination setting, eliminating the possibility of these rocks originating in an arc-like setting. Additionally, the mobile elements spectrum, especially the enrichments in Rb, Sr, U and Pb, were explained by pervasive alteration, associated to sea-water and sea-water derived fluids, under low-temperature conditions, similar to the oceanic metasomatic event described in this work (see Chapter IV.3.2.1).

Considering the available published data for the Lasail volcanic unit, especially regarding its isotopic compositions, these low-Ti, LREE depleted basalts possibly erupted in a back-arc basin. These are the result of a later, shallower, high % melting event of a DMM-like source, following an initial lower-degree partial melting (extraction of Geotimes). This volcanic unit (Lasail) is usually considered as part of V2 magmatic stage of the Sumail, for which there is widespread agreement on the arc-affinity/SSZ signature (Figure IV. 22). Additionally, the tholeiitic nature of these rocks excludes any genetic relationship with typical alkaline-affinity off-axis volcanism. Considering the previous discussion, one may suggest that this unit should be attributed to the upper part of the V1 volcanic episode, as it does not seem to result from partial melting of a SSZ-modified mantle source; instead, it is likely that it formed during the latest stages of V1 volcanism, through partial melting of a depleted mantle source, after extraction of the Geotimes basalts, in a ridge-like setting.

IV.2. CONCLUSIONS

The volcanic sequence that host the Mandoos deposit includes basaltic to basalt-andesitic rocks with tholeiitic affinities, and with HSFE ratios and REE patterns characteristic of the Lasail volcanic unit. Those rocks represent the product of late partial melting of a depleted DMM source, during the first volcanic episode (V1), in a ridge-like setting (Godard *et al.,* 2006).

These rocks include pillow-lavas and massive volcanic flows whose texture and mineralogy documents the progression of heterogeneously developed and multi-staged alteration processes triggered by fluid-rock interactions. These processes were locally promoted by physical discontinuities, generated during *in-situ* brecciation processes. Nevertheless, structurally-controlled fractures, related to hydraulic fracturing play an important role in fluid circulation, thus controlling the development of the alteration patterns.

The breakdown of primary igneous phases, *i.e.* clinopyroxene microphenocrysts and magnetite, into *Act+Chl+Ep* and *Ttn*, albitization of the plagioclase microphenocrysts and microlites, and the neoformation of secondary mineral phases, such as carbonates, phyllosilicates (*Chl-Sme* interstratificates) and zeolites, in veins and vesicles, is of pervasive nature. This alteration marks the oceanic metassomatic alteration, also found in the footwall volcanic rocks, also known as spilitization. This process developed in (sub-)superficial conditions, involving sea-water fluids, at low water/rock ratios.

The spatial distribution of the alteration haloes associated with hydrothermal stages is structurally controlled but also related to primary permeability, determined by the amount (and connectivity) of the vesicles: i) the distribution and circulation of low-temperature hydrothermal, siliceous, S-poor and Fe-rich fluids, was responsible for the deposition of jaspers, with hematite impregnations in the underlying basaltic rocks; ii) the main hydrothermal activity is contemporaneous with the sulphide deposition. In the open pit samples, silicification processes are recorded, accompanied by the dissemination of pyrite with occasional chalcopyrite and sphalerite, sometimes preserving remnants of the feldspars microlites, in the rocks matrix. Locally, some *Zeo+Qz* veins cut these hydrothermally altered rocks, possibly developed during the reopening and sealing of a set of *Cb+Py* veins. These zeolite-bearing veins are later re-opened and sealed by microcrystalline *Qz*, suggesting a rapid cooling and also the important structural control on the hydrothermal fluids circulation. Towards the SSE part of the deposit, the hydrothermal alteration is marked by chloritization and pyrite dissemination, accompanied by mild silicification, with occasional *Qz+Chl+Py+Ccp* veins. Here, a strong variation in the alteration is observed: the presence of chloritized volcanic rocks contrasts with mildly silicified, chloritized (and also pyritized) volcanic rocks which essentially exhibits the alteration mineralogical association attributed to

the oceanic metassomatic alteration. Regardless of the differences on the hydrothermal alteration "facies", further sampling (*e.g.* in the stockwork that underlies the massive sulphide lens and from different areas of the open pit, as well as a more detailed mapping of this area) would allow a better understanding of the spatial development and distribution of these haloes. Nevertheless, the recognizable mineralogical and textural alterations are analogous to those described in the literature for the mafic-hosted VMS-type deposits: a highly silicified and pyritized area, beneath the massive sulphide lens (quartz and pyrite stockwork) and the lower-temperature alteration, related to the stockwork that fed the hydrothermal system, characterized by chlorite and pyrite (chlorite-pyrite stockwork).

The hydrothermal fluids responsible for the massive sulphide mineralization are characterized by moderate to high temperatures (195-430ºC), most cerntainly acidic and bearing relatively high metal contents; its chemistry as mostly controlled the chemical reactions that developed the alteration haloes, under high water/rock ratios.

The residual heat derived from the cooling of sub-volcanic intrusions – dolerite dykes – sustained such hydrothermal processes; the presence of small disseminated Ap crystals, as well as sulphides (Py), in the doleritic rocks suggest a small contribution of late-stage magmatic volatiles to the hydrothermal fluid, responsible for the precipitation of accessory apatite in the hydrothermally altered footwall volcanic rocks. This input is probably also responsible for increases in the In, Cd, Tl and Sn contents in the most mineralized samples.

Apart from the pervasive oceanic metasomatism, the similarities between the hanging-wall and footwall rocks imply that similar heat-sources favoured the development of low-temperature hydrothermal processes at different times, explaining the occurrence of jaspers and/or umbers both before and after the main mineralization event, during the waning of the hydrothermal system.

The mineralogical and textural transformations are also evident in the major element geochemistry variations, using the AI and CCPI indexes. These indexes represent lithogeochemical compositional modifications which result in secondary mineral associations characterized by I) Ab+Chl; II) Ab+Chl+Ep; III) Chl+Py; IV) Cb±Ser; V) Chl+Cb. Such compositional modifications are consistent with mass losses, although some major and trace element additions are recorded; these are usually associated with hydrothermal activity, marked by vein- and vesicle-infilling or, during extreme hydrothermal alteration, by sulphide deposition. Furthermore, the AI_{major} and AI_{trace} indices (Häussinger, 1993) successfully discriminate various alteration trends, related or not to ore-forming hydrothermal systems, and rather useful for VMS exploration.

CHAPTER VI
REFERENCES

ALABASTER, T., PEARCE, J.A., MALLICK, D.I.J., AND ELBOUSHI, I.M., 1980, The volcanic stratigraphy and location of massive sulphide deposits in the Oman ophiolite. *In* PANAYIOTOU, A. (eds), *Ophiolites, Proceedings International Ophiolite Symposium*, Cyprus, 1979: Nicosia, The Geological Survey of Cyprus, 751–757.

ALABASTER, T., PEARCE, J.A., MALPAS, J., 1982, The Volcanic Stratigraphy and Petrogenesis of the Oman Ophiolite Complex. *Contributions to Mineralogy and Petrology*, 81, 168-183.

ALABASTER, T., AND PEARCE, J.A., 1985, The interrelationship between magmatic and ore-forming hydrothermal processes in the Oman ophiolite. *Economic Geology*, 80, 1–16.

ALT, J., 1997, Hydrothermal Alteration and Mineralisation of Oceanic Crust: Mineralogy, Geochemistry and Processes, *In* BARRIE, C.T., AND HANNINGTON, M.D. (eds) *Volcanic-Associated Massive Sulphide Deposits: Processes and Examples in Modern and Ancient Settings*. Reviews in Economic Geology, 8, 417p.

ARMBRUSTER, T., AND GUNTHER, M.E., 2001, Crystal structures of natural zeolites. *In* BISH, D.L., MING, D.W. (eds), *Natural Zeolites: Occurrence, Properties, Applications*. Mineralogical Society of America and Geochemical Society, 45, 1-57.

A'SHAIKH, D., MIYASHITA, S., MATSUEDA, H., 2005, The petrological and geochemical characteristics of an ophiolite volcanic suite from the Ghayth area of Oman. *Journal of Mineralogical and Petrological Sciences*, 100, 202-220.

A'SHAIKH, D., MATSUEDA, H., MIZUTA, T., MIYASHITA, S., 2006, Hydrothermal Alteration of Oman Ophiolite Extrusives in Ghuzayn Area. *Resource Geology*, 56(2), 167-182.

BASALTIC VOLCANISM STUDY PROJECT, 1981, *Basaltic Volcanism on the Terrestrial Planets*. Pergamon Press, Inc., 1286 p.

BARRAT, J. A., KELLER, F., AMOSSÉ, J., TAYLOR, R. N., NESBITT, R. W. AND HIRATA, T., 1996, Determination of rare earth elements in sixteen silicate reference samples by ICP-MS after Tm addition and ion exchange separation. *Geostandards Newsletter*, 20(1), 133-139.

BARRAT, J. A., YAMAGUCHI, A., GREENWOOD, R. C., BOHN, M., COTTEN, J., BENOIT, M. AND FRANCHI, I. A., 2007, The Stannern trend eucrites: Contamination of main group eucritic magmas by crustal partial melts. *Geochimica et Cosmochimica Acta*, 71(16), 4108-4124.

BARRET, T.J. & MCLEAN, W.H., 1994, Chemostratigraphy and hydrothermal alteration in exploration for VHMS deposits in greenstones and younger volcanic rocks. *In* LENTZ, D.R. (eds), *Alteration and Alteration Processes associated with Ore-forming Systems*. Geological Association of Canada, Short Course Notes, 11, 433-467.

BARRET, T.J., & MACLEAN, W.H., 1999, Volcanic sequences, litogeochemistry, and hydrothermal alteration in some bimodal volcanic-associated massive sulphide systems. *In* BARRIE, C.T. AND HANNINGTON, M.D. (eds) *Volcanic-Associated Massive Sulphide Deposits: Processes and Examples in Modern and Ancient Settings*. Reviews in Economic Geology, 8, 417 p.

BARRET, T.J., DAWSON, G.L., MACLEAN, W.H., 2008, Volcanic Stratigraphy, Alteration, and Sea-Floor Setting of the Paleozoic Fetais Massive Sulphide Deposit, Aljustrel, Portugal. *Economic Geology*, 103, 215-239.

BARRIE, C.T., HANNINGTION, M.D., 1997, Classification of Volcanic-Associated Massive Sulphide Deposits Based on Host-Rock Composition. Chapter 1 *in* BARRIE, C.T., AND HANNINGTON, M.D., (eds) *Volcanic-Associated Massive Sulphide Deposits: Processes and Examples in Modern and Ancient Settings*. Reviews in Economic Geology, 8, 417 p.

BENNOIT, M., CELEUNEER, G. POLVÉ, M., 1999, The remelting of hydrothermally altered peridotite at mid-ocean ridges by intruding mantle diapirs. *Nature*, 402, 514-518.

BERRA, F., AND ANGIOLINI, L., The evolution of the Tethys region throughout the Phanerozoic: A brief tectonic reconstruction. *In* MARLOW, L., KENDALL, C., AND YOSE, L. (eds), *Petroleum systems of the Tethyan region*, AAPG Memior, 106, 1-27p.

BOUDIER, F., NICOLAS, A., 1985, Harzburgite and lherzolites subtypes in ophiolitic and oceanic environments. *Earth and Planetary Science Letters*, 76, 84-92.

BOUDIER, F. & NICOLAS, A., 1995, Nature of the Moho Transition Zone in the Oman Ophiolite. *Journal of Petrology*, 36(3), 777-796.

BOUDIER, F., NICOLAS, A., ILDEFONSE, B., 1996, Magma chambers in the Oman ophiolite: fed from the top and the bottom. *Earth and Planetary Science Letters*, 144, 239-250.

BOUDIER, F., CEULENEER, G., NICOLAS, A., 1998, Shear zones, thrusts and related magmatism in the Oman ophiolite: initiation of thrusting on an oceanic ridge. *Tectonophysics*, 151, 257-296.

BOUDIER, F., GORDARD, M., ARMBRUSTER, C., 2000, Significance of gabbronorite occurrence in the crustal section of the Sumail ophiolite. *Marine geophysical Researches*, 21, 307-326.

BOURDELLE, F., PARRA, T., BEYSSAC, O., CHOPIN, C., & VIDAL, O., 2013, Clay minerals as geo-thermometer: A comparative study based on high spatial resolution analysis of illite and chlorite in Gulf Coast sandstones (Texas, U.S.A.). *American Mineralogist*, 98, 914-926.

BRETON, J-P., BÉCHENNEC, F., LE MÉTOUR, J., MOEN-MAUREL, L., RAZIN, P., Eoalpine (Cretaceous) evolution of the Oman Tethyan continental margin: insights from a structural field in Jabal Akhdar (Oman Mountains). *GeoArabia*, 9(2), 41-58.

BURG, J.-P., 2015, Oman: An obducting orogen, in: http://www.files.ethz.ch/structuralgeology/JPB/files/English/Omaneng.pdf

CAMPBELL, L.S., CHARNOCK, J., DYER, A., HILLIER, S., CHENERY, S., STOPPA, F., HENDERSON, C.M.B., WALCOTT, R., RUMSEY, M., 2016, Determination of zeolite-group mineral compositions by electron probe microanalysis. *Mineralogical Magazine*, 80(5), 781-807.

CATHELINEAU, M., 1988, Cation site occupancy in chlorites and ilites as a function of temperature. *Clay and Clay Minerals*, 23, 471-485.

CATHELINEAU, M., AND NIEVA, D., 1985, A chlorite solid solution geothermometer: the Los Azufres (Mexico) geothermal system. *Contrib. Mineral. Petrol.*, 91, 235–244.

CODEÇO, M., 2015, *Estudo comparativo das sequências vulcânicas constituintes dos eixos Ervidel-Roxo e Figueirinha-Albernoa (Faixa Piritosa Ibérica) e respectiva relevância na prospecção de sulfuretos maciços polimetálicos.* MSc thesis, Lisbon University, 253pp.

COLEMAN, R.G., 1981, Tectonic Setting for Ophiolite Obduction in Oman. *Journal of geophysical Research*, 48(B4), 2497-2508.

COX, J., 2000, *Subduction-obduction related petrogenetic and metamorphic evolution of the Semail ophiolite section in Oman and the United Arab Emirates.* PhD thesis, University of Oxford, 284pp.

DE CARITAT, P., HUTCHEON, I. AND WALSHE, J.L., 1993, Chlorite geothermometry: a review. Clays and Clay Minerals, 41, 219-239.

DEER, W.A., HOWIE, R.A. AND ZUSSMAN, J., 2008, Introduction to the Rock-forming Minerals. Tradução de C.A.R. Macedo. Fundação Calouste Gulbenkian, 727pp.

DILEK, Y., FURNES, H., 2009, Structure and Geochemistry of the Tethyan ophiolites and their Petrogenesis in subduction rollback systems. *Lithos*, 113, 1-20.

DILEK, Y., FURNES, H., 2011, Ophiolite genesis and global tectonics: Geochemical and tectonic fingerprinting of ancient oceanic lithosphere. *GSA Bulletin*, 123, 387-411.

DILEK, Y., FURNES, H., 2014, Ophiolite and Their Genesis. *Elements*, 10, 93-100.

DILL, H.G., FÜßL, M, BOTZ, R., 2007, Mineralogy and (economic) geology of zeolite-carbonate mineralization in basic igneous rocks of the Troodos Complex, Cyprus. *Neues Jahrbuch für Mineralogie - Abhandlugen*, 183(3), 251-268.

ERNEWEIN, M., PFLUMINO, C., WHITECHURCH, H., 1988, The death of an accretion zone as evidenced by the magmatic history of the Sumail ophiolite (Oman). *Tectonophysics*, 151, 247-274.

FLEET, A.J., & ROBERTSON, A.H.F., 1980, Ocean-ridge metalliferous and pelagic sediments of the Semail Nappe, Oman. *Journal of the Geological Society*, 137, 403-422

FRANKLIN, J.M., SANGSTER, D.M., LYDON, J.W., 1981, Volcanic-Associated Massive Sulphide Deposits. *Economic Geology 75th Anniversary Volume*, 485-627.

FRANKLIN, J.M., GIBSON, H.L., JONASSON, I.R., GALLEY, A.G., 2005, Volcanogenic Massive Sulphides. *Economic Geology 99th Anniversary* Volume, 523-560.

GALLEY, A.G., KOSKI, R.A., 1999, Setting and Characteristics of Ophiolite-Hosted Volcanogenic Massive Sulphide Deposits. Chapter 10 *in* BARRIE, C.T., AND HANNINGTON, M.D., (eds), *Volcanic-Associated Massive Sulphide Deposits: Processes and Examples in Modern and Ancient Settings*. Reviews in Economic Geology, 8, 417 p.

GALLEY, A.G., HANNINGTON, M.D., AND JONASSON, I.R., 2007, Volcanogenic massive sulphide deposits. *In* GOODFELLOW, W.D. (eds) *Mineral Deposits of Canada: A Synthesis of Major Deposit-Types, District Metallogeny, the Evolution of Geological Provinces, and Exploration Methods.* Geological Association of Canada, Mineral Deposits Division, Special Publication No. 5, 141-161.

GILGEN, S.A., DIAMOND, L.W., MERCOLLI, I., AL-TOBI, K., MAIDMENT, D.W., CLOSE, R., AL-TOWAYA, A., 2014, Volcanostratigraphic Controls on the Occurrence of Massive Sulphide Deposits in the Sumail Ophiolite, Oman. *Economic Geology*, 109, 1585-1610.

GODARD, M., DAUTRIA, J.-M., AND PERRIN, M., 2003, Geochemical variability of the Oman Ophiolite lavas; relationship with spatial distribution and paleomagnetic directions. *Geochemistry, Geophysics, Geosystems*, 4(6), 1-15.

GODARD, M., BOSCH, D., AND EINAUDI, F., 2006, A MORB source for low-Ti magmatism in the Sumail ophiolite. *Chemical Geology*, 234, 58–78.

GOODENOUGH, K.M., STYLES, M.T., SCHOEFIELD, D., THOMAS, R.J., CROWLEY, Q.C., LILLY, R.M., MCKERVEY, J., STEPHENSON, D., CARNEY, J.N., 2010, Architecture of the Oman-UAE ophiolite: evidence for a multi-phase magmatic history. *Arab Journal of Geosciences*, 3, 439-458.

GOODENOUGH, K.M., THOMAS, R.J., STYLES, M.T., SCHOFIELD, D.I., MACLEOD, C.J., 2014. Records of Ocean Growth and Destruction in the Oman-UAE Ophiolite. *Elements*, 10, 109-114

GRAY, D.R., GREGORY, R.T., AND MILLER, J.M., A new Structural profile along the Muscat-Ibra transect, Oman: implications for emplacement of the Semail ophiolite. *Geological Society of America*, 349, 513-523.

GREGORY, R.T., GRAY, D.R., AND MILLER, J.M., 1998, Tectonics of the Arabian margin associated with the emplacement of the Oman margin along the Ibra transect: new evidences from northeast Saih Hatat Tectonics, 17, 657-670.

HÄUSSINGER, H., OKRUSCH, M. & SCHEEPERS, D., 1993, Geochemistry of premetamorphic hydrothermal alteration of metasedimentary rocks associated to the Gorob massive sulphide prospect, Damara orogen, Namibia. *Economic Geology*, 88, 72.49.

HANNINGTON, M.D., 2014, Volcanogenic Massive Sulphide Deposits. *In* HEINRICH D., HOLLAND, H.D. AND TUREKIAN, K.K. (eds), *Treatise on Geochemistry* (2nd Edition), 13, 463-488.

HANNINGTON, M.D., GALLEY, A.G., HERZIG, P.M., PETERSEN, S., 1998, Comparison of the TAG Mound and Stockwork Complex with Cyprus-type Massive Sulphide Deposits. *In* HERZIG, P.M., HUMPHRIS, S.E., MILLER, D.J., AND ZIERENBERG, R.A. (eds), *Procedures in ODP Scientific Results*, 158.

HERRINGTON, R., MASLENNIKOV, V., ZAYKOV, V., SERAVKIN, I., KOSAREV, A., BUSCHMANN, B., ORGEVAL, J., HOLLAND, N., TESALINA, S., NIMIS, P., ARMSTRONG, R., 2005, Classification of VMS deposits: Lessons from the South Uralides. *Ore Geology Reviews*, 27, 203-237.

HOFMANN, A.W., 2014, Sampling Mantle Heterogeneity through Oceanic Basalts: Isotopes and Trace Elements. *In* CARLSON, R.W., HOLLAND, H.D. AND TUREKIAN, K.K., (eds), *Treatise on Geochemistry* (2nd Edition), 2, 61-101.

HOU, Z., ZHANG, H., 2015, Geodynamics and metallogeny of the eastern Tethyan metallogenic domain. *Ore Geology Reviews*, 70, 346-384.

INOUE, A., MEUNIER, A., PARTIER-MAS, P., RIGAULT, C., BEAUFORT, D., VIEILLARD, P., 2009, Application of chemical geothermometry to low-temperature trioctahedral chlorites. *Clay and Clay Minerals*, 57(3), 371-382.

ISHIKAWA, T., NAGAISHI, K., UMINO, S., 2002, Boninitic volcanism in the Oman ophiolite: Implications for thermal condition during transition from spreading ridge to arc. *Geology*, 30(10), 899-902.

ISHIKAWA, T., FUJISAWA, S., NAGAISHI, K., MASUDA, T., 2005, Trace element characteristics of the fluid liberated from amphibolite-facies slab: Inference from the metamorphic sole beneath the Oman ophiolite and implication for boninite genesis. *Earth and Planetary Sciences Letters*, 240, 355-377.

JOWETT, E.C., 1991, Fitting iron and magnesium into the hydrothermal chlorite geothermometer: GAC/MAC/SEG Joint Annual Meeting, Toronto, Program with Abstracts 16, A62.

KUSANO, Y., ADACHI, Y., MIYASHITA, S., UMINO, S., 2012, Lava accretion system around mid-ocean ridges: Volcanic stratigraphy in the Wadi Fizh area, northern Oman ophiolite. *Geochemistry, Geophysics, Geosystems*, 13.

KRANIDIOTIS, P. & MACLEAN, W.H., 1987, Systematics of chlorite alteration at the Phelps Dodge massive sulphide deposit, Matagami, Quebec. *Economic Geology*, 82, 1898-1911.

LARGE, RR., GEMMEL, J.B., PAULICK, H., & HUSTON, D.L., 2001, The alteration box plot: a simple approach to understanding the relationship between alteration mineralogy and litogeochemistry associated with volcanic-hosted massive sulphide deposits. *Economic Geology*, 96, 957-971.

LEBAS, M.J., LEMAITRE, R.W., STRECKEISEN, A. & ZANETTIN, B., 1986, A Chemical Classification of Volcanic-Rocks Based on the Total Alkali Silica Diagram. *Journal of Petrology*, 27(3), 745-750.

LIPPARD, S.J., SHELTON, A.W., AND GASS, I.G., 1986, *The ophiolite of northern Oman.* Blackwell Scientific Publications Ltd, 165 p.

MACLEAN, W.H., 1990, Mass change calculations in altered volcanic series. *Mineralium Deposita*, 25, 44-49.

MACLEAN AND KRANIDIOTIS, P., 1987, Immobile Elements as Monitors of Mass Transfer in Hydrothermal Alteration: Phelps Dodge Massive Sulphide Deposit, Matagami, Quebec. *Economic geology*, 82, 951-962.

MACLEAN, W.H. AND BARRETT, T.J., 1993, Lithogeochemical techniques using immobile elements. *Journal of Geochemical Explorations*, 48, 109-133.

MACLEOD, C.J., LISSENBERG, C.J., BIBBY, L.E., 2013, "Moist MORB" axial magmatism in the Oman ophiolite: The evidence against a mid-ocean ridge origin. *Geology*, 41(4), 459-462.

MAROSVÖLGYI, K., KRISTMANNSDÓTTIR, H., LACASSE, C., 2010, Retrograde Alteration of Basaltic Rocks in the Þeistareykir High-Temperature Geothermal Field, North-Iceland. *Proceedings World Geothermal Congress*, *Bali, Indonesia*, 9 p.

MCPHIE, JOCELYN & ALLEN, RODNEY, 1993, V*olcanic textures: a guide to the interpretation of textures in volcanic rocks*. Centre for Ore Deposit and Exploration Studies, University of Tasmania, 198 p.

MICHARD, A., BOUDIER, F., GOFFÉ, B., 1991, Obduction *Versus* Subduction and Collision in the Oman Case and Other Tethyan Settings. *In* PETERS, T.J., NICOLAS, A., COLEMAN, R., (eds) *Ophiolite Genesis and Evolution of the Oceanic Litosphere*, Proceedings of the Ophiolite Conference, 447-467.

MORIMOTO, N.; FABRIES; J., FERGUSON, A.K.; GINZBURG, I.V.; ROSS, M.; SEIFERT, F.A. & ZUSSMAN J. (1988). Nomenclature of pyroxenes. *American Mineralogist*, 73, 1123-1133.

MUTTONI, G., GAETANI, M., KENT, D.V., SCIUNNACH, D., ANGIOLINI, L., BERRA, F., GARZANTI, E., MATTEI, M., AND ZANCHI, A., 2009, Opening of the Neo-Tethys Ocean and the Pangea B to Pangea A transformation during the Permian. *GeoArabia*, 14(4), 17-48.

NÉMETH, Z., PUTIS, M., AND HRAŠKO, L., 2016, The relation of metallogeny to geodynamic processes – the n aturel prerequisite for the origin of mineral deposits of public importance (MDoPI): The case study in the Western Carpathians, Slovakia. *Mineralia Slovakia*, 48, 119-134.

NICOLAS, A., BOUDIER, E., ILDEFONSE, B., AND BALL, E., 2000, Accretion of Oman and United Arab Emirates ophiolite—discussion of a new structural map. Marine Geophysical Researches, 21, 147–179.

NONNOTTE, P., CELEUNEER, G., BENOIT, M., 2005, Genesis of andesitic-boninitic magmas at mid-ocean ridges by melting of hydrated peridotites: Geochemical evidence from DSDP Site 334 gabbonorites. *Earth and Planetary Science Letters,* 236, 632-653.

PARTINGTON, G., 2009, Developing Models using GIS to Assess Geological and Economic Risk: An Example from Mineral Exploration in Oman for VMS Copper Gold Mineralisation. *In* P.J., WILLIAMS (eds) *Proceedings of the Tenth Biennal SGA Meeting*, Smart Science for Exploration and Mining, 836-838.

PEARCE, J.A., 1996, A user's guide to basalt discrimination diagrams. *Geological Association of Canada Special Publication*, 12, 79-113.

PEARCE, J.A., 2008, Geochemical fingerprinting of oceanic basalts with applications to ophiolite classification and the search for Archean crust. *Lithos*, 100, 14-48.

PEARCE, J.A., 2014, Immobile Element Fingerprinting of Ophiolites. *Elements*, 10, 101-108.

ROLLINSON, H.R., 1983, Using geochemical data: evaluation, presentation, interpretation. *Longman Geochemistry Series*. Longman, 352 p.

ROLLINSON, H.R., SEARLE, M.P., ABBASI, I.A., AL-LAZKI, A.I., AL KINDI, M.H., 2014, Tectonic evolution of the Oman Mountains: an introduction, *In* ROLLISON, H.R., SEARLE, M.P., ABBASI, I.A., AL-LAZKI, A. & AL KINDY (eds) *Tectonic Evolution of the Oman Mountains.* Geological Society, 392, 1-7.

ROSS, P-S., BÉDARD, J.H., 2009, Magmatic affinity of modern and ancient subalkaline volcanic rocks determined from trace-element discriminant diagrams. *Canadian Journal of Earth Sciences*, 46(11), 823-839.

SACCANI, E., BECCALUVA, L., PHOTIADES, A., ZEDA, O., 2011, Petrogenesis and tectono-magmatic significance of basalts and mantle peridoties from the Albanian-Greek ophiolites and sub-ophiolitic mélanges. New constraints for the Triassic-Jurassic evolution of the Neo-Tethys in the Dinaride sector. *Lithos*, 124, 227-242.

SEARLE, M.P., AND COX, J., 1999, Tectonic setting, origin, and obduction of the Oman ophiolite. *Geological Society of America Bulletin*, 111, 104–122.

SEARLE, M.P., WARREN, C.J., WATERS, D.J., PARRISH, R.R., 2003, Subduction zone polarity in the Oman Mountains: Implications for ophiolite emplacement. *In* DILEK, Y. & ROBINSON P.T. (eds), *Ophiolites in Earth History*. Geological Society, Special Publications, 218, 467-480.

SHANKS, W.C. PAT, III, AND THURSTON, ROLAND, (eds), 2012, *Volcanogenic massive sulphide occurrence model*. U.S. Geological Survey Scientific Investigations Report 2010–5070–C, 345 p.

SUN, S.S., & MCDONOUGH, W.F., 1989, Chemical and isotopic systematics of oceanic basalts: implications for mantle composition and processes, *In* Saunders, A.D. & NORRY, M.J. (eds), *Magmatism in the Ocean Basins*, Geological Society Special Publication No. 42, 313-345.

TILTON, G.R., HOPSON, C.A., AND WRIGHT, J.E., 1981, Uranium-lead isotopic ages of the Sumail ophiolite, Oman, with applications to Tethyan ocean ridge tectonics: *Journal of Geophysical Research*, 86, 2763–2775.

WALSHE, J.L., 1986, A six-component chlorite solid solution model and the conditions of chlorite formation in hydrothermal and geothermal systems. *Economic Geology*, 81, 681-703.

WARREN, C., PARRISH, R., WATERS, D., AND SEARLE, M., 2005, Dating the geologic history of Oman's Sumail ophiolite: Insights from U-Pb Geochronology. *Contributions to Mineralogy and Petrology*, 150, 403–422.

WINCHESTER, J. A. & FLOYD, P.A., 1977, Geochemical discrimination of different magma series and their differentiation products using immobile elements. *Chemical Geology*, 20, 325-343.

ZANE, A., SASSI, R. & GUIDOTTI, C.V., 1998, New data on metamorphic chlorite as petrogenetic indicator mineral, with special regard to greenshist-facies rocks. *The Canadian Mineralogist*, 36, 713-726.

ZANG, W., & FYFE, C.V., 1995, Chloritization of the hydrothermally altered bedrock at the Igarapá Bahia gold deposit, Carajás, Brazil. *Mineralium Deposita*, 30, 30-38.

YAMASKI, T., MAEDA, J., MIZUTA, T., 2006, Geochemical evidence in clinopyroxene from gabbroic sequence for two distinct magmatism in the Oman ophiolite. *Earth and Planetary Science Letters*, 251, 52-65.

YOKOYAMA, T., MAKISHIMA, A. AND NAKAMURA, E.,1999, Evaluation of the coprecipitation of incompatible trace elements with fluoride during silicate rock dissolution by acid digestion. *Chemical Geology*, 157(3), 175-187.

ADDITIONAL REFERENCES:

MAWARID MINING, 2014, Information Guide – Regional and Local Geology of Mandoos. *Mawarid Mining, Unpublished memorandum*, 12p.

APPENDICES

APPENDIX I

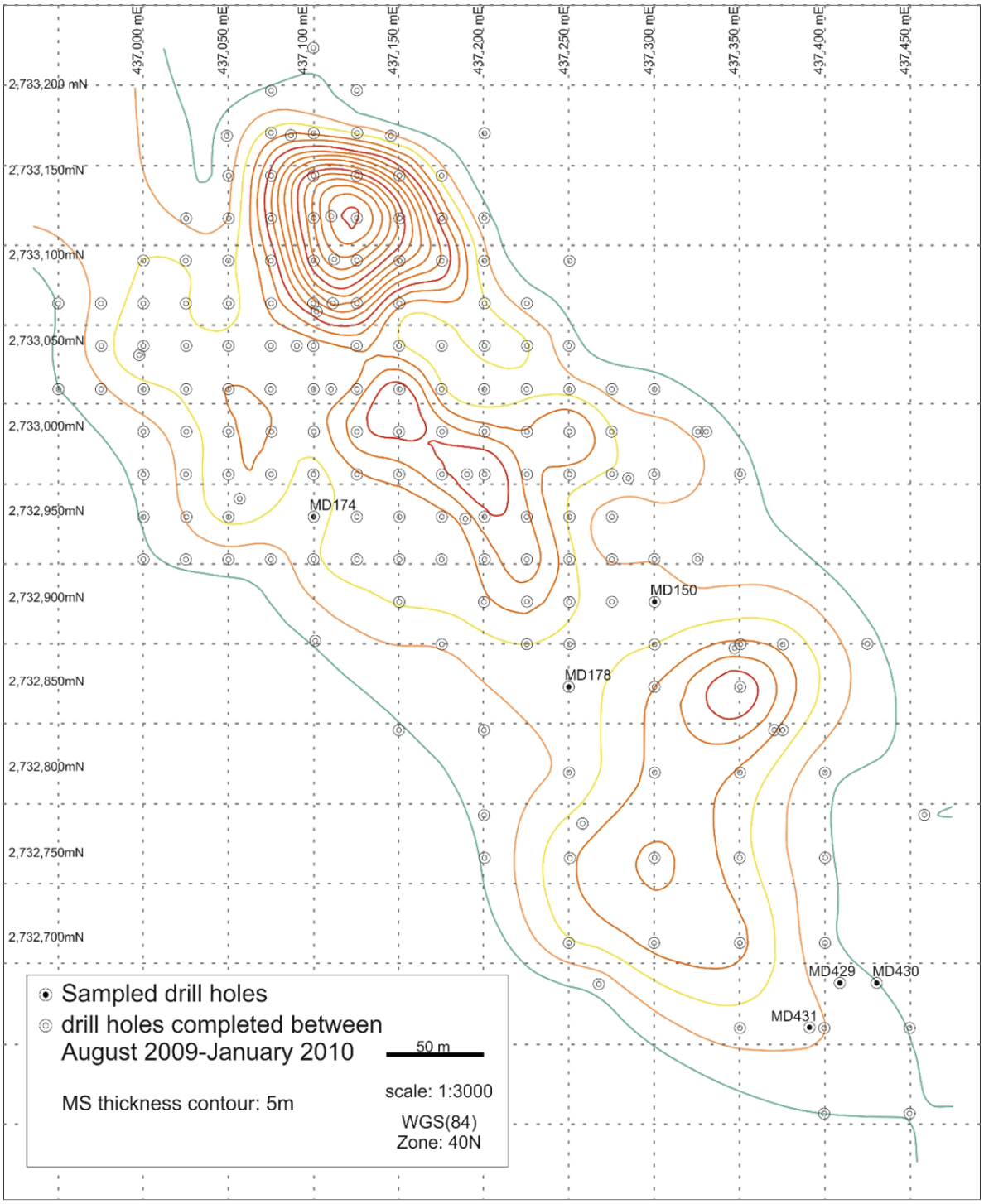

Appendix I- Map showing sampled drillcore locations and MS thickness, with contour lines increasing from blue to red, in 5 m. intervals.

APPENDIX II

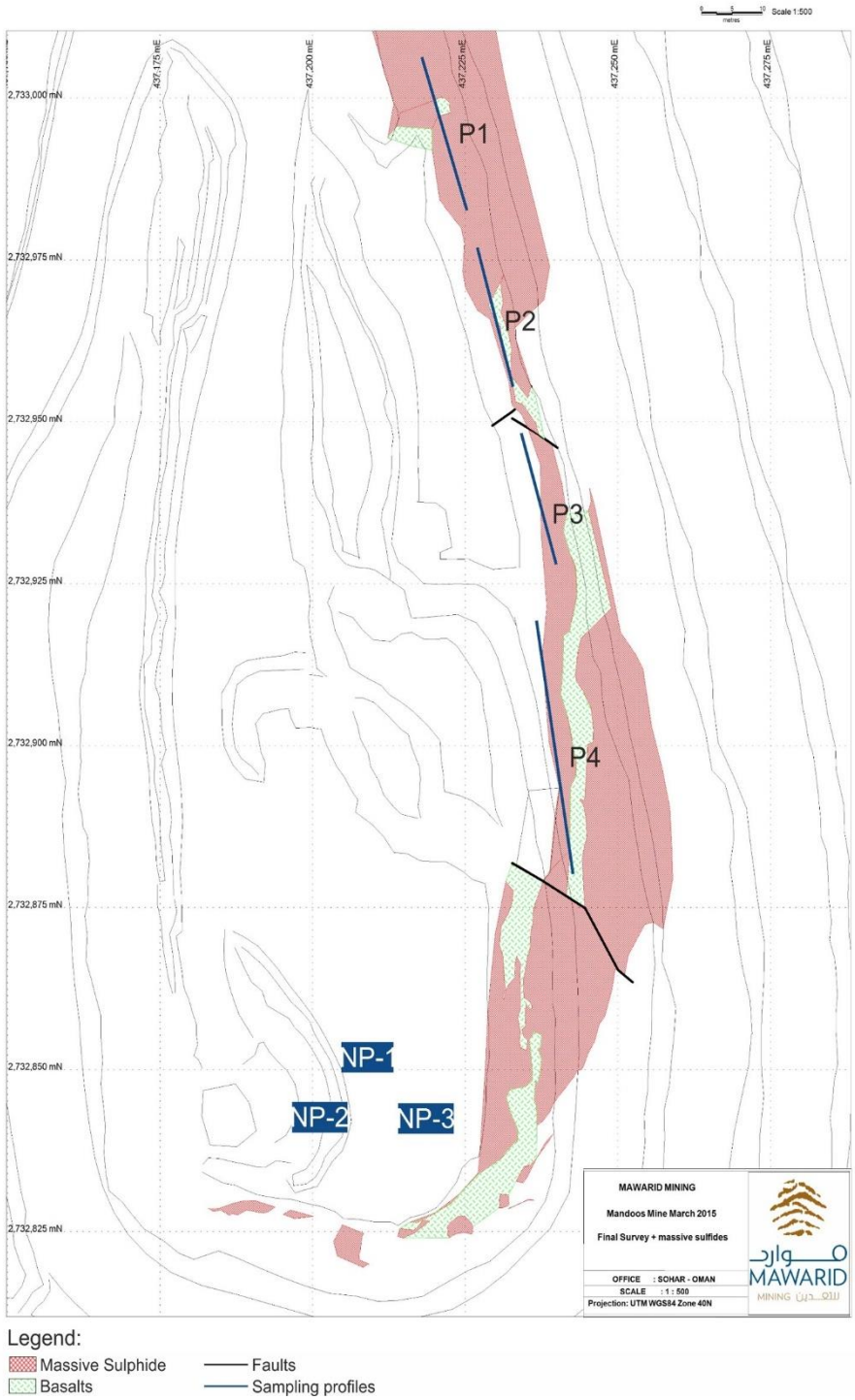

Appendix II- Map showing sampled locations, in the open pit, with a basic cartography of the surroundings of the sampled profiles

APPENDIX III

Appendix III- Analytical condition of the microprobe and detection limites (ppm).

	Element	Crystals	Standards	Detection limit
Feldspar	Ca	PETJ	Diopside	200
	Na	TAP	Tugtupite	200
	Sr	PETJ	Celestite	1300
	Si	PETH	Sanidine	200
	Ba	PETJ	Benitoite	600
	Mg	TAP	Olivine	150
	Ti	PETJ	Rutile	300
	K	PETH	Sanidine	100
	Mn	PETJ	Bustamite	400
	Al	TAP	Pyrope	200
	Fe	LIFH	Almandine	300
Oxides	P	PETJ	Apatite	300
	Na	TAP	Jadeite	200
	S	PETJ	Stibnite	250
	Ba	LIFH	Barite	500
	Bi	PETJ	Bismuth Selenide	700
	Mg	TAP	Periclase	100
	Pb	PETJ	Galena	500
	V	LIFH	V	200
	Ag	PETJ	Ag	300
	As	TAP	Galium Arsenide	350
	K	PETJ	Sanidine	200
	Cr	PETJ	Chromium Oxide	300
	Ca	PETJ	Diopside	200
	Sn	PETJ	Cassiterite	400
	Fe	LIFH	Haematite	250
	Zn	LIF	Ilmenite	700
	Si	LIF	Diopside	200
	Ti	LIFH	Rutile	300
	Ni	LIFH	Nickel Silicide	300
	Ta	LIF	LiTaO3	1500
	Zr	TAP	Zirconia	300
	Mn	PETJ	Rhodonite	300
	Cu	LIFH	Cuprite	350
	Co	LIFH	Skutterudite	350
	Nb	LIF	m21	350
	W	LIF	m34	1500
	Au	LIFH	Au	300
Phyllosilicates	Ca	PETJ	Diopside	200
	F	TAP	Fluorite	600
	Si	TAP	Olivine	300
	Rb	PETJ	CAL-STO	400
	Ti	PETJ	Rutile	200
	Na	TAP	Jadeite	100
	Cl	TAP	Tugtupite	100
	K	PETH	Sanidine	100
	Cr	PETJ	Chromium Oxide	200
	Mg	TAP	Chlorite	150
	Cs	PETJ	Pollucite	300
	Ba	PETJ	Barite	350
	Mn	PETJ	Bustamite	300
	Al	TAP	Almandine	200
	Ni	LIFH	Nickel Silicide	400
	Fe	LIFH	Almandine	200
Al-rich phyllosilicates	Ca	PETJ	Diopside	200
	F	TAP	Fluorite	600
	Si	TAP	Olivine	300
	Rb	PETJ	CAL-STO	400
	Ti	PETJ	Rutile	200
	Na	TAP	Jadeite	100
	Cl	TAP	Tugtupite	100
	K	PETH	Sanidine	100
	Cr	PETJ	Chromium Oxide	200
	Mg	TAP	Chlorite	150
	Cs	PETJ	Pollucite	300
	Ba	PETJ	Barite	350
	Mn	PETJ	Bustamite	300
	Al	TAP	Almandine	200
	Ni	LIFH	Nickel Silicide	400
	Fe	LIFH	Almandine	200

	Element	Crystals	Standards	Detection limit
Pyroxenes	Ti	PETJ	Benitoite	200
	F	TAP	Fluorite	800
	Cl	PETH	Tugtupite	100
	Si	PETJ	Diopside	200
	Mn	PETJ	Bustamite	300
	Na	TAP	Jadeite	200
	Cr	PETJ	Chromium Oxide	200
	Fe	LIFH	Almandine	200
	Mg	TAP	Diopside	100
	Zn	LIFH	Sphalerite	600
	K	PETH	Sanidine	100
	Al	TAP	Plagioclase	100
	Ca	PETJ	Diopside	100
Chalcopyrite, Pyrite and Sphalerite	Bi	PETJ	Bismuth Selenide	1000
	Ga	TAP	m18	250
	Pb	PETJ	Galena	600
	Au	LIFH	Au	250
	Ag	PETJ	REE 6	300
	Ge	TAP	m 17	300
	Cd	PETJ	Cd	300
	In	PETJ	m 28	350
	As	TAP	Galium Arsenide	220
	Sn	PETJ	Cassiterite	300
	S	PETH	Pyrite	100
	Ni	LIFH	Pentlandite	400
	Se	TAP	Bismuth Selenide	200
	Zn	LIF	Sphalerite	700
	Fe	LIFH	Pyrite	200
	Sb	PETJ	Stibnite	300
	Mn	PETJ	Bustamite	300
	Co	LIFH	Skutterudite	200
	Cu	LIFH	Cuprite	300
Apatite	La	PETJ	Monazite	
	F	TAP	Apatite	
	Sr	PETJ	Celestite	
	P	PETH	Apatite	
	Nd	PETJ	REE 6	
	Na	TAP	Jadeite	
	Ce	LIF	Monazite	
	Ca	PETH	Diopside	
	Mn	PETJ	Bustamite	
	Mg	TAP	Periclase	
	Cl	PETJ	Tugtupite	
	Fe	LIFH	Almandine	
Carbonates	Ca	PETJ	Calcite	200
	La	PETJ	Monazite	1300
	Sr	PETH	Celestite	500
	Ba	PETJ	Barite	300
	Na	TAP	Jadeite	400
	Ce	PETJ	Monazite	100
	Fe	LIFH	Magnetite	500
	Ti	PETJ	Rutile	200
	Mg	TAP	Almandine	200
	Mn	PETJ	Bustamite	300
	Zn	LIFH	Sphalerite	400
Zeolites	Ca	PETJ	Diopside	500
	F	TAP	Fluorite	3000
	Si	TAP	Olivine	1500
	Rb	PETJ	CAL-STD	1500
	Ti	PETJ	Rutile	700
	Na	TAP	Jadeite	400
	Cl	TAP	Tugtupite	400
	K	PETH	Sanidine	200
	Cr	PETJ	Chromium Oxide	500
	Mg	TAP	Chlorite	250
	Cs	PETJ	Pollucite	1200
	Ba	LIFH	Barite	1300
	Mn	PETJ	Bustamite	700
	Al	TAP	Almandine	500
	Ni	LIFH	Nickel Silicide	2000
	Fe	LIFH	Almandine	700

APPENDIX IV

Appendix IV- Compositional variation of analysed clinopyroxenes.

n= 71	Min	Max	Std-Dev	Median	Average
SiO2	46.966	54.069	1.118	52.080	52.044
TiO2	0.071	0.436	0.084	0.229	0.233
Al2O3	1.191	4.021	0.811	2.520	2.534
V2O3	BDL	BDL	BDL	BDL	BDL
Cr2O3	0.054	1.111	0.289	0.169	0.332
MgO	13.363	19.548	0.963	17.085	16.979
CaO	11.499	20.868	1.661	19.050	18.764
MnO	0.044	0.340	0.066	0.175	0.176
FeO	5.205	13.766	1.606	6.853	7.254
ZnO	BDL	0.099	0.029	BDL	0.020
Na2O	0.052	1.013	0.145	0.124	0.161
K2O	BDL	0.212	0.035	0.004	0.014

Representative analysis of Clinopyroxenes			
SiO2	52.494	52.490	52.308
TiO2	0.327	0.282	0.253
Al2O3	2.604	2.520	1.968
V2O3	0.000	0.000	0.000
Cr2O3	0.118	0.109	0.126
MgO	17.597	17.552	15.858
CaO	18.726	18.764	19.694
MnO	0.198	0.202	0.240
FeO	7.038	7.009	8.448
NiO	0.000	0.000	0.000
ZnO	0.000	0.002	0.031
Na2O	0.108	0.109	0.163
K2O	0.013	0.000	0.014
Total	99.210	99.039	99.089
6 O	*apuf*		
Distribuição Catiónica			
T			
Si	1.936	1.939	1.950
Al IV	0.064	0.061	0.050
TOTAL T	2.000	2.000	2.000
M1			
Al VI	0.049	0.049	0.037
Ti4+	0.009	0.008	0.007
Cr3+	0.003	0.003	0.004
V3+	0.000	0.000	0.000
Zn2+	0.000	0.000	0.001
soma parc	0.064	0.061	0.056
Mg2+	0.936	0.939	0.881
soma parc	1.000	1.000	0.937
Fe2+	0.000	0.000	0.063
soma parc	1.000	1.000	1.000
Mn2+	0.000	0.000	0.000
TOTAL M1	1.000	1.000	1.000
M2			
Mg2+	0.031	0.028	0.000
Fe2+	0.215	0.216	0.193
Mn2+	0.006	0.006	0.008
Ca2+	0.740	0.743	0.787
Na+	0.008	0.008	0.012
TOTAL M2	0.999	1.000	0.999
Q+J	1.937	1.941	1.948
Sodic %	0.797	0.805	1.210
Quad %	99.203	99.195	98.790
Wo	38.326	38.438	40.571
En	50.111	50.028	45.454
Fs	11.564	11.534	13.975

APPENDIX V

Appendix V- Compositional variation of primary and secondary plagioclases.

	Min	Max	Std-Dev	Median	Average
SiO2	47.993	60.016	3.141	54.473	53.930
Na2O	1.560	5.947	1.152	4.005	3.811
BaO	BDL	0.069	0.021	BDL	0.011
K2O	0.013	1.253	0.272	0.040	0.109
CaO	5.004	16.534	2.649	11.600	12.012
MgO	0.036	2.050	0.463	0.131	0.265
TiO2	BDL	1.253	0.275	0.028	0.103
SrO	BDL	0.195	0.063	0.009	0.044
Al2O3	20.117	31.732	2.549	27.857	27.907
MnO	0.000	0.099	0.030	0.014	0.026
FeO(t)	0.566	5.060	0.965	0.861	1.077

Representative analysis of primary feldspars			
SiO2	48.214	48.429	47.993
Na2O	1.673	1.703	1.560
BaO	0.000	0.007	0.069
K2O	0.023	0.013	0.019
CaO	16.534	16.339	16.518
MgO	0.266	0.212	0.232
TiO2	0.023	0.013	0.019
SrO	0.195	0.000	0.000
Al2O3	31.556	31.732	31.543
MnO	0.000	0.007	0.015
FeO(t)	0.693	0.668	0.745
total	99.180	99.120	98.710
32 O	*apuf*		
Si	8.930	8.940	8.920
Al	6.890	6.910	6.910
Fe3+	0.110	0.100	0.120
Ca	3.280	3.230	3.290
Mg	0.070	0.060	0.060
Na	0.600	0.610	0.560
K	0.010	0.000	0.000
Ba	0.000	0.000	0.010
Ti	0.000	0.000	0.000
Sr	0.02	0	0
Mn	0	0	0
Or	0.14	0.08	0.11
Ab	15.17	15.62	14.34
An	82.84	82.81	83.91

	Min	Max	Std-Dev	Median	Average
SiO2	65.789	70.098	1.414	69.052	68.903
Na2O	10.081	11.460	0.519	11.368	11.072
BaO	BDL	0.061	0.020	0.009	0.016
K2O	0.035	1.145	0.377	0.051	0.223
CaO	0.129	1.673	0.510	0.222	0.487
MgO	0.000	1.631	0.549	0.008	0.343
TiO2	0.000	1.145	0.385	0.043	0.209
SrO	0.000	0.247	0.079	0.111	0.099
Al2O3	18.680	19.667	0.269	19.209	19.212
MnO	0.000	0.063	0.026	0.009	0.023
FeO(t)	0.077	1.111	0.364	0.297	0.404

Representative analysis of secondary feldspars			
SiO2	68.549	69.052	65.789
Na2O	11.382	11.368	10.281
BaO	0.035	0.000	0.009
K2O	0.063	0.043	0.505
CaO	0.129	0.635	1.673
MgO	0.429	0.008	0.741
TiO2	0.063	0.043	0.505
SrO	0.111	0.000	0.126
Al2O3	18.680	19.224	19.667
MnO	0.058	0.063	0.043
FeO(t)	0.536	0.295	1.111
total	100.040	100.730	100.450
32 O			
Si	12.010	12.000	11.640
Al	3.860	3.940	4.100
Fe3+	0.080	0.040	0.160
M-total	15.950	15.970	15.900
Ca	0.020	0.120	0.320
Mg	0.110	0.000	0.200
Na	3.870	3.830	3.530
K	0.010	0.010	0.110
Ba	0.000	0.000	0.000
Ti	0.010	0.010	0.070
Sr	0.01	0	0.01
Mn	0.01	0.01	0.01
T-total	4.05	3.97	4.24
Or	0.35	0.24	2.74
Ab	96.26	96.72	84.91
An	0.6	2.99	7.64

APPENDIX VI

Appendix VI- Compositinal variation of analysed chlorites.

n=16	Min	Max	Std-Dev	Median	Average	resentative analysis of chlorite			
SiO2	27.075	29.180	0.550	28.454	28.396	SiO2	28.671	28.283	27.896
TiO2	BDL	0.058	0.020	0.036	0.030	TiO2	0.003	0.039	0.000
Al2O3	16.929	19.196	0.621	18.314	18.345	Al2O3	18.801	17.961	17.902
FeO	18.094	18.826	0.203	18.449	18.448	FeO	18.365	18.427	18.754
MnO	0.121	0.219	0.027	0.168	0.168	MnO	0.146	0.121	0.164
MgO	18.517	19.914	0.447	19.301	19.223	MgO	19.459	19.301	19.022
CaO	0.183	0.457	0.081	0.376	0.339	CaO	0.457	0.306	0.248
Na2O	BDL	0.029	0.009	0.011	0.011	Na2O	0.011	0.019	0.000
K2O	BDL	0.042	0.011	0.010	0.012	K2O	0.014	0.022	0.009
BaO	BDL	0.059	0.020	0.005	0.014	BaO	0.012	0.005	0.000
Cs2O	BDL	0.006	0.002	BDL	0.000	Cs2O	0.000	0.000	0.000
ZnO	BDL	0.110	0.034	0.026	0.030	ZnO	0.008	0.000	0.067
F	BDL	0.110	0.038	0.012	0.031	F	0.000	0.068	0.000
Cr2O3	0.030	0.098	0.023	0.051	0.057	Cr2O3	0.049	0.098	0.049
NiO	0.000	0.031	0.013	BDL	0.008	NiO	0.000	0.000	0.024
						apuf calculations: 24 ionic charges			
						Group T			
						Si4+	2.935	2.871	2.924
						Al3+ (IV)	1.065	1.129	1.076
						Total	4	4	4
						Group A			
						Ti4+	0.000	0.003	0.000
						Fe3+	0.000	0.000	0.000
						Cr3+	0.000	0.022	0.000
						Al3+ (VI)	0.069	1.020	1.136
						Ba2+	BDL	BDL	BDL
						Zn2+	0.001	0.000	0.005
						Ni2+	0.002	0.004	0.002
						Fe2+	1.572	1.564	1.644
						Mn2+	0.013	0.010	0.015
						Ca2+	0.050	0.033	0.028
						Mg2+	2.969	2.920	2.972
						Cs+	BDL	BDL	BDL
						K+	0.001	0.001	0.001
						Na+	0.002	0.004	BDL
						Total	4.680	5.582	5.802

APPENDIX VII

Appendix VII- Compositional variation of analysed interlayered chlorite-smectite aggregates.

n=30	Min	Max	Std-Dev	Median	Average
SiO2	30.052	36.866	1.586	34.020	33.906
TiO2	BDL	0.015	0.005	BDL	0.003
Al2O3	12.377	13.994	0.385	13.130	13.196
FeO	14.154	21.521	1.726	18.076	17.967
MnO	0.109	0.692	0.140	0.488	0.455
MgO	19.189	24.691	1.146	22.845	22.751
CaO	0.181	1.222	0.199	0.471	0.478
Na2O	0.014	0.098	0.020	0.036	0.039
K2O	BDL	0.046	0.012	0.015	0.018
BaO	BDL	0.081	0.022	0.016	0.021
Cs2O	BDL	0.064	0.014	BDL	0.008
ZnO	BDL	0.072	0.037	0.048	0.040
F	BDL	0.197	0.043	0.004	0.027
Cr2O3	BDL	0.110	0.028	0.066	0.058
NiO	BDL	0.079	0.025	BDL	0.019

Representative analysis of *Chl-Sme*			
SiO2	34.899	35.310	36.072
TiO2	0.000	0.000	0.005
Al2O3	13.566	13.389	13.647
FeO	16.560	16.604	14.359
MnO	0.234	0.252	0.163
MgO	24.051	23.934	24.109
CaO	0.181	0.188	0.256
Na2O	0.038	0.019	0.030
K2O	0.025	0.022	0.032
BaO	0.022	0.000	0.000
Cs2O	0.012	0.000	0.016
ZnO			
F	0.036	0.197	0.000
Cr2O3	0.069	0.066	0.065
NiO	0.000	0.003	0.000
H2O	10.316	10.096	11.239
apuf calculations: 50 ionic charges			
IV			
Si 4+	6.058	6.114	6.230
Al 3+	1.942	1.886	1.770
Total	8	8	8
VI			
Ti 3+	0.000	0.000	0.001
Al 3+	0.834	0.847	1.007
Fe 2+	2.404	2.404	2.074
Mn 2+	0.034	0.037	0.024
Mg 2+	6.223	6.177	6.206
Zn 2+	0.000	0.000	0.000
Cr 3+	0.009	0.009	0.009
Ni 2+	0.000	0.000	0.000
Total	8.671	8.628	8.313
Exchange			
Ca 2+	0.034	0.035	0.047
Na +	0.013	0.006	0.010
K +	0.006	0.005	0.007
Ba 2+	0.001	0.000	0.000
Cs +	0.001	0.000	0.001
Total	0.054	0.046	0.066

APPENDIX VIII

Appendix VIII- Compositional variation of analysed Al-rich phyllosilicates

	1	2	3	4	5	6	7	9	1	2	3	4	5	6	7	8	9	10	11	12
Al2O3	37.762	29.622	37.414	38.08	38.341	38.356	37.736	36.663	26.728	21.64	28.337	27.511	27.641	27.924	29.623	30.936	30.311	29.027	30.625	31.046
SiO2	46.828	32.472	43.761	45.756	45.722	45.482	42.383	46.192	49.311	42.55	50.775	50.43	50.542	51.2	49.76	50.954	49.668	48.242	52.089	52.578
FeO	0.696	1.413	0.444	0.821	1.01	1.051	0.924	0.588	6.178	13.469	1.692	2.573	3.466	2.305	2.453	2.057	1.367	1.216	1.095	0.694
CaO	0.086	0.135	0.057	0.08	0.098	0.098	0.081	0.115	0.261	0.139	0.228	0.361	0.314	0.194	0.304	0.26	1.01	1.229	0.239	0.309
BaO	0.046	0	0.058	0.003	0	0.052	0	0.002	0	0.099	0.009	0.058	0	0.035	0.055	0.058	0.015	0.011	0.017	0.076
Rb2O	0	0	0	0	0	0	0	0	0	0	0	0	0	0	0	0	0	0	0	0
TiO2	0	0	0	0	0	0	0	0	0.017	0.03	0.033	0.007	0.006	0	0.025	0.026	0	0.001	0.025	0.044
Na2O	0.051	0.079	0.078	0.055	0.05	0.05	0.087	0.049	1.642	0.942	1.45	1.534	1.836	1.555	1.939	2.194	2.202	2.052	2.057	2.237
Cl	0.054	0.356	0.155	0.064	0.089	0.105	0.12	0.096	0.165	0.26	0.161	0.173	0.14	0.161	0.143	0.146	0.07	0.085	0.115	0.11
K2O	0.024	0.027	0.018	0.022	0.022	0.017	0.015	0.044	1.278	0.809	1.306	1.316	1.334	1.26	1.472	1.599	1.591	1.556	1.636	1.494
Cr2O3	0.064	0.068	0.101	0.038	0.045	0.035	0.04	0.005	0.078	0.021	0.064	0.087	0.025	0.047	0.055	0.073	0.084	0.054	0.073	0.073
MgO	0.101	0.22	0.083	0.127	0.108	0.164	0.189	0.289	1.266	1.456	1.341	1.437	1.279	1.403	1.207	0.696	0.548	0.598	0.9	0.692
Cs2O	0	0	0	0.006	0.018	0	0	0	0	0	0	0	0	0	0.003	0	0	0.002	0	0
NiO	0.017	0	0	0	0	0.019	0.023	0	0	0.005	0	0	0	0	0	0.027	0	0	0	0
MnO	0.01	0.008	0	0.009	0.012	0	0	0	0	0.006	0	0.06	0.022	0.001	0	0	0	0	0	0.019
F	0	0	0.063	0	0	0.001	0	0.041	0	0.175	0.082	0	0	0	0	0	0.099	0.082	0.099	0.039
H2O	14.27	35.681	17.828	14.952	14.507	14.594	18.43	15.958	13.116	18.531	14.595	14.492	13.43	13.953	12.992	11.007	13.092	15.898	11.098	10.629
Total	100	100	100	100	100	100	100	100	100	100	100	100	100	100	100	100	100	100	100	100

	13	14	15	16	17	18	19	20	21	22
Al2O3	31.797	30.909	33.175	32.567	30.284	30.174	32.011	31.463	29.85	29.81
SiO2	53.835	51.573	51.49	52.278	51.797	52.707	53.019	53.301	54.453	54.977
FeO	0.724	0.736	0.491	0.433	1.88	0.402	0.383	0.459	0.633	0.597
CaO	0.304	0.25	0.29	0.287	0.288	0.297	0.299	0.273	0.312	0.282
BaO	0	0.014	0.056	0.058	0.062	0.066	0.024	0.015	0	0.067
Rb2O	0	0	0	0	0	0	0	0	0	0
TiO2	0.007	0.023	0.034	0.014	0.024	0.006	0	0.002	0.016	0
Na2O	2.288	2.055	2.277	2.171	2.044	2.059	2.195	2.002	1.757	1.824
Cl	0.061	0.101	0.072	0.091	0.122	0.113	0.066	0.08	0.072	0.074
K2O	1.447	1.644	1.81	2.033	2.031	1.97	1.776	1.845	1.75	1.724
Cr2O3	0.05	0.039	0.083	0.058	0.04	0.076	0.086	0.067	0.122	0.051
MgO	0.679	0.877	0.438	0.456	0.545	0.589	0.59	0.66	1.015	0.997
Cs2O	0	0	0.019	0.027	0	0	0	0	0	0
NiO	0	0.002	0	0.053	0	0	0	0	0	0
MnO	0	0.006	0	0	0	0.058	0	0	0	0
F	0	0.04	0	0.068	0.018	0	0	0	0.039	0
H2O	8.823	11.773	9.781	9.455	10.9	11.506	9.566	9.852	10.013	9.614
Total	100	100	100	100	100	100	100	100	100	100

APPENDIX IX

Appendix IX- Compositionl variation of analysed zeolites.

Note: *apuf* data was calculated using the number of oxygens for each mineral.

MD-P3-9-1-3

Sample	1	2	3	4	5	6	8	9	10
CaO	8.294	8.312	8.994	8.212	9.023	8.796	8.300	8.484	8.883
F	0.000	0.000	0.000	0.000	0.000	0.000	0.216	0.000	0.000
SiO2	62.477	62.068	61.614	61.395	61.507	59.377	60.656	62.311	60.899
Rb2O	0.000	0.000	0.000	0.000	0.000	0.000	0.000	0.000	0.000
TiO2	0.000	0.000	0.044	0.064	0.089	0.000	0.000	0.000	0.000
Na2O	0.961	1.227	1.126	0.841	1.127	0.992	0.961	0.954	0.988
Cl	0.001	0.019	0.038	0.000	0.016	0.001	0.000	0.000	0.000
K2O	0.137	0.081	0.085	0.071	0.067	0.082	0.065	0.114	0.062
Cr2O3	0.000	0.091	0.094	0.056	0.000	0.077	0.000	0.010	0.175
MgO	0.001	0.000	0.000	0.036	0.000	0.000	0.015	0.000	0.042
Cs2O	0.000	0.000	0.000	0.000	0.000	0.000	0.041	0.000	0.000
BaO	0.015	0.046	0.335	0.000	0.289	0.123	0.307	0.000	0.092
MnO	0.177	0.000	0.000	0.104	0.000	0.146	0.000	0.041	0.000
Al2O3	17.399	17.756	17.855	17.084	18.469	18.348	17.384	16.758	18.035
NiO	0.000	0.000	0.000	0.110	0.155	0.000	0.157	0.172	0.000
FeO	0.073	0.000	0.043	0.022	0.000	0.025	0.031	0.000	0.000
H2O	10.464	10.405	9.783	12.007	9.260	12.034	11.959	11.156	10.827
Total	100.000	100.000	100.000	100.000	100.000	100.000	100.000	100.000	100.000
apuf									
Ca	0.847	0.849	0.918	0.853	0.916	0.920	0.867	0.873	0.915
Si	6.032	5.994	5.946	6.028	5.903	5.872	5.987	6.064	5.928
Rb	0.000	0.000	0.000	0.000	0.000	0.000	0.000	0.000	0.000
Ti	0.000	0.000	0.003	0.005	0.007	0.000	0.000	0.000	0.000
Na	0.180	0.230	0.211	0.160	0.210	0.190	0.184	0.180	0.186
K	0.017	0.010	0.010	0.009	0.008	0.010	0.008	0.014	0.008
Cr	0.000	0.007	0.007	0.004	0.000	0.006	0.000	0.001	0.013
Mg	0.000	0.000	0.000	0.005	0.000	0.000	0.002	0.000	0.006
Cs	0.000	0.000	0.000	0.000	0.000	0.000	0.002	0.000	0.000
Ba	0.001	0.002	0.013	0.000	0.011	0.005	0.012	0.000	0.004
Mn	0.014	0.000	0.000	0.009	0.000	0.012	0.000	0.003	0.000
Al	1.980	2.021	2.031	1.977	2.089	2.138	2.022	1.922	2.069
Ni	0.000	0.000	0.000	0.009	0.012	0.000	0.012	0.013	0.000
Fe	0.006	0.000	0.003	0.002	0.000	0.002	0.003	0.000	0.000
X	1.059	1.090	1.152	1.036	1.145	1.138	1.074	1.071	1.118
Y	1.980	2.028	2.038	1.981	2.089	2.144	2.022	1.923	2.082
Si	6.032	5.994	5.946	6.028	5.903	5.872	5.987	6.064	5.928
O	16	16	16	16	16	16	16	16	16

EPSTILBITE

$CaAl_2Si_6O_{16} \cdot 5H_2O$

Sample	1	2	3	4	5	6	7	8	9	10	11	12	13	14	15	16	17	18	19	20	21	22	23	24	25	26	27	28	29	30
CaO	10.475	10.941	11.105	10.732	10.748	10.590	10.352	10.072	10.331	10.409	10.501	10.424	10.358	10.551	10.789	10.432	11.268	10.836	10.808	10.903	10.776	10.757	10.508	11.009	11.139	10.686	11.223	10.743	11.008	10.665
F	0.000	0.319	0.000	0.108	0.221	0.111	0.210	0.000	0.000	0.000	0.000	0.000	0.000	0.318	0.100	0.000	0.000	0.209	0.000	0.000	0.210	0.103	0.429	0.317	0.422	0.000	0.107	0.215	0.000	0.106
SiO2	57.306	57.012	56.732	55.287	54.136	57.584	56.312	56.745	56.166	57.216	57.097	55.406	55.965	56.001	54.613	57.124	54.024	57.094	55.953	57.382	57.087	55.796	57.233	55.481	56.715	56.536	55.202	57.913	57.620	56.953
Rb2O	0.000	0.000	0.000	0.000	0.000	0.000	0.000	0.000	0.000	0.000	0.000	0.000	0.000	0.000	0.000	0.000	0.000	0.000	0.000	0.000	0.000	0.000	0.000	0.000	0.000	0.000	0.000	0.000	0.000	0.000
TiO2	0.000	0.000	0.000	0.000	0.069	0.000	0.035	0.038	0.000	0.017	0.000	0.000	0.001	0.000	0.008	0.000	0.041	0.031	0.000	0.020	0.000	0.000	0.114	0.000	0.052	0.006	0.047	0.043	0.000	0.000
Na2O	0.148	0.242	0.193	0.393	0.166	0.275	0.415	0.450	0.370	0.478	0.368	0.249	0.547	0.411	0.405	0.347	0.203	0.144	0.304	0.308	0.266	0.516	0.302	0.286	0.110	0.142	0.417	0.596	0.228	0.320
Cl	0.042	0.000	0.015	0.015	0.015	0.000	0.039	0.000	0.027	0.062	0.029	0.016	0.000	0.010	0.082	0.036	0.023	0.000	0.015	0.000	0.000	0.009	0.033	0.001	0.067	0.000	0.007	0.043	0.000	0.020
K2O	0.512	0.494	0.414	0.383	0.329	0.497	0.477	0.494	0.531	0.578	0.557	0.413	0.457	0.561	0.477	0.340	0.215	0.401	0.424	0.452	0.501	0.483	0.525	0.472	0.423	0.490	0.404	0.506	0.497	0.481
Cr2O3	0.010	0.000	0.070	0.056	0.137	0.189	0.084	0.060	0.151	0.077	0.200	0.137	0.056	0.088	0.148	0.049	0.021	0.084	0.025	0.178	0.021	0.000	0.084	0.000	0.140	0.147	0.112	0.028	0.066	0.066
MgO	0.000	0.018	0.063	0.000	0.062	0.006	0.007	0.021	0.017	0.000	0.000	0.004	0.000	0.000	0.000	0.000	0.000	0.022	0.000	0.005	0.048	0.045	0.000	0.026	0.000	0.033	0.031	0.019	0.009	0.029
Cs2O	0.000	0.000	0.097	0.000	0.000	0.041	0.179	0.000	0.106	0.057	0.098	0.000	0.000	0.065	0.016	0.090	0.082	0.000	0.000	0.000	0.000	0.000	0.000	0.139	0.000	0.049	0.000	0.000	0.000	0.000
BaO	0.107	0.061	0.000	0.000	0.139	0.092	0.015	0.123	0.000	0.000	0.062	0.077	0.062	0.062	0.000	0.031	0.062	0.015	0.000	0.153	0.000	0.123	0.015	0.092	0.000	0.031	0.000	0.046	0.000	0.107
MnO	0.014	0.007	0.018	0.000	0.000	0.000	0.104	0.067	0.000	0.000	0.021	0.000	0.033	0.000	0.187	0.045	0.126	0.000	0.000	0.002	0.000	0.000	0.000	0.000	0.099	0.026	0.000	0.000	0.014	0.073
Al2O3	20.138	20.465	20.755	19.743	20.346	19.645	20.037	19.498	19.814	19.201	18.938	19.555	19.682	19.720	20.148	19.339	19.698	20.550	20.424	19.818	19.878	20.011	20.038	20.166	20.069	20.031	20.790	19.911	20.268	20.730
NiO	0.000	0.000	0.124	0.016	0.047	0.078	0.016	0.047	0.000	0.000	0.000	0.173	0.125	0.078	0.047	0.110	0.095	0.000	0.000	0.000	0.000	0.000	0.062	0.000	0.125	0.125	0.109	0.016	0.000	0.093
FeO	0.064	0.000	0.000	0.000	0.000	0.000	0.054	0.000	0.000	0.015	0.000	0.023	0.068	0.000	0.053	0.000	0.042	0.001	0.000	0.070	0.052	0.090	0.082	0.000	0.057	0.027	0.075	0.069	0.000	0.026
H2O	11.196	10.575	10.416	13.315	13.679	10.941	11.761	12.386	12.494	11.905	12.137	13.528	12.646	12.270	12.986	12.067	14.107	10.701	12.052	10.708	11.250	12.112	10.763	12.145	10.776	11.669	11.521	9.954	10.291	10.381
Total	100.000	100.000	100.000	100.000	100.000	100.000	100.000	100.000	100.000	100.000	100.000	100.000	100.000	100.000	100.000	100.000	100.000	100.000	100.000	100.000	100.000	100.000	100.000	100.000	100.000	100.000	100.000	100.000	100.000	100.000
apuf																														
Ca	5.749	5.987	6.066	6.053	6.105	5.807	5.747	5.605	5.765	5.767	5.839	5.889	5.796	5.897	6.091	5.784	6.440	5.923	6.000	5.969	5.931	5.998	5.762	6.154	6.127	5.911	6.229	5.838	5.987	5.822
Si	29.736	29.493	29.297	29.481	29.070	29.854	29.554	29.854	29.633	29.971	30.015	29.593	29.608	29.588	29.149	29.946	29.189	29.503	29.368	29.701	29.705	29.414	29.671	29.322	29.491	29.564	28.965	29.753	29.629	29.391
Rb	0.000	0.000	0.000	0.000	0.000	0.000	0.000	0.000	0.000	0.000	0.000	0.000	0.000	0.000	0.000	0.000	0.000	0.000	0.000	0.000	0.000	0.000	0.000	0.000	0.000	0.000	0.000	0.000	0.000	0.000
Ti	0.000	0.000	0.000	0.000	0.028	0.000	0.014	0.015	0.000	0.007	0.000	0.000	0.000	0.000	0.003	0.000	0.017	0.012	0.000	0.008	0.000	0.000	0.045	0.000	0.021	0.002	0.019	0.017	0.000	0.000
Na	0.149	0.243	0.193	0.406	0.173	0.276	0.422	0.459	0.378	0.485	0.375	0.258	0.561	0.421	0.419	0.353	0.213	0.144	0.309	0.309	0.268	0.527	0.304	0.293	0.111	0.144	0.424	0.594	0.227	0.320
K	0.339	0.326	0.273	0.261	0.225	0.329	0.319	0.332	0.357	0.386	0.374	0.281	0.308	0.378	0.325	0.227	0.148	0.264	0.284	0.298	0.333	0.325	0.347	0.318	0.281	0.327	0.270	0.332	0.326	0.317
Cr	0.004	0.000	0.029	0.024	0.058	0.077	0.035	0.025	0.063	0.032	0.083	0.058	0.023	0.037	0.062	0.020	0.009	0.034	0.010	0.073	0.009	0.000	0.034	0.000	0.058	0.061	0.046	0.011	0.027	0.027
Mg	0.000	0.014	0.049	0.000	0.050	0.005	0.005	0.016	0.013	0.000	0.000	0.003	0.000	0.000	0.000	0.000	0.000	0.017	0.000	0.004	0.037	0.035	0.000	0.020	0.000	0.026	0.024	0.015	0.007	0.022
Cs	0.000	0.000	0.021	0.000	0.000	0.009	0.040	0.000	0.024	0.013	0.022	0.000	0.000	0.015	0.004	0.020	0.019	0.000	0.000	0.000	0.000	0.000	0.000	0.031	0.000	0.011	0.000	0.000	0.000	0.000
Ba	0.022	0.012	0.000	0.000	0.029	0.019	0.003	0.025	0.000	0.000	0.013	0.016	0.013	0.013	0.000	0.006	0.013	0.003	0.000	0.031	0.000	0.025	0.003	0.019	0.000	0.006	0.000	0.009	0.000	0.022
Mn	0.006	0.003	0.008	0.000	0.000	0.000	0.046	0.030	0.000	0.000	0.009	0.000	0.015	0.000	0.085	0.020	0.058	0.000	0.000	0.001	0.000	0.000	0.000	0.000	0.044	0.012	0.000	0.000	0.006	0.032
Al	12.315	12.476	12.631	12.407	12.876	12.003	12.393	12.089	12.320	11.853	11.733	12.309	12.271	12.279	12.673	11.948	12.543	12.514	12.634	12.089	12.190	12.432	12.243	12.560	12.298	12.344	12.856	12.055	12.283	12.608
Ni	0.000	0.000	0.052	0.007	0.020	0.033	0.007	0.020	0.000	0.000	0.000	0.074	0.053	0.033	0.020	0.046	0.041	0.000	0.000	0.000	0.000	0.000	0.026	0.000	0.052	0.053	0.046	0.007	0.000	0.039
Fe	0.028	0.000	0.000	0.000	0.000	0.000	0.024	0.000	0.000	0.007	0.000	0.010	0.030	0.000	0.024	0.000	0.019	0.000	0.000	0.030	0.023	0.040	0.036	0.000	0.025	0.012	0.033	0.030	0.000	0.011
X	6.265	6.585	6.609	6.720	6.582	6.445	6.583	6.467	6.538	6.652	6.632	6.448	6.693	6.723	6.923	6.411	6.890	6.351	6.594	6.613	6.569	6.911	6.416	6.836	6.562	6.436	6.948	6.787	6.554	6.534
Y	12.319	12.476	12.660	12.430	12.934	12.080	12.428	12.114	12.383	11.885	11.816	12.367	12.295	12.316	12.736	11.968	12.552	12.549	12.644	12.162	12.199	12.432	12.277	12.560	12.356	12.405	12.902	12.067	12.309	12.634
Si	29.736	29.493	29.297	29.481	29.070	29.854	29.554	29.854	29.633	29.971	30.015	29.593	29.608	29.588	29.149	29.946	29.189	29.503	29.368	29.701	29.705	29.414	29.671	29.322	29.491	29.564	28.965	29.753	29.629	29.391
O	84	84	84	84	84	84	84	84	84	84	84	84	84	84	84	84	84	84	84	84	84	84	84	84	84	84	84	84	84	84

PAULINGITE-CA?

$(Ca,K,Na,Ba,\square)_{10}\ (Si,\ Al)_{42}O_{84}\cdot 34H_2O$

	MD-P3-9-1-3								
Sample	1	2	3	4	5	6	8	9	10
CaO	8.294	8.312	8.994	8.212	9.023	8.796	8.300	8.484	8.883
F	0.000	0.000	0.000	0.000	0.000	0.000	0.216	0.000	0.000
SiO2	62.477	62.068	61.614	61.395	61.507	59.377	60.656	62.311	60.899
Rb2O	0.000	0.000	0.000	0.000	0.000	0.000	0.000	0.000	0.000
TiO2	0.000	0.000	0.044	0.064	0.089	0.000	0.000	0.000	0.000
Na2O	0.961	1.227	1.126	0.841	1.127	0.992	0.961	0.954	0.988
Cl	0.001	0.019	0.038	0.000	0.016	0.001	0.000	0.000	0.000
K2O	0.137	0.081	0.085	0.071	0.067	0.082	0.065	0.114	0.062
Cr2O3	0.000	0.091	0.094	0.056	0.000	0.077	0.000	0.010	0.175
MgO	0.001	0.000	0.000	0.036	0.000	0.000	0.015	0.000	0.042
Cs2O	0.000	0.000	0.000	0.000	0.000	0.000	0.041	0.000	0.000
BaO	0.015	0.046	0.335	0.000	0.289	0.123	0.307	0.000	0.092
MnO	0.177	0.000	0.000	0.104	0.000	0.146	0.000	0.041	0.000
Al2O3	17.399	17.756	17.855	17.084	18.469	18.348	17.384	16.758	18.035
NiO	0.000	0.000	0.000	0.110	0.155	0.000	0.157	0.172	0.000
FeO	0.073	0.000	0.043	0.022	0.000	0.025	0.031	0.000	0.000
H2O	10.464	10.405	9.783	12.007	9.260	12.034	11.959	11.156	10.827
Total	100.000	100.000	100.000	100.000	100.000	100.000	100.000	100.000	100.000
apuf									
Ca	0.847	0.849	0.918	0.853	0.916	0.920	0.867	0.873	0.915
Si	6.032	5.994	5.946	6.028	5.903	5.872	5.987	6.064	5.928
Rb	0.000	0.000	0.000	0.000	0.000	0.000	0.000	0.000	0.000
Ti	0.000	0.000	0.003	0.005	0.007	0.000	0.000	0.000	0.000
Na	0.180	0.230	0.211	0.160	0.210	0.190	0.184	0.180	0.186
K	0.017	0.010	0.010	0.009	0.008	0.010	0.008	0.014	0.008
Cr	0.000	0.007	0.007	0.004	0.000	0.006	0.000	0.001	0.013
Mg	0.000	0.000	0.000	0.005	0.000	0.000	0.002	0.000	0.006
Cs	0.000	0.000	0.000	0.000	0.000	0.000	0.002	0.000	0.000
Ba	0.001	0.002	0.013	0.000	0.011	0.005	0.012	0.000	0.004
Mn	0.014	0.000	0.000	0.009	0.000	0.012	0.000	0.003	0.000
Al	1.980	2.021	2.031	1.977	2.089	2.138	2.022	1.922	2.069
Ni	0.000	0.000	0.000	0.009	0.012	0.000	0.012	0.013	0.000
Fe	0.006	0.000	0.003	0.002	0.000	0.002	0.003	0.000	0.000
X	1.059	1.090	1.152	1.036	1.145	1.138	1.074	1.071	1.118
Y	1.980	2.028	2.038	1.981	2.089	2.144	2.022	1.923	2.082
Si	6.032	5.994	5.946	6.028	5.903	5.872	5.987	6.064	5.928
O	16	16	16	16	16	16	16	16	16

EPSTILBITE

$CaAl_2Si_6O_{16} \cdot 5H_2O$

MD-P2-9-1-2

Sample	1	2	3	4	5	6	7	8	9	10	11	12	13	14	15	16	17	18	19	20
CaO	11.598	11.609	10.878	10.305	10.753	11.008	11.123	10.797	10.674	10.422	10.263	10.626	11.090	11.257	10.853	10.558	11.558	10.326	11.328	10.685
F	0.000	0.000	0.540	0.000	0.000	0.000	0.000	0.000	0.214	0.000	0.000	0.000	0.000	0.000	0.103	0.321	0.322	0.113	0.000	0.000
SiO2	54.711	53.895	53.292	55.921	53.700	56.336	54.361	54.448	56.780	53.895	54.818	58.508	57.896	56.010	56.210	55.461	56.432	55.573	53.229	54.714
Rb2O	0.000	0.000	0.000	0.000	0.000	0.000	0.000	0.000	0.000	0.000	0.000	0.000	0.000	0.000	0.000	0.000	0.000	0.000	0.000	0.000
TiO2	0.000	0.000	0.075	0.000	0.027	0.000	0.000	0.000	0.000	0.003	0.000	0.028	0.053	0.000	0.000	0.039	0.000	0.000	0.000	0.000
Na2O	0.000	0.127	0.121	0.457	0.160	0.218	0.430	0.348	0.326	0.365	0.422	0.259	0.276	0.474	0.391	0.240	0.220	0.518	0.182	0.317
Cl	0.000	0.000	0.000	0.000	0.042	0.033	0.005	0.000	0.000	0.006	0.131	0.009	0.053	0.000	0.036	0.061	0.009	0.049	0.040	0.024
K2O	0.312	0.206	0.339	0.623	0.435	0.450	0.471	0.387	0.469	0.510	0.539	0.526	0.432	0.412	0.437	0.480	0.499	0.545	0.329	0.510
Cr2O3	0.007	0.134	0.085	0.000	0.053	0.000	0.000	0.000	0.000	0.078	0.131	0.115	0.156	0.056	0.084	0.000	0.129	0.000	0.035	0.074
MgO	0.001	0.004	0.084	0.021	0.373	0.018	0.002	0.000	0.063	0.026	0.008	0.000	0.000	0.001	0.000	0.012	0.035	0.054	0.039	0.000
Cs2O	0.000	0.090	0.000	0.000	0.000	0.000	0.000	0.016	0.000	0.000	0.000	0.000	0.089	0.163	0.000	0.000	0.000	0.000	0.000	0.025
BaO	0.015	0.000	0.047	0.123	0.000	0.000	0.000	0.046	0.046	0.000	0.000	0.000	0.000	0.000	0.000	0.000	0.000	0.000	0.000	0.000
MnO	0.044	0.000	0.000	0.064	0.095	0.000	0.000	0.000	0.056	0.000	0.000	0.000	0.039	0.023	0.000	0.000	0.000	0.025	0.053	0.064
Al2O3	20.126	20.859	20.418	20.505	18.957	20.757	21.321	20.219	20.157	19.924	19.479	19.855	20.822	20.739	20.720	19.416	20.821	19.550	20.781	20.459
NiO	0.016	0.188	0.000	0.172	0.174	0.000	0.094	0.000	0.000	0.253	0.032	0.155	0.000	0.062	0.172	0.047	0.171	0.000	0.032	0.000
FeO	0.012	0.007	0.074	0.026	0.242	0.000	0.000	0.097	0.000	0.040	0.054	0.058	0.000	0.026	0.000	0.022	0.000	0.000	0.000	0.000
H2O	13.158	12.883	14.273	11.782	14.999	11.188	12.194	13.641	11.305	14.480	14.152	9.863	9.106	10.777	11.046	13.494	9.944	13.307	13.961	13.131
Total	100.000	100.000	100.000	100.000	100.000	100.000	100.000	100.000	100.000	100.000	100.000	100.000	100.000	100.000	100.000	100.000	100.000	100.000	100.000	100.000

Ca	0.934	0.935	0.891	0.817	0.887	0.865	0.888	0.874	0.840	0.853	0.835	0.821	0.852	0.885	0.853	0.853	0.901	0.832	0.923	0.860
Si	4.167	4.105	4.127	4.191	4.190	4.185	4.103	4.168	4.225	4.170	4.219	4.273	4.206	4.162	4.179	4.237	4.160	4.232	4.102	4.164
Rb	0.000	0.000	0.000	0.000	0.000	0.000	0.000	0.000	0.000	0.000	0.000	0.000	0.000	0.000	0.000	0.000	0.000	0.000	0.000	0.000
Ti	0.000	0.000	0.004	0.000	0.002	0.000	0.000	0.000	0.000	0.000	0.000	0.002	0.003	0.000	0.000	0.002	0.000	0.000	0.000	0.000
Na	0.000	0.019	0.018	0.066	0.024	0.031	0.063	0.052	0.047	0.055	0.063	0.037	0.039	0.068	0.056	0.036	0.031	0.076	0.027	0.047
K	0.030	0.020	0.033	0.060	0.043	0.043	0.045	0.038	0.045	0.050	0.053	0.049	0.040	0.039	0.041	0.047	0.047	0.053	0.032	0.050
Cr	0.000	0.008	0.005	0.000	0.003	0.000	0.000	0.000	0.000	0.005	0.008	0.007	0.009	0.003	0.005	0.000	0.008	0.000	0.002	0.004
Mg	0.000	0.000	0.010	0.002	0.043	0.002	0.000	0.000	0.007	0.003	0.001	0.000	0.000	0.000	0.000	0.001	0.004	0.006	0.004	0.000
Cs	0.000	0.003	0.000	0.000	0.000	0.000	0.000	0.001	0.000	0.000	0.000	0.000	0.003	0.005	0.000	0.000	0.000	0.000	0.000	0.001
Ba	0.000	0.000	0.001	0.004	0.000	0.000	0.000	0.001	0.001	0.000	0.000	0.000	0.000	0.000	0.000	0.000	0.000	0.000	0.000	0.000
Mn	0.003	0.000	0.000	0.004	0.006	0.000	0.000	0.000	0.004	0.000	0.000	0.000	0.002	0.001	0.000	0.000	0.000	0.002	0.003	0.004
Al	1.807	1.872	1.864	1.811	1.743	1.817	1.897	1.824	1.768	1.817	1.767	1.709	1.783	1.816	1.815	1.748	1.809	1.755	1.887	1.835
Ni	0.001	0.012	0.000	0.010	0.011	0.000	0.006	0.000	0.000	0.016	0.002	0.009	0.000	0.004	0.010	0.003	0.010	0.000	0.002	0.000
Fe	0.001	0.000	0.005	0.002	0.016	0.000	0.000	0.006	0.000	0.003	0.003	0.004	0.000	0.002	0.000	0.001	0.000	0.000	0.000	0.000
X	0.968	0.977	0.954	0.953	1.005	0.941	0.997	0.966	0.944	0.961	0.952	0.907	0.936	0.999	0.951	0.937	0.984	0.969	0.991	0.961
Y	1.807	1.881	1.869	1.811	1.746	1.817	1.897	1.824	1.768	1.822	1.775	1.716	1.792	1.819	1.820	1.748	1.817	1.755	1.889	1.839
Si	4.167	4.105	4.127	4.191	4.190	4.185	4.103	4.168	4.225	4.170	4.219	4.273	4.206	4.162	4.179	4.237	4.160	4.232	4.102	4.164
O	12	12	12	12	12	12	12	12	12	12	12	12	12	12	12	12	12	12	12	12

LAUMONTITE?
$CaAl_2Si_4O_{12}\cdot 4H_2O$

	Min	Max	Std-Dev	Median	Average
CaO	10.43	11.89	0.390	11.39	11.28
F	BDL	0.15	0.03	0.01	0.03
SiO2	51.72	58.57	1.061	56.40	56.37
Rb2O	BDL	BDL	BDL	BDL	BDL
TiO2	BDL	0.04	0.007	BDL	BDL
Na2O	0.001	0.48	0.107	0.14	0.15
Cl	BDL	0.02	0.00	BDL	BDL
K2O	0.183	0.58	0.11	0.34	0.38
Cr2O3	BDL	0.11	0.022	0.05	0.05
MgO	BDL	0.06	0.011	0.01	0.01
Cs2O	BDL	0.02	0.003	BDL	0.00
BaO	BDL	0.09	0.022	0.02	0.02
MnO	BDL	0.04	0.012	BDL	0.01
Al2O3	19.971	21.73	0.458	21.16	21.03
NiO	BDL	0.07	0.016	BDL	0.01
FeO	BDL	0.06	0.0	0.01	0.01
H2O	9.36	14.65	0.901	10.43	10.64
apuf					
Ca	0.809	0.94	0.03	0.89	0.88
Si	4.025	4.27	0.04	4.16	4.17
Rb	BDL	BDL	BDL	BDL	BDL
Ti	BDL	BDL	BDL	BDL	BDL
Na	BDL	0.07	0.01	0.02	0.02
K	0.017	0.05	0.01	0.03	0.04
Cr	BDL	0.01	BDL	BDL	BDL
Mg	BDL	0.01	BDL	BDL	BDL
Cs	BDL	BDL	BDL	BDL	BDL
Ba	BDL	BDL	BDL	BDL	BDL
Mn	BDL	BDL	BDL	BDL	BDL
Al	1.724	1.98	0.04	1.84	1.83
Ni	BDL	BDL	BDL	BDL	BDL
Fe	BDL	BDL	BDL	BDL	BDL
X	0.885	1.01	0.02	0.94	0.94
Y	1.726	1.98	0.04	1.84	1.83
Si	4.025	4.27	0.04	4.16	4.17
O	12	12.00	1.99E-15	12.00	12.00

laumontite?

$CaAl_2Si_4O_{12} \cdot 4H_2O$

APPENDIX X

Appendix X- Table with the compositional variation of the analysed carbonates crystals.

	Min	Max	Std-Dev	Median	Average
CaO	42.552	57.991	2.744	54.056	53.402
CO2	31.942	47.602	2.924	37.647	37.901
La2O3	BDL	0.315	0.053	0.01	0.030
SrO	BDL	0.107	0.020	BDL	0.006
BaO	BDL	0.217	0.034	BDL	0.018
Na2O	BDL	0.163	0.032	BDL	0.019
Ce2O3	BDL	0.958	0.170	0.025	0.090
FeO	BDL	1.214	0.217	0.164	0.224
TiO2	BDL	1.251	0.183	BDL	0.033
MgO	BDL	0.487	0.084	0.07	0.092
MnO	BDL	7.591	1.089	1.832	2.000
ZnO	BDL	0.092	0.020	0.009	0.016

Representative set of analyses for Calcite			
CaO	54.876	54.435	54.879
CO2	38.137	37.060	38.834
La2O3	0.000	0.049	0.015
SrO	0.000	0.000	0.000
BaO	0.000	0.052	0.000
Na2O	0.000	0.000	0.000
Ce2O3	0.088	0.081	0.000
FeO	0.235	0.680	0.031
TiO2	0.011	0.004	0.052
MgO	0.243	0.487	0.044
MnO	0.848	0.931	0.937
ZnO	0.032	0.018	0.021
apuf were calculated based on charge balance (SUM(cations)=2)			
Ca	0.978	0.965	0.984
La	0.000	0.000	0.000
Sr	0.000	0.000	0.000
Ba	0.000	0.000	0.000
Na	0.000	0.000	0.000
Ce	0.000	0.000	0.000
Fe	0.003	0.009	0.000
Ti	0.000	0.000	0.001
Mg	0.006	0.012	0.001
Mn	0.012	0.013	0.013
Zn	0.000	0.000	0.000

APPENDIX XI

Appendix XI- Table with the compositional variation of the analysed apatite crystals.

n= 9	Min	Max	Std-Dev	Median	Average
CaO	46.854	54.572	2.961	50.457	50.525
SrO	BDL	BDL	BDL	BDL	BDL
Na2O	0.001	0.180	0.055	0.048	0.060
Ce2O3	BDL	0.205	0.069	0.047	0.073
La2O3	BDL	0.045	0.019	0.007	0.017
MnO	BDL	0.119	0.040	0.071	0.068
FeO	0.136	2.286	0.917	0.314	0.971
MgO	BDL	1.244	0.521	0.095	0.360
Nd2O3	0.017	0.145	0.040	0.059	0.062
P2O5	37.007	43.175	2.419	38.242	39.843
SiO2	BDL	BDL	BDL	BDL	BDL
F	1.446	3.014	0.456	2.057	2.080
Cl	0.128	1.247	0.425	0.499	0.660
H2O	0.424	11.382	3.977	8.150	6.306

Representative analysis of Apatite crystals

	Hydrothermally Altered Basalt			Dolerite		
CaO	52.728	54.572	54.516	47.448	47.405	46.854
SrO	0.000	0.000	0.000	0.000	0.000	0.000
Na2O	0.048	0.031	0.026	0.066	0.100	0.001
Ce2O3	0.205	0.046	0.000	0.020	0.000	0.144
La2O3	0.045	0.027	0.000	0.044	0.005	0.024
MnO	0.067	0.000	0.022	0.091	0.119	0.111
FeO	0.309	0.314	0.294	2.269	2.286	1.871
MgO	0.009	0.045	0.012	1.236	1.244	0.494
Nd2O3	0.145	0.021	0.070	0.094	0.075	0.017
P2O5	40.399	42.675	42.679	38.143	38.142	37.007
SiO2	0	0	0	0	0	0
F	2.057	3.014	1.939	1.737	2.062	2.21
Cl	0.499	0.128	0.365	1.019	1.041	1.055
H2O	4.468	0.424	0.976	8.794	8.623	11.382
26 anions						
apfu				apfu		
Ca	4.953	4.899	4.898	4.689	4.685	4.790
Sr	0.000	0.000	0.000	0.000	0.000	0.000
Na	0.008	0.005	0.004	0.012	0.018	0.000
Ce	0.007	0.002	0.000	0.001	0.000	0.005
La	0.001	0.001	0.000	0.002	0.000	0.001
Mn	0.005	0.000	0.002	0.007	0.010	0.009
Fe	0.023	0.022	0.021	0.175	0.177	0.150
Mg	0.001	0.006	0.002	0.170	0.171	0.071
Nd	0.005	0.001	0.002	0.003	0.003	0.001
	4.996	4.928	4.924	4.885	4.889	4.954
P	2.998	3.027	3.030	2.978	2.979	2.989
F	0.570	0.799	0.514	0.507	0.602	0.667
Cl	0.074	0.018	0.052	0.160	0.163	0.171
OH	0.356	0.183	0.434	0.334	0.236	0.163

APPENDIX XII

Appendix XII- Table with the compositional variation of the analysed magnetite crystals.

n= 55	Min	Max	Std-Dev	Median	Average
TiO2	7.052	18.178	2.364	16.656	15.817
Cr2O3	BDL	0.057	0.015	0.011	0.015
Al2O3	0.733	4.572	0.759	1.734	1.879
V2O3	0.006	1.384	0.325	0.547	0.546
FeO	58.323	79.373	3.242	69.118	69.337
MnO	0.426	4.099	0.788	3.748	3.467
NiO	BDL	0.054	0.013	BDL	0.006
ZnO	0.028	0.504	0.108	0.347	0.336
MgO	BDL	2.529	0.475	0.091	0.275
Total	82.753	94.346	2.468	92.828	91.677

Representative Analysis of Magnetite			
TiO2	17.865	17.783	15.618
Cr2O3	0.037	0.013	0.03
Al2O3	1.683	2.046	1.241
V2O3	0.847	0.789	0.162
FeO	69.118	68.601	72.589
MnO	3.846	3.932	3.561
NiO	BDL	BDL	BDL
ZnO	0.333	0.332	0.27
MgO	0.03	0.007	0.039
Total	93.759	93.503	93.51
4 O			
Ti	0.479	0.477	0.424
Cr	0.001	0.000	0.001
Al	0.071	0.086	0.053
Fe3+	1.425	1.413	1.518
V	0.024	0.023	0.005
Total(3+)	2.000	2.000	2.000
Fe2+	0.635	0.634	0.671
Mn	0.116	0.119	0.109
Mg	0.002	0.000	0.002
Ni	0.000	0.000	0.000
Zn	0.009	0.009	0.007
(Tot. 2+)	0.761	0.762	0.789
TOTAL	2.761	2.761	2.788

APPENDIX XIII

Appendix XIII- Table with whole rock major and trace-element data.

Sample name	Na2O	MgO	Al2O3	SiO2	P2O5	K2O	CaO	Fe2O3	TiO2	P	K	Cu	Zn	Li	Sc	V	Cr	Mn	Co	Ni
	wt %	wt %	wt %	wt %	wt %	wt %	wt %	wt %	wt %	ppm	ppm	ppm	ppm	ppm	ppm	ppm	ppm	ppm	ppm	ppm
	XRF	XRF	XRF	XRF	XRF	XRF	XRF	XRF	ICP-MS	XRF	XRF	XRF	XRF	ICP-MS	ICP-MS	ICP-MS	ICP-MS	ICP-MS	ICP-MS	ICP-MS
MD-429-81.40	2.34	5.05	12.36	60.86	0.08	1.02	5.21	8.37	0.59	82.91	4241.87	38.8	67.3	20.26	26.52	145	3.66	945	16.74	3.6
MD-150-40.3	1.03	9.91	15.53	44.75	0.03	0.49	6.67	nd	0.42	28.37	2017.17	45.9	55.5	16.46	36.55	224	21.02	687	27.34	16.8
MD-174-39.4	1.89	9.84	15.21	48.98	0.08	0.44	6.76	11.78	0.69	91.65	1834.55	37.6	77.5	16.35	38.43	300	55.3	1631	36.62	43.4
MD-431-91.00(1)	3.39	3.03	12.57	65.63	0.09	0.86	3.92	8.00	0.75	93.83	3569.48	13	62.8	16.24	26.22	105	6.53	1913	16.74	5.5
MD-150-88.7	1.68	11.00	13.75	48.90	0.04	1.01	8.59	nd	0.58	46.91	4200.37	74.2	71.4	8.22	38.48	258	150.84	1211	35.57	48.6
MD-178-90.6	2.80	6.16	13.41	56.62	0.05	1.13	5.36	10.79	0.63	54.55	4694.29	26	57.6	19.64	34.25	339	37	1614	27.66	23.2
MD-178-92.0(1)	1.74	8.59	12.57	47.41	0.06	1.08	11.10	10.92	0.49	63.28	4470.16	13.4	49.1	12.53	32.34	219	145.32	1095	32.65	43.5
MD-429-81.70	2.85	5.13	12.30	61.30	0.13	0.76	6.36	7.60	0.7	138.56	3162.73	26.8	70.2	23.08	24.99	132	1.64	1494	12.6	1.9
MD-431-42.1	2.25	7.78	15.04	50.24	0.04	0.26	8.38	10.86	0.38	39.27	1095.75	53.5	59.2	7.34	36.13	234	20.53	1100	31.32	17.5
MD-178-92.0(2)	2.54	6.41	14.16	52.97	0.08	1.63	6.41	11.02	0.73	81.83	6761.27	27.7	69.9	15.02	37.04	398	6.2	1662	27.56	16.1
MD 174-73.15	1.55	8.05	14.24	51.01	0.03	0.29	7.00	13.49	0.5	31.64	1191.21	74.7	56.7	9.73	40.15	307	2.94	1098	32.03	7
MD-431-91(3)	3.40	5.10	12.87	58.51	0.09	0.92	4.61	9.59	0.45	97.1	3822.67	31.1	79.9	12.55	39.89	273	14.66	1320	23.65	10.5
MD-431-69.00	2.39	5.49	14.10	53.80	0.04	0.68	8.64	9.82	0.83	44.73	2822.38	29.4	54.1	15.13	30.56	124	10.24	1940	23.95	11.7
MD-431-95.8	3.54	3.77	13.23	60.11	0.08	1.36	5.13	8.59	0.82	91.65	5640.61	22.6	76.9	14.37	28.78	140	3.86	2448	18.29	2.4
MD-431-91.00(2)	3.21	3.27	12.65	64.42	0.08	0.79	4.24	8.45	0.73	91.645	3278.94	19.2	65	17.02	26.25	101	3.58	1902	15.55	6.1
MD-429-74.70	1.76	6.19	12.84	43.24	0.03	1.05	15.40	10.12	0.37	34.91	4341.49	13.1	47.6	11.22	32.7	223	17.93	2677	27.82	13.1
MD-431-57.80	1.48	7.31	13.56	46.23	0.02	0.20	11.30	9.69	0.5	25.09	825.96	66.8	54	16.03	42.97	266	21.28	3200	34.41	17.9
MD-174-92.2	5.04	3.85	12.82	51.25	0.08	0.11	1.99	9.68	0.9	81.83	439.96	380	89.1	7.77	31.19	156	0.72	645	22.71	0.2
MD-174-84.7	2.56	8.23	13.40	51.94	0.10	0.26	5.74	12.50	0.94	105.83	1062.54	68.1	230	12.59	35.1	344	1.26	1740	49.39	8.1
MD-178-110.5	0.78	1.67	2.97	50.46	0.92	0.45	8.16	25.46	0.13	999.4	1851.15	1410	1070	21.15	4.59	165	15.64	13768	27.6	185.4
MD-P2-8-1	2.92	4.40	14.87	58.47	0.14	1.39	1.34	6.45	1.06	157.11	5777.58	34.9	320	8.06	30.67	336	3.66	954	37.22	11
MD-P2-9-1	3.66	4.27	15.32	59.91	0.16	0.69	1.23	4.67	1.03	171.29	2843.13	290	3590	13.81	27.65	298	2.14	556	29.89	5.2
MD-P2-6.4	1.21	10.75	16.31	47.37	0.15	1.35	2.30	12.88	1.17	161.47	5619.86	180	440	21.7	34.64	340	1.54	2675	30.76	5.7
MD-P2-7-2	1.54	8.53	14.65	49.09	0.15	2.34	2.57	12.23	1.11	163.66	9728.92	45.2	280	13.6	30.19	333	2.82	2390	27.62	6
MD-P2-7-5	0.80	5.43	8.51	68.87	0.09	1.01	2.16	6.84	0.39	97.1	4196.22	81.7	290	13.33	11.85	186	15.11	1089	15.13	2.4
MD-431-117.00	1.68	9.29	14.08	48.56	0.09	0.18	7.59	14.46	0.82	93.83	734.65	77.6	13.5	5.52	39.28	343	3.46	1604	37.02	16
MD-P1-6.7	2.46	7.77	15.18	43.25	0.21	0.76	3.19	19.48	1.44		3150.28	36.8	510	8.78	35.37	354	1.3	1583	24.72	4.5
MD-P2-7.3	1.92	8.95	15.31	47.71	0.14	2.34	2.52	11.95	1.27	148.38	9691.56	48.7	510	14.28	36.57	371	1.78	2792	34.4	6.2
MD-431-121.7	1.69	8.12	13.82	53.18	0.05	0.25	6.86	11.88	0.76	57.83	1045.94	160	13.4	11.9	37.66	395	4.15	1490	32.19	13.7
MD-P2-6-7	2.13	7.90	15.17	49.98	0.14	2.51	2.43	11.48	1.2	154.93	10409.61	210	700	16.09	33.61	335	1.42	2622	29.16	5.6
MD-P3-2-1									0.43					6.88	16.56	178	2.32	73	68.51	5
MD-150-126.7									0.94					6.91	27.21	272	4.77	1091	37.7	4.8
MD-430-127.7	0.44	5.26	10.31	61.73	0.06	0.37	0.48	7.67	0.63	65.46	1539.86	160	32.6	14.99	17.35	174	1.49	220	84.85	2.9
MD-150-141.3	0.23	14.47	17.99	44.02	0.09	0.07	0.59	nd	0.94	96.01	278.09	690	170	6.61	36.83	331	4.81	1689	37.58	10.9
MD-150-105.8	3.37	4.39	13.97	60.54	0.09	2.68	0.78	8.68	0.83	93.83	11135.96	35.9	88.5	10.69	29.46	148	1.7	1588	16.93	1.7
MD-P2-4-1	nd	0.10	1.17	2.66	0.03	0.03	16.35	24.73	0.03	34.91	103.76	8890	130	18.77	0.78	76	10.86	152	70.85	8.7
MD-430-126.00	1.52	8.97	14.72	46.50	0.03	0.28	7.58	13.44	0.54	33.82	1149.71	126	66.4	5.96	45.02	347	5.54	843	39.44	8.8
MD-430-129.0	1.52	8.97	14.72	46.50	0.03	0.28	7.58	13.44	0.1	33.82	1149.71	4570	31.7	6.91	2.04	32	9.1	132	177.82	3.2
MD-P2-4-3									0.04					18.26	1.32	111	12.58	192	50.84	7.7
MD-430-131.00	0.89	6.30	17.37	47.45	0.09	0.59	0.88	8.66	0.87	93.83	2440.53	410	10.9	3.47	25.27	241	2.39	276	111.57	4.2
MD-P3-1-1	0.54	9.53	17.53	51.59	0.13	0.20	0.84	9.20	1.02	138.56	817.66	540	310	10.22	29.97	300	2.78	785	25.91	5
MD-174-96.0	2.63	5.00	13.75	56.46	0.08	0.24	5.27	11.88	0.82	86.19	1008.58	91.4	62.2	7.3	29.77	154	0.92	1100	20.35	BDL

Sample name	Ga	Ge	As	Se	Rb	Sr	Y	Zr	Nb	Mo	Ag	Cd	In	Sn	Sb	Te	Cs	Ba	La	Ce
	ppm	ppm	ppm	ppm	ppm	ppm	ppm	ppm	ppm	ppm	ppm	ppm	ppm	ppm	ppm	ppm	ppm	ppm	ppm	ppm
	ICP-MS	ICP-MS	ICP-MS	ICP-MS	ICP-MS	ICP-MS	ICP-MS	ICP-MS	ICP-MS	ICP-MS	ICP-MS	ICP-MS	ICP-MS	ICP-MS	ICP-MS	ICP-MS	ICP-MS	ICP-MS	ICP-MS	ICP-MS
MD-429-81.40	11.9	1.16	0.82	0.162	12.02	77.98	19.01	35.84	0.575	0.262	0.019	0.036	0.069	0.389	0.077	0.022	0.131	41.2	1.32	3.4
MD-150-40.3	13.2	1.8	1.09	0.116	7.14	108.63	12.72	16.68	0.215	0.173	0.04	0.054	0.058	0.276	0.04	0.01	0.096	38.5	0.65	1.9
MD-174-39.4	15.9	1.99	2.74	0.139	4.49	186.84	26.17	30.26	0.378	0.184	0.019	0.051	0.089	1.38	0.05	0.153	0.038	23.7	1.56	5.3
MD-431-91.00(1)	12.4	1.59	5.6	0.064	8.66	91.83	24.27	51.48	0.852	0.516	0.025	0.05	0.096	0.45	0.062	0.034	0.161	66.3	1.82	5.2
MD-150-88.7	14.1	1.25	2.12	0.129	10.08	86.59	15.78	26.06	0.347	0.13	0.015	0.126	0.06	0.403	0.02	BDL	0.12	18.7	0.9	2.7
MD-178-90.6	11.7	1.34	5.95	0.092	11.02	91.86	16.28	29.3	0.511	0.291	0.017	0.042	0.072	0.264	0.101	0.016	0.168	73.4	1.04	2.9
MD-178-92.0(1)	12.4	1.42	4.52	0.106	8.61	76.36	17.34	21.45	0.298	0.17	0.012	0.104	0.054	0.249	0.065	0.079	0.113	25.4	1.05	2.8
MD-429-81.70	11.9	1.34	1.39	0.215	7.42	78.21	33.06	45.06	0.781	0.402	0.026	0.064	0.079	0.517	0.057	0.054	0.061	44.4	2.24	5.7
MD-431-42.1	11.7	1.19	0.37	0.073	2.81	161.62	12.92	14.77	0.179	0.111	0.01	0.062	0.055	0.273	0.037	0.01	0.049	12.4	0.61	1.7
MD-178-92.0(2)	14.5	1.45	4.85	0.037	18.33	78.2	14.91	34.15	0.611	0.397	0.021	0.206	0.08	0.339	0.056	BDL	0.21	47	1.06	3.1
MD 174-73.15	14.3	1.35	BDL	0.116	2.84	113.9	13.59	20.63	0.318	0.306	0.018	0.282	0.07	0.157	0.046	0.011	0.015	40.8	0.57	1.7
MD-431-91(3)	12.7	1.4	3.38	0.081	9.31	96.52	14.83	16.84	0.213	0.179	0.01	0.044	0.059	0.168	0.091	0.02	0.132	27.1	0.71	1.9
MD-431-69.00	14.1	1.59	10.24	0.176	10.97	89.27	28.04	54.45	0.936	0.53	0.029	0.045	0.096	0.487	0.071	0.381	0.257	49.2	2.13	5.8
MD-431-95.8	12.2	1.47	5.75	0.132	15.78	100.06	25.22	52.48	0.882	0.587	0.03	0.047	0.085	0.634	0.053	0.115	0.241	65.5	1.82	5.1
MD-431-91.00(2)	12.3	1.47	6.89	0.134	7.86	84.97	23.92	49.52	0.842	0.455	0.026	0.074	0.086	0.379	0.051	BDL	0.138	57.5	1.88	5.2
MD-429-74.70	11.1	1.59	4.81	0.121	15.01	87.33	23.19	14.49	0.181	0.185	0.011	0.16	0.043	0.126	0.064	BDL	0.285	25.1	0.69	1.8
MD-431-57.80	15.7	1.65	0.81	0.142	3.12	105.47	20.36	18.74	0.244	0.124	0.015	0.075	0.069	0.251	0.054		0.051	11.4	1.01	2.8
MD-174-92.2	13.8	1.5	0.72	0.147	0.43	73.33	32.35	55.55	0.959	0.428	0.034	0.114	0.138	0.842	0.033	0.014	0.019	24.5	1.82	5.7
MD-174-84.7	15.5	1.38	5.31	0.142	3.56	93.57	26.97	44.49	0.672	0.21	0.024	0.086	0.087	0.552	0.236	0.025	0.046	21.8	2.21	6.4
MD-178-110.5	3.9	2.81	383.01	0.198	4.37	115.9	60.03	33.85	2.735	0.443	0.019	2.736	0.614	2.27	1.156	0.327	0.26	78.8	50.07	16.5
MD-P2-8-1	12.5	1.26	77.23	0.264	4.26	56.12	28.54	59.66	1.501	2.031	0.165	1.413	0.07	0.897	0.845	BDL	0.023	87.2	2.35	7.3
MD-P2-9-1	9.2	1.29	37.41	0.191	2.43	74.42	27.51	60.73	1.485	12.738	0.176	20.049	0.141	0.639	0.367	0.041	0.04	62.6	2.82	8.4
MD-P2-6.4	15.9	1.57	4.93	0.115	4.06	27.18	33.98	64.24	1.632	0.097	0.076	0.276	0.101	0.853	0.057	0.064	0.013	57.8	2.85	8.4
MD-P2-7-2	16	1.65	10.26	0.007	7	34.57	27	62.24	1.575	0.128	0.057	0.397	0.089	0.833	0.064	BDL	0.016	120.4	3.15	7.7
MD-P2-7-5	6.3	1.44	31.67	0.001	2.09	17.57	13.92	22.22	0.575	0.294	0.057	0.818	0.062	0.339	0.105	0.059	0.018	49.6	1.71	3.7
MD-431-117.00	15.4	1.65	16.17	0.119	1.11	103.74	29.99	38.94	0.606	0.36	0.022	0.066	0.105	0.529	0.173	0.02	0.016	29.2	2.25	5.6
MD-P1-6.7	24.1	2.02	13.25	0.116	13.55	93.58	36.41	84.08	2.413	0.384	0.043	0.077	0.437	3.282	0.3	0.938	0.26	30.9	4.06	11.5
MD-P2-7.3	17.7	1.61	20.82	0.213	7.44	38.3	33.81	70.22	1.766	0.13	0.077	2.315	0.096	1.041	0.073	0.014	0.011	129.2	2.93	8.9
MD-431-121.7	15.4	1.59	BDL	0.159	1.87	90.61	17.94	36.83	0.65	0.371	0.026	0.121	0.073	0.325	0.034	0.205	0.007	43.6	1.06	3.2
MD-P2-6-7	15	1.5	11.67	0.169	7.28	43.7	25.63	69.39	1.687	0.273	0.075	1.204	0.106	0.829	0.058	BDL	0.012	138.4	2.73	8.3
MD-P3-2-1	7	1.87	45.37	4.653	1.48	43.66	6.96	16.77	0.372	3.867	0.278	0.23	0.322	0.373	0.266	3.401	0.023	36.7	0.47	1.3
MD-150-126.7	14.6	2.09	1.71	0.296	0.21	28.7	14.02	37.03	1.326	0.311	0.037	0.142	0.043	0.696	0.044	0.21	0.007	6	1.67	5
MD-430-127.7	7.3	1.28	4.46	1.435	1.64	40.21	10.12	22.67	0.897	1.029	0.018	0.074	0.025	0.226	0.067	1.474	0.046	29	0.58	1.9
MD-150-141.3	17.5	2.94	0.09	0.313	0.22	21.05	12.03	32.23	1.178	1.171	0.023	0.092	0.074	0.529	0.016	0.109	0.009	6.9	1.63	5
MD-150-105.8	21.9	1.35	9.39	0.113	12.51	344.51	22.44	55.46	0.929	0.606	0.029	0.196	0.1	0.546	0.203	0.017	0.109	216.6	1.7	4.9
MD-P2-4-1	2.7	1.98	181.79	6.563	0.12	75.41	2.82	2.35	0.077	6.138	0.566	0.704	2.213	0.905	1.315	1.575	0.013	28.6	0.44	0.7
MD-430-126.00	15.5	1.87	BDL	0.069	2.61	92.13	12.73	19.98	0.326	0.215	0.018	0.098	0.073	0.338	0.03	0.02	0.011	38.6	0.58	1.6
MD-430-129.0	1.4	2.1	31.76	6.698	0.38	15.88	4.15	6.75	0.304	39.91	0.239	0.104	0.149	0.277	0.257	1.231	0.014	8	0.72	1.3
MD-P2-4-3	2.8	1.88	192	6.248	0.15	24.28	3.43	3.23	0.111	3.685	0.445	1.796	3.14	0.834	1.5	0.822	0.009	13.9	0.62	1
MD-430-131.00	9.3	1.63	10.38	2.357	1.62	74.3	8.15	25.52	1.189	0.87	0.057	0.061	0.081	0.435	0.061	1.103	0.027	28	0.89	3
MD-P3-1-1	13.4	1.33	7.01	0.235	0.6	39.57	15.49	57.44	1.434	5.362	0.083	0.491	0.048	0.659	0.087	3.3	0.023	14.4	1.4	4.7
MD-174-96.0	15.3	1.46	BDL	0.135	1.85	100.18	28.06	55.71	0.917	0.437	0.035	0.111	0.09	0.598	0.025	0.017	0.01	53.1	1.82	5.5

Sample name	Pr	Nd	Sm	Eu	Gd	Tb	Dy	Ho	Er	Yb	Lu	Hf	Ta	W	Tl	Pb	Bi	Th	U
	ppm	ppm	ppm	ppm	ppm	ppm	ppm	ppm	ppm	ppm	ppm	ppm	ppm	ppm	ppm	ppm	ppm	ppm	ppm
	ICP-MS	ICP-MS	ICP-MS	ICP-MS	ICP-MS	ICP-MS	ICP-MS	ICP-MS	ICP-MS	ICP-MS	ICP-MS	ICP-MS	ICP-MS	ICP-MS	ICP-MS	ICP-MS	ICP-MS	ICP-MS	ICP-MS
MD-429-81.40	0.68	3.97	1.52	0.59	2.5	0.432	2.98	0.65	1.94	1.88	0.28	1.21	0.042	0.066	0.029	0.75	0.013	0.114	0.12
MD-150-40.3	0.37	2.25	0.98	0.4	1.67	0.3	2.11	0.46	1.38	1.39	0.21	0.62	0.016	0.078	0.019	0.57	0.014	0.06	0.061
MD-174-39.4	0.88	5.28	2.02	0.76	3.4	0.584	3.96	0.9	2.53	2.35	0.35	1.03	0.028	0.083	0.019	0.68	0.018	0.084	0.051
MD-431-91.00(1)	0.89	5.14	1.99	0.73	3.14	0.565	3.87	0.85	2.45	2.44	0.38	1.71	0.061	0.186	0.038	2.87	0.02	0.152	0.207
MD-150-88.7	0.51	2.99	1.2	0.49	1.98	0.355	2.48	0.56	1.7	1.64	0.25	0.9	0.025	0.037	0.025	0.52	0.015	0.07	0.073
MD-178-90.6	0.53	2.99	1.18	0.45	1.96	0.36	2.51	0.58	1.75	1.72	0.27	0.98	0.034	0.062	0.042	1.48	0.014	0.091	0.101
MD-178-92.0(1)	0.49	2.82	1.07	0.43	1.83	0.345	2.44	0.57	1.74	1.84	0.29	0.73	0.022	0.059	0.032	0.84	0.016	0.055	0.069
MD-429-81.70	1.13	6.58	2.53	0.87	4.16	0.724	5.02	1.13	3.3	3	0.44	1.48	0.055	0.142	0.027	0.77	0.016	0.138	0.18
MD-431-42.1	0.34	2.1	0.91	0.39	1.66	0.285	2.01	0.44	1.31	1.26	0.19	0.57	0.012	0.04	BDL	0.56	0.012	0.049	0.03
MD-178-92.0(2)	0.55	3.13	1.28	0.49	1.96	0.354	2.39	0.52	1.53	1.58	0.23	1.12	0.045	0.092	0.083	1.05	0.017	0.108	0.102
MD 174-73.15	0.31	1.85	0.87	0.37	1.57	0.292	2.11	0.48	1.45	1.46	0.22	0.75	0.024	0.072	0.018	0.66	0.014	0.075	0.069
MD-431-91(3)	0.36	2.22	0.93	0.39	1.67	0.302	2.11	0.5	1.54	1.61	0.24	0.62	0.014	0.09	0.024	0.57	0.015	0.06	0.047
MD-431-69.00	1	5.68	2.22	0.77	3.57	0.641	4.35	0.96	2.78	2.64	0.37	1.78	0.063	0.215	0.044	3.25	0.016	0.167	0.237
MD-431-95.8	0.9	5.11	2.02	0.74	3.21	0.577	3.93	0.9	2.7	2.7	0.41	1.72	0.063	0.139	0.059	1.44	0.017	0.156	0.242
MD-431-91.00(2)	0.89	5.08	1.94	0.73	3.1	0.538	3.72	0.85	2.46	2.41	0.35	1.62	0.058	0.202	0.036	3.03	0.015	0.147	0.208
MD-429-74.70	0.35	2.3	1.02	0.38	2.03	0.397	2.96	0.73	2.28	2.27	0.35	0.55	0.013	0.116	0.031	0.53	0.016	0.047	0.052
MD-431-57.80	0.51	3.19	1.34	0.55	2.39	0.436	3.01	0.68	1.97	1.9	0.28	0.71	0.019	0.088	0.014	0.58	0.019	0.065	0.041
MD-174-92.2	1.01	5.95	2.4	0.81	3.94	0.717	5.12	1.14	3.49	3.47	0.54	1.89	0.067	0.078	BDL	1.17	0.016	0.171	0.185
MD-174-84.7	1.13	6.36	2.39	0.9	3.7	0.639	4.31	0.95	2.76	2.58	0.39	1.48	0.048	0.033	0.032	0.64	0.016	0.116	0.104
MD-178-110.5	8.22	34.13	6.62	1.89	8.38	1.198	7.8	1.7	4.81	3.96	0.54	0.66	0.159	0.545	0.12	75.56	0.017	2.189	0.728
MD-P2-8-1	1.32	7.28	2.7	0.96	3.97	0.714	4.83	1.04	2.97	2.83	0.39	1.75	0.102	0.231	0.557	47.26	0.015	0.17	2.182
MD-P2-9-1	1.5	8.31	2.87	0.88	4.15	0.688	4.58	0.99	2.74	2.47	0.37	1.84	0.104	0.139	0.123	22.91	0.019	0.168	3.938
MD-P2-6.4	1.46	8.2	2.96	1.16	4.45	0.798	5.2	1.15	3.4	3.15	0.46	1.93	0.115	0.375	0.011	2.1	0.015	0.177	0.23
MD-P2-7-2	1.27	7	2.46	0.9	3.65	0.633	4.3	0.97	2.97	2.94	0.46	1.9	0.109	0.321	0.022	5.63	0.018	0.18	0.385
MD-P2-7-5	0.64	3.45	1.2	0.44	1.86	0.334	2.22	0.49	1.45	1.48	0.21	0.66	0.041	0.292	BDL	9.5	0.019	0.085	0.157
MD-431-117.00	1.09	6.45	2.47	0.93	4.06	0.723	5.21	1.16	3.45	3.42	0.51	1.31	0.043	0.165	0.017	1.14	0.018	0.109	0.199
MD-P1-6.7	1.93	10.68	3.62	1.33	5.25	0.893	5.94	1.32	3.77	3.55	0.52	2.5	0.17	0.239	0.017	3.41	0.013	0.24	0.198
MD-P2-7.3	1.61	9	3.33	1.13	4.73	0.835	5.55	1.22	3.56	3.44	0.51	2.11	0.118	0.236	0.017	9.03	0.017	0.197	0.32
MD-431-121.7	0.56	3.24	1.33	0.55	2.09	0.394	2.74	0.63	1.93	1.9	0.28	1.21	0.045	0.075	0.014	0.79	0.018	0.116	0.091
MD-P2-6-7	1.41	7.81	2.68	0.97	3.82	0.657	4.29	0.91	2.55	2.27	0.31	2.07	0.12	0.257	0.168	1.65	0.015	0.193	0.365
MD-P3-2-1	0.24	1.4	0.58	0.14	0.86	0.16	1.13	0.25	0.74	0.78	0.11	0.59	0.025	0.082	0.058	5.62	0.015	0.038	0.374
MD-150-126.7	0.88	4.9	1.48	0.37	2.23	0.363	2.53	0.54	1.7	1.53	0.25	1.17	0.094	0.242	BDL	1.11	0.012	0.11	1.09
MD-430-127.7	0.35	2.15	0.88	0.16	1.15	0.218	1.55	0.38	1.19	1.46	0.21	0.7	0.062	0.11	0.019	1.5	0.012	0.066	0.22
MD-150-141.3	0.84	4.47	1.42	0.29	1.98	0.314	2.06	0.44	1.26	1.18	0.17	1.14	0.084	0.106	BDL	0.38	0.015	0.089	0.142
MD-150-105.8	0.87	4.99	1.93	0.61	3	0.533	3.61	0.79	2.37	2.26	0.32	1.79	0.064	0.111	0.065	1.98	0.009	0.17	0.177
MD-P2-4-1	0.15	0.8	0.27	0.15	0.39	0.061	0.44	0.1	0.29	0.3	0.04	0.07	BDL	0.056	0.741	50.03	0.015	0.048	0.492
MD-430-126.00	0.29	1.8	0.86	0.39	1.51	0.287	2.07	0.48	1.44	1.5	0.23	0.75	0.022	0.115	0.019	1.32	0.02	0.076	0.069
MD-430-129.0	0.26	1.29	0.37	0.09	0.51	0.088	0.65	0.15	0.46	0.51	0.08	0.19	0.021	0.131	0.399	4.77	0.019	0.112	0.204
MD-P2-4-3	0.21	1.07	0.31	0.18	0.43	0.08	0.54	0.12	0.37	0.37	0.06	0.09	BDL	0.056	0.354	29.8	0.014	0.072	0.563
MD-430-131.00	0.56	3.09	1.03	0.26	1.26	0.214	1.36	0.3	0.86	0.85	0.12	0.99	0.081	0.066	0.026	1.83	0.013	0.064	0.195
MD-P3-1-1	0.85	4.77	1.62	0.33	2.24	0.39	2.66	0.59	1.72	1.82	0.31	1.76	0.096	0.107	0.003	2.02	0.013	0.16	0.426
MD-174-96.0	0.96	5.39	2.19	0.77	3.5	0.626	4.2	0.97	2.86	2.71	0.41	1.74	0.066	0.052	BDL	0.74	0.017	0.17	0.133

APPENDIX XIV

Appendix XIV- Tables with ICP-MS detection limit(s).

	Instrumental detection limit	Analytical procedural blank	Total procedural blank
	pg.g $^{-1}$	*ng.g $^{-1}$*	*ng.g $^{-1}$*
Li	nd	20.6	48.6
Sc	nd	1.05	1.24
Ti	0.969	630	642
V	0.278	19.6	20.2
Cr	1.56	1249	1252
Mn	2.9	76.0	82.0
Co	0.113	17.5	18.0
Ni	22.2	199	214
Cu	2.02	17.7	18.7
Zn	74.5	281	301
Ga	0.216	1.06	1.11
Rb	0.433	3.89	6.28
Sr	5.32	4.28	7.41
Y	nd	0.093	0.171
Zr	1.38	4.61	5.38
Nb	1.71	1.83	2.37
Cs	0.1	1.13	1.28
Ba	20.1	7.84	8.35
La	0.121	0.115	0.307
Ce	0.151	0.289	0.606
Pr	0.04	0.022	0.07
Nd	0.084	0.077	0.1
Sm	0.078	0.061	0.065
Eu	0.065	0.081	0.09
Gd	0.259	0.123	0.134
Tb	nd	0.018	0.047
Dy	0.079	0.041	0.045
Ho	0.025	0.008	0.018
Er	0.033	0.07	0.073
Yb	0.051	0.022	0.029
Lu	0.013	0.014	0.021
Hf	1.21	0.225	0.24
Ta	0.701	0.313	0.413
Pb	0.245	7.05	7.97
Th	0.247	0.035	0.073
U	0.036	0.064	0.076

APPENDIX XV

Appendix XV- Tables with PM and C1 values.

PM	Palme & O'Neill 2004
P	87
K	260
Sc	16.4
Ti	1265
V	86
Cr	2520
Co	102
Ni	1860
Zn	53.5
Cu	20
As	0.068
Rb	0.605
Sr	22
Y	4.13
Zr	10.3
Nb	0.595
Cd	0.035
In	0.018
Sb	0.0054
Cs	0.018
Ba	6.85
La	0.6832
Ce	1.7529
Nd	1.341
Sm	0.4347
Gd	0.5855
Tb	0.1075
Yb	0.4774
Lu	0.073883
Hf	0.3014
Ta	0.0432
Pb	0.185
Bi	0.003
Th	0.0849
U	0.0229

C1	Palme et al 2012
La	0.2414
Ce	0.61947
Pr	0.0939
Nd	0.437
Sm	0.1536
Eu	0.05883
Gd	0.2069
Tb	0.03797
Dy	0.2558
Ho	0.05644
Er	0.1655
Tm	0.02609
Yb	0.1687
Lu	0.02503